International
Progress Report

IPR-03-02

Äspö Hard Rock Laboratory

Äspö Pillar Stability Experiment

Geology and properties of the rock mass around the experiment volume

Isabelle Staub
Thomas Janson
Anders Fredriksson

Golder Associates

March 2003

Svensk Kärnbränslehantering AB
Swedish Nuclear Fuel
and Waste Management Co
Box 5864
SE-102 40 Stockholm Sweden
Tel +46 8 459 84 00
Fax +46 8 661 57 19

Äspö Hard Rock
Laboratory

Report no.
IPR-03-02

No.
F86K

Author
Isabelle Staub
Thomas Janson
Anders Fredriksson

Date
March 2003

Checked by
Christer Andersson
Jan Hermansson

Date
2003-04-01

Approved
Christer Svemar

Date
2003-05-22

Äspö Hard Rock Laboratory

Äspö Pillar Stability Experiment

Geology and properties of the rock mass around the experiment volume

Isabelle Staub
Thomas Janson
Anders Fredriksson

Golder Associates

March 2003

Keywords: Äspö Pillar Stability Experiment, hydro-structural model, in-situ stresses, mechanical properties, thermal properties, spatial correlation

Abstract

A site scale Pillar Stability Experiment is planned in the Äspö Hard Rock Laboratory. One of the experiment's aims is to demonstrate the possibilities of predicting spalling in the fractured rock mass.

The investigations for the possibility of spalling are based on results from numerical simulations. General information on geology and input parameters are required to build the numerical model. This report presents an overview of the geology and properties of the rock mass around the experiment volume. Three different locations have been investigated for the location of the experiment and information on each location is provided by cores from sub-horizontal boreholes.

A hydro-structural model has been developed in a 200-m domain that includes the 3 alternatives. The main rock type in the model is Äspö diorite. Beside two major fracture zones located at the corner of the model one minor fracture zone, z4, is identified in the model. Three hydraulic conductors running WNW are also identified, two of them going through the recognition's boreholes of alternatives 2 and 3.

As all three alternatives are located in the same "block" delimited by two major fracture zones the in situ stresses are assumed to be equivalent in all 3 locations. Nevertheless some discrepancy might be encountered in alternative 3 which is closer to the edge of the block.

The mechanical and thermal properties of the rock mass are based on preliminary laboratory results obtained on samples from nearby boreholes and on previous investigations. Density could be adjusted in the 3 locations based on density logging from the new drilled boreholes. Thermal properties could be calculated from the results of density logging on the basis of relationships previously found between density and thermal conductivity/volume heat capacity.

The spatial correlation of data, and especially density, has been investigated. The spatial correlation of density is found to be very poor and the analysis shows that the spatial variability of density is best described by the spatial variability of its mean value. The analysis enhanced that density is generally higher in alternatives 2 and 3 than in alternative 1.

Sammanfattning

SKB planerar genomföra ett fullskaleförsök angående pelarstabilitet vid Äspö laboratoriet. En av målsättningarna med experiment är att demonstrera möjligheten att prediktera risken för smällberg i en uppsprucken bergmassa.

Analysen av sannolikheten och förutsättningarna till smällberg i bergmassan skall baseras på numeriska simuleringar. Uppbyggnaden av modellen kräver information om geologin och materialparametrarna. Denna rapport presenterar en översikt över geologin och bergmassans egenskaper i experimentvolymen. Tre möjliga lokaliseringar undersöktes för placering av experimentet och utvärderingen grundades på kärnor från subhorisontella borrhål.

En hydrostrukturell modell utvecklades i ett 200 meters block som innesluter alla de 3 alternativa lägena. Den vanligaste bergarten i området är Äspödiorit. Förutom 2 regionala sprickzoner i utkanten av domänen skär en dominerande struktur, sprickzon z4, modellen. Tre vattenförande spricksvärmar identifierades och 2 av dessa skär undersökningsborrhålen vid alternativ 2 och 3.

Alla 3 alternativen tillhör samma ”bergblock” begränsat av de 2 regionala sprickzonerna, därför gjordes antagandet att de initiala spänningar är lika i alla tre undersökningsområdena. Däremot kan en viss avvikelse uppmätas vid alternativ 3 som befinner sig nära blockkanten.

Bergmassans mekaniska och termiska egenskaper tolkades från tidigare utvärderade laboratorietester utförda på prover från näraliggande borrhål. Densitetsloggning utfördes i de nya borrhålen vid de tre alternativa lägena. Ett samband som tidigare etablerades mellan densitet och termisk konduktivitet/termisk kapacitet användes för att beräkna de termiska egenskaperna.

Den rumsliga korrelationen studerades hos densitetsdata. Korrelationen är mycket låg och analysen visar att densitetens rumsliga variation kan beskrivas som en medelvärdebildande process. Analysen tyder på att densiteten är högre vid alternativ 2 och 3 än vid alternativ 1.

Contents

1 Introduction

1.1 Background

SKB is planning a full-scale rock mechanics experiment. The experiment will study pillar stability. The main objectives with the pillar stability experiment are summarized as (Andersson, 2003):

1. Demonstrate the capability to predict spalling in a fractured rock mass
2. Demonstrate the effect of backfill (confining pressure) on the rock mass response
3. Comparison of 2D and 3D mechanical and thermal predicting capabilities

The experiment will be performed in the Äspö Hard Rock Laboratory (HRL) at level –450 m. Three alternative locations are studied, alternative 1 is located north of the F-tunnel, alternative 2 is located south of the TBM-tunnel and alternative 3 is located 180° from alternative 2, see Figure 1-1. A new tunnel will be excavated with start from the F-tunnel or TBM-tunnel and from the floor of the new tunnel two vertical holes will be drilled. The pillar between the holes will be heated and the additional thermal stresses shall force the rock in the holes walls to spall. Figure 1-1 illustrates the location of the experimental volumes towards the tunnel system.

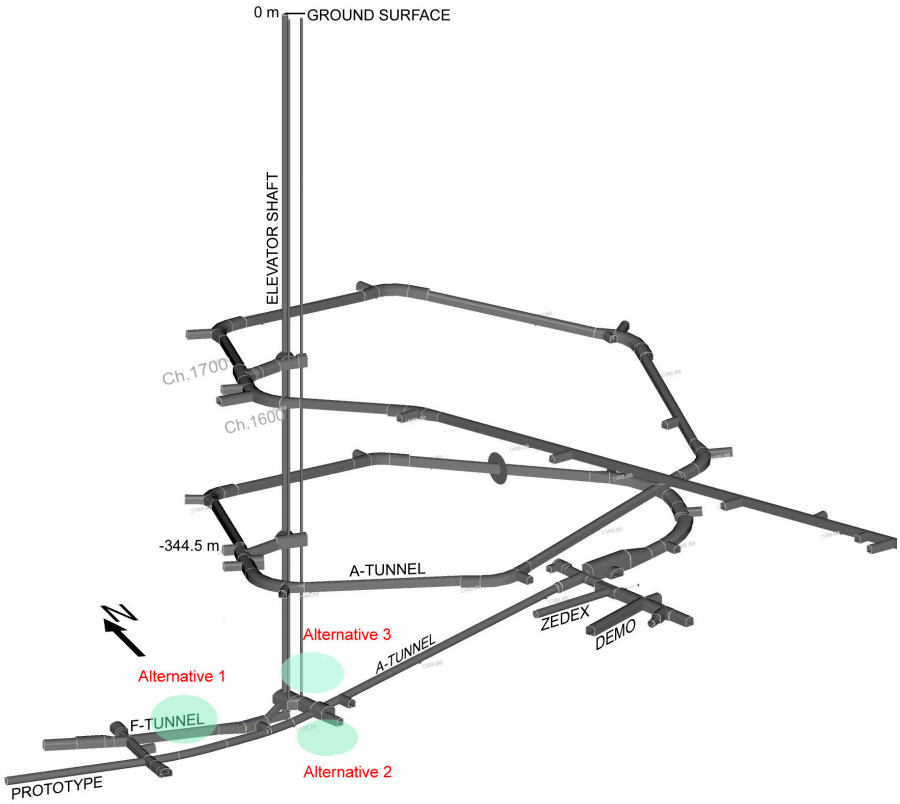

Figure 1-1. *3D view of the tunnel-system, and localization of the three alternatives for localization of the experiment.*

1.2 Objective

This report is a basic document aimed to give a general understanding of the geological structures and state of stresses around the experiment volumes. A review of the mechanical and thermal properties of the rock mass is also presented.

The analysis of geology, stresses and laboratory results for mechanical / thermal properties of intact rock and fractures have been achieved in accordance to the requirement of the experiment and the modeling.

A hydro-structural model is first developed in a 200-m domain centered onto the three alternative locations. The aim is mainly to identify structures that might at proximity of the experiment volumes.

Then the in situ stresses, mechanical and thermal properties provided from previously drilled boreholes are studied. So far the estimated properties are considered valid for all three experiment volumes.

Complementary data have been provided by drilling four boreholes at the three different alternative locations. Only geological mapping, density and flow log have been conducted on these boreholes. The complete description of density along the different boreholes helped to describe the spatial variability of this parameter.

The combined analysis of the hydro-structural model and rock mass properties at the three alternative locations will give a support for decision of the localization of the Äspö Pillar Stability Experiment.

2 Model of geological structures

2.1 Scope of work

2.1.1 Objectives

The development of this 200-m model of geological structure is aimed to identify potential minor structures and water-bearing features that could influence the present experiment and interfere with other ongoing experiments in the tunnel system around -420 m depth.

The model area is centered onto the hoist elevator shaft and is represented as a 200-m sided cube, see Figure 2-1. The model is built on the Äspö96 coordinate system and the coordinates of the model boundary are presented in Table 2-1.

Table 2-1. Coordinates of the model (Äspö96)

Model size	Origin E	Origin N	Origin z	Delta E	Delta N	Delta z
200 m	1954	7200	-350	200	200	200

Note: the Äspö96 coordinate system present a bearing of 348.2° towards the RT-90 coordinate system.

The work aims to give an overview and comprehension of the structural and geological background in a certain volume around the three alternative locations for the experiment, and give a support for the decision for localization of the experimental pillar.

2.1.2 Background data

Data required for the identification and characterization of hydrogeological structures are rock type, fracturing data (RQD, fracture frequency, and occurrence of crush zone), fracture characteristics (orientation, width, mineral filling), structural feature and flow-log / water data.

The available data were extracted from SICADA and delivered by SKB for parts of the tunnel system and the 16 boreholes located in the 200-m model, see Figure 2-1. Some of the boreholes are partly outside the model box, see Table 2-2, and the data corresponding to these sections have been extracted from the core logging.

The status of data available and used for the study is summarized in Table 2-2 for boreholes and in Table 2-3 for tunnels.

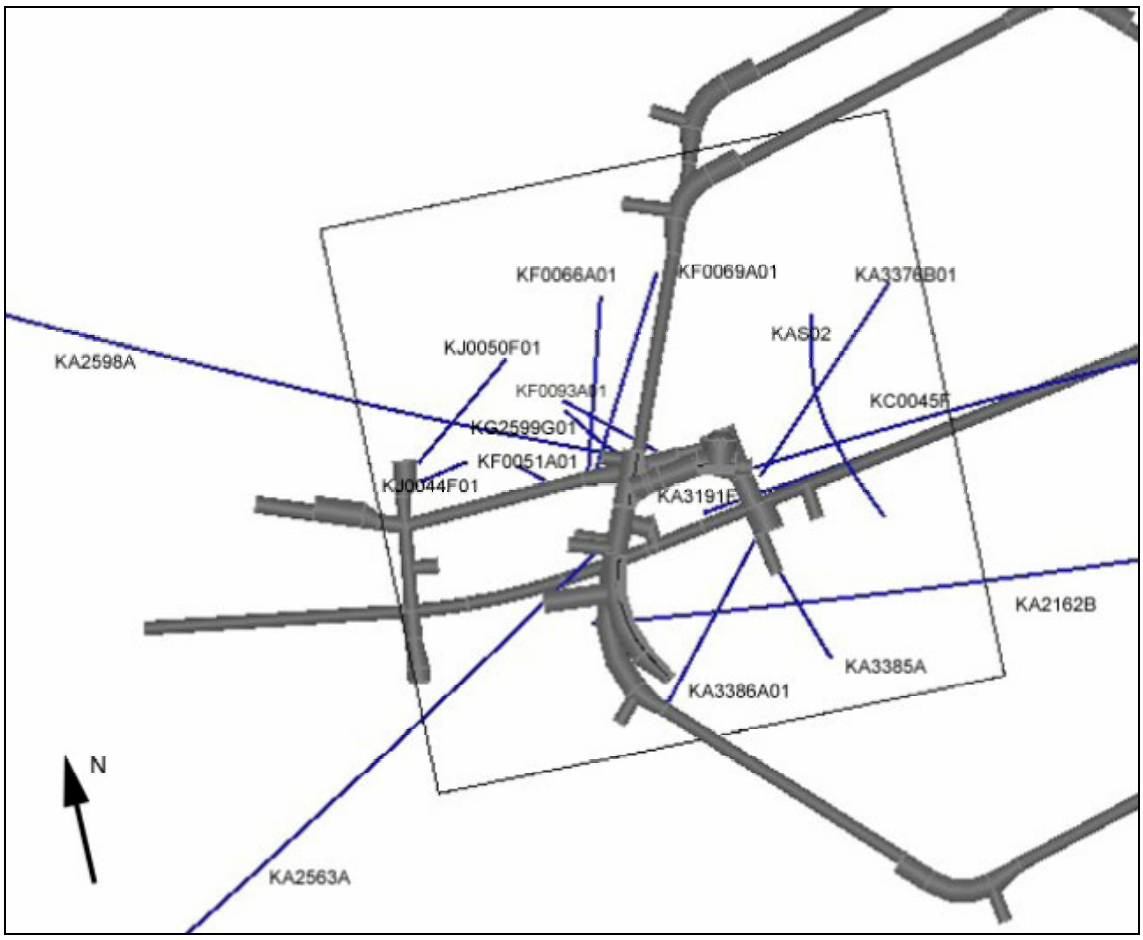

Figure 2-1. *Localization of the boreholes and tunnel system in relation to the 200-m model in the Äspö site, top view.*

Table 2-2. Data for the boreholes used in the 200-m model.

	Total length, m	From	To	Method	rqd	Fract freq	rocktype	veins, dykes,…	Fracture orient.	struct. feat	Flow data
KA2162B	288.1	232	288.1	Petrocore	X	X	X	-	-(1)	-	X
KA2563A	363.43	13	115	Petrocore	X	X	X	-	-(1)	X	X
KA2598A	300.77	16.5	87	Petrocore	X	X	X	-	X	-	X
KA2599G01	129.12	19	129.12	Boremap	X	X	X	X	X	X	-
KA3191F	924.04	352	557	Petrocore	X	X	X	-	X	X	X
KA3376B01	210.41	119	210.41	Petrocore	X	X	X	X	X	X	X
KA3385A	80.19	0	80.19	Boremap	X	-	X	-	-(1)	-	X
KA3386A01	34.18	0	34.18	Petrocore	X	X	X	X	X	X	X
KAS02	64.96	0	64.96	Boremap	X	X	X	-	-(1)	-	-
KC0045F	336.7	28	73	Petrocore	X	-	X	-	-(1)	-	-
KF0051A01	11.43	0	11.43	Boremap	-	-	X	X	-(2)	-	-
KF0066A01	36.04	0	36.04	Boremap	X	X	X	X	X	-	X
KF0069A01	17.26	0	17.26	Boremap	X	X	X	X	X	X	X
KF0093A01	46.45	0	46.45	Boremap	X	X	X	X	X	-	-
KJ0044F01	60.01	0	60.01	Boremap	X	X	X	X	-(3)	-	-
KJ0050F01	69.85	0	69.85	Boremap	X	X	X	X	X	-	-

Note 1: The fracture orientation parameter refers to the true fracture orientation (strike and dip values). Only relative fracture orientation (alpha and beta angles) is available for these marked boreholes.

Note 2: True fracture orientation has only be delivered for sealed fractures

Note 3: The strike for all fractures in KJ0044F01 is given to 0.

Table 2-3. Geometry of tunnel sections and data used in the 200-m model

Tunnel ID	Engineered structure	Trend/Plunge (Äspö96)	Chainage	Length, m	No of fractures
TASA	Access ramp	260/8.3; 265/0.4	3300-3460	160	718
TASF	F-tunnel	87/7	0-75	75	136
TASI	I-tunnel	368/2	all	27	21
TASJ	J-tunnel	187/2	all	52	22
NASA3384A	Niche	169/-1	all	24.5	26
NASA3419B	Niche	171/2	all	10	36
TASH	Hoist shaft	116/89.8	350-550	200	50

2.2 Assumptions and concepts for interpretation

The following assumptions have been made for the interpretation of geological structures.

- Mapping observations in the tunnels represent a much larger exposed fracture trace or trace of a structure than borehole logs do. These observations are therefore primary used to determine the definition and persistence of structures.
- Zones featuring shear characteristics are generally regarded as more continuous than other structures.
- Two or more discontinuity indications that can be related between different boreholes have been considered as indications of the same structure. The closest in space these indications are the most probable the potential structure is.
- Discontinuity indications with the same direction indicate that these joints may not just be more frequent but also more persistent than random indications, therefore they have been interpreted to persist until they meet another structure.
- The potential water inflow points in the borehole or in the tunnel have been identified as natural open fractures, crush zones, contacts between rock types. Water seepage in the rock has not been considered as probable as the crystalline rocks expose a very low porosity.
- The identification of potential water inflow features was conducted by looking at the core mapping 10 cm around the interpreted inflow point, which is given as the resolution of the measurement equipments. When no natural fractures or contacts could explain the inflow in this short interval, we looked at the occurrence of sealed fractures at this depth. A fracture mapped as sealed might not be totally sealed and might enable water flow.

2.3 Rock type distribution

The rock type distribution has been analyzed and the percentage of each rock type for sections of boreholes within the model domain is presented in Table 2-4.

The Äspö Diorite is the dominant rock type identified in the boreholes and in the tunnel system in the 200-m model. Fine-grained granite, or aplite, is also mapped in almost all boreholes in the model. It generally occurs as relatively thin sheets and constitutes a secondary rock type in the boreholes. Småland granite is also identified in significant sections of KAS02, KA2162B and KA2598A, as in the end of the mapped section of TASF (Ch.40 to 70).

Table 2-4. Rock type distribution in the sections of boreholes located within the 200-m model, in %

ID	Diorite	Aplite	Småland Granite	Mafic volcanite	Others	
KA2162B	0	11.2	88.8	0		
KA2563A	83.9	11.2	0	4.9		
KA2598A	44.3	47.2	7.4	1.1		
KA2599G01	83.6	10.9	0	0	5.5	Basalt
KA3191F	98.6	0	0	1.4		
KA3376B01	97	0	0	0	3	Hybrid rock*
KA3385A	86.9	6.8	0	6.3		
KA3386A01	78	17.4	0	4.6		
KAS02	50.8	16	29.4	3.5	0.2 0.1	Pegmatite Mylonite
KC0045F	6.6	93.4	0	0		
KF0051A01	100	0	0	0		
KF0066A01	90.3	7.1	0	0	2.6	Hybrid rock*
KF0069A01	88.3	4	0	0	7.6	Hybrid rock*
KF0093A01	96.2	3.8	0	0		
KJ0044F01	100	0	0	0		
KJ0050F01	97.4	2.6	0	0		

*: The term "hybrid rock" was defined to describe a mixture of Äspö diorite and greenstone when the parent rock can not be distinguished, see section 5.1.

Subordinate rock types are basic volcanic and metamorphic rocks (basalt and amphibolite), pegmatite. Thin sheets of mylonite are mapped in the elevator shaft (about -410 m and -425 m) and in KAS02 (L=440 and L=455 m).

Aplite, granite, pegmatite and basic volcanic and metamorphic rocks occur most often as veins, dykes and xenoliths less than 1 m thick.

2.4 Analysis of fracture data

2.4.1 Analysis of fracturing

The RQD and fracture frequency in the sections of boreholes located within the 200-m model have been visualized, and the graphs are presented in appendix A.

The RQD is generally high to very high (RQD=75-100) along the sections of boreholes in the 200-m model, especially in KF0066A01, KF0069A01, KF0093A01, KJ0044F01 and KJ0050F01. Low RQD values generally occur in isolated 1-m sections, and are generally correlated to the occurrence of crush zone: KA2563A at L=67-68 m, KA2598A at L=71-73 m, KAS02 at L=374-375 m, KF0066A01 at L=43-44 m.

The frequency of natural fractures is highly variable along the boreholes, see Table 2-5, but is generally in the range of 0 to 2 fractures /m. Some boreholes present a low to very low fracture frequency all along, see appendix A. This is the case of KF0069A01 and KF0093A01 that are closed to the experiment volume 1.

Table 2-5. Mean fracture frequency, and identification of crush zones in the boreholes within the model domain

ID	Natural fractures / m, average	Crush zone	
		Y / N	Depth sections
KA2162B	1.7	Y	237-238 m
KA2563A	2.92	Y	68-69 m, 96-97 m
KA2598A	2.77	Y	49-50 m, 71-72 m
KA2599G01	1.27	N	-
KA3191F	3.14	N	-
KA3376B01	1.84	N	-
KA3385A	-(1)	-(1)	-
KA3386A01	1.92	N	-
KAS02	2.86	Y	352-353 m, 356-357 m, 374-376 m
KC0045F	-(1)	-(1)	-
KF0051A01	-(1)	-(1)	-
KF0066A01	1.36	Y	43-44 m
KF0069A01	0.65	N	-
KF0093A01	0.22	N	-
KJ0044F01	1.33	N	-
KJ0050F01	0.45	N	-

(1) The fracture frequency files were not available, see Table 2-2.

2.4.2 Fracture orientation

Fracture data from boreholes and tunnels in the 200-m model were plotted on an equal area lower hemisphere projection. Data for boreholes and tunnels are analyzed separately and a Terzaghi correction is applied for the estimation of fracture density distribution to take into account the orientation of the borehole/tunnel onto the representativity of fractures almost parallel to the trace line. About 1300 fractures (natural and sealed) are mapped in the boreholes in the model box, and about 450 fractures in the tunnel system.

The pole and density plots obtained for all fractures mapped in the boreholes are illustrated in Figure 2-2 and Figure 2-3.

Fracture data for boreholes KA2162B, KA2563A, KA3385A and KC0045F could not be plotted because only alpha and beta angles were available. Moreover, data from KJ0044F01 have been removed as the strike is given to be 0 for all natural fractures, which seems unrealistic, see Table 2-2.

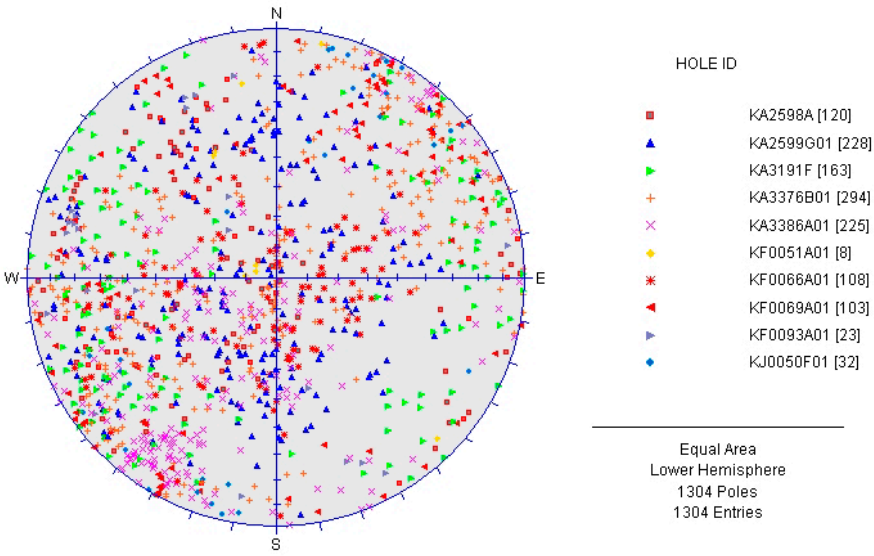

Figure 2-2. *Point plot of poles to all fractures mapped in boreholes in the 200-m model.*

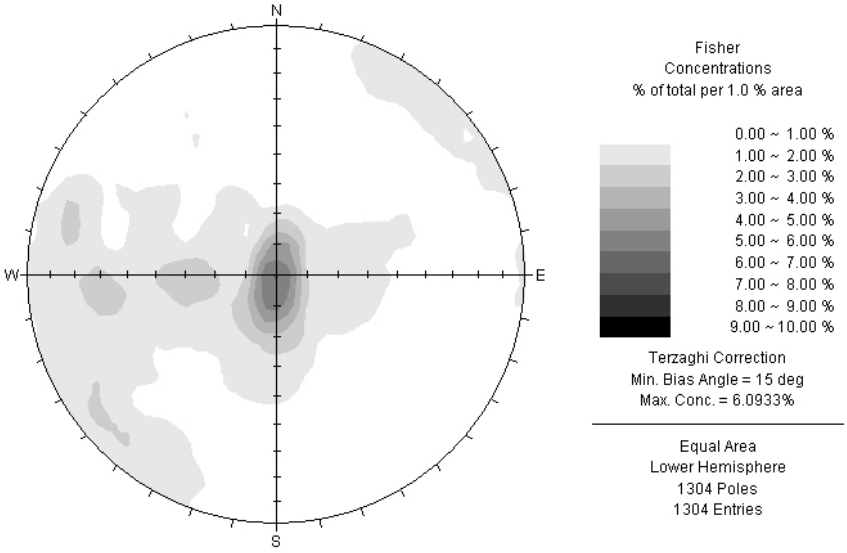

Figure 2-3. *Density plot of poles to all fractures mapped in boreholes in the 200-m model.*

Two dominant fracture sets are identified, one sub-horizontal that is the most dominant, and 1 striking WNW and dipping 80-90°. Tow another clusters of fractures striking N are identified, one dipping 60-70°, and one dipping 30-50°.

The poles and density poles for natural fractures only are presented in Figure 2-4 and Figure 2-5. Data from boreholes KA2598A and KA3191F have been removed as natural and sealed fractures are not distinguished in the oriented fracture data file.

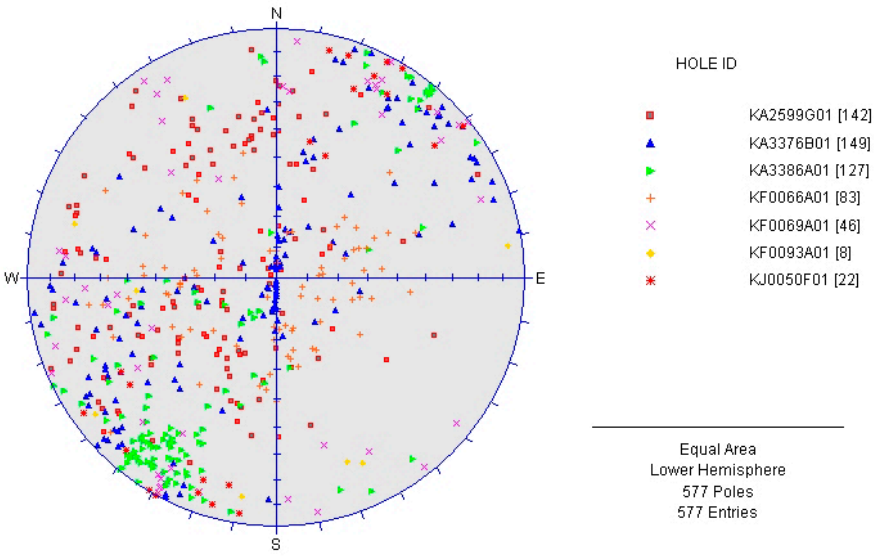

Figure 2-4. *Point plot of natural fractures mapped in boreholes in the 200-m model.*

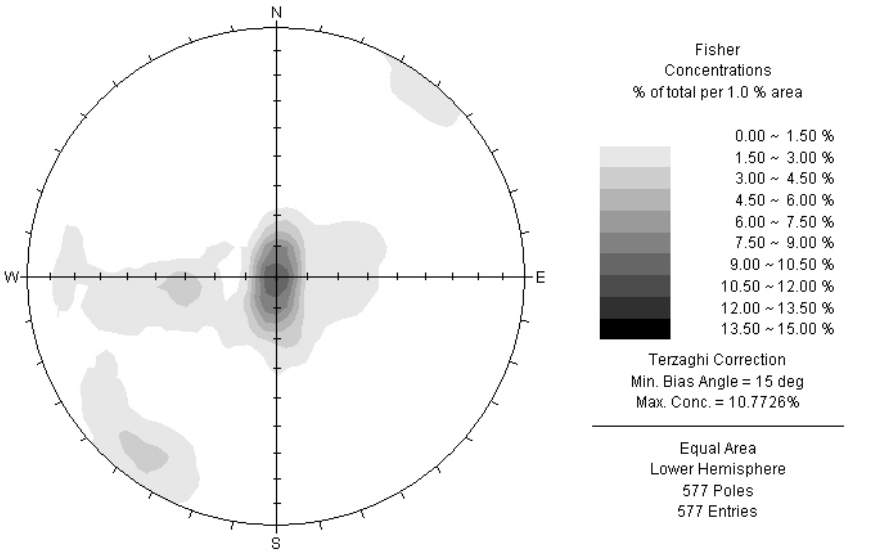

Figure 2-5. *Density plot of poles to natural fractures mapped in boreholes in the 200-m model.*

The orientation of borehole lines is plotted as a reference in Figure 2-6.

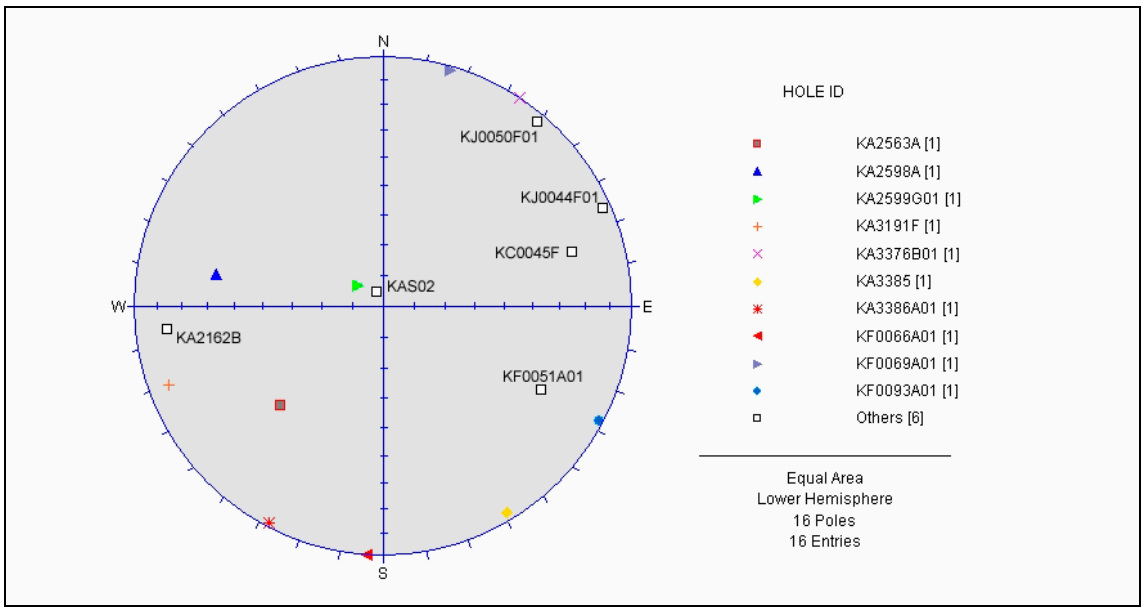

Figure 2-6. *Stereoprojection of the boreholes orientation in the 200-m model.*

The stereoplot for natural fractures in the boreholes, Figure 2-5, is quite similar to the one obtained for all boreholes in the model domain, Figure 2-3. The same fracture sets are identified but the density distribution of the sets is slightly different. WNW striking fractures are more frequent in natural fractures, and the density of sub-horizontal fractures is also enhanced.

The projection of poles to fractures for tunnel sections within the 200-m model is presented in Figure 2-7 and the estimation of fracture density distribution after Terzaghi correction is illustrated in Figure 2-8.

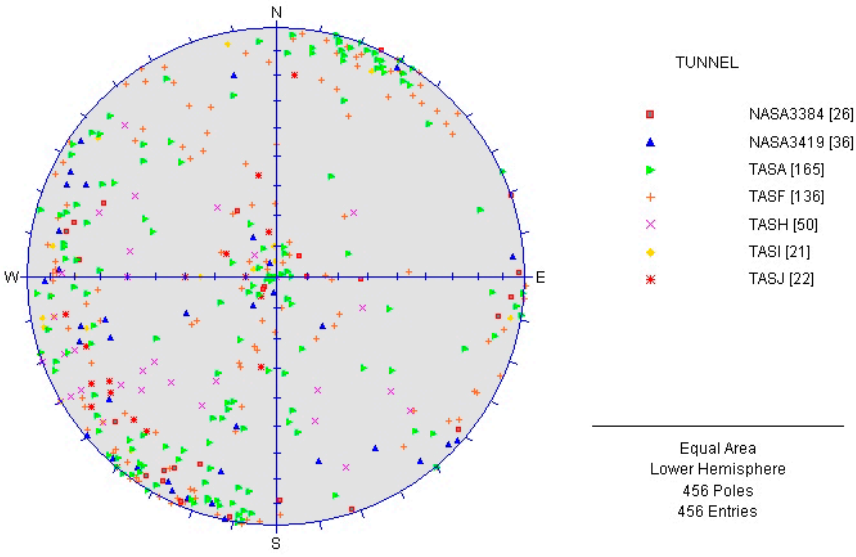

Figure 2-7. *Point plot of all fractures mapped in tunnel within the 200-m model domain.*

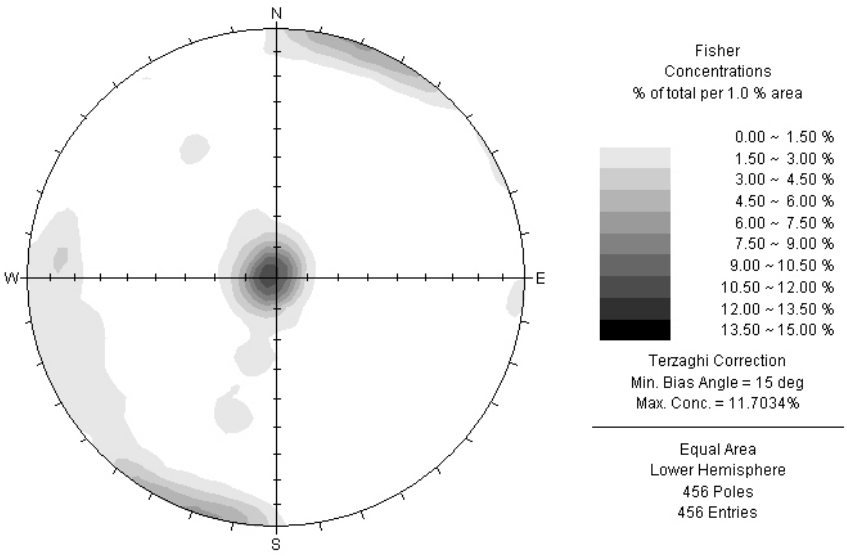

Figure 2-8. *Density plot of poles to all fractures mapped in tunnel within the 200-m model domain.*

The orientation of tunnels and niches centre lines is illustrated in Figure 2-9.

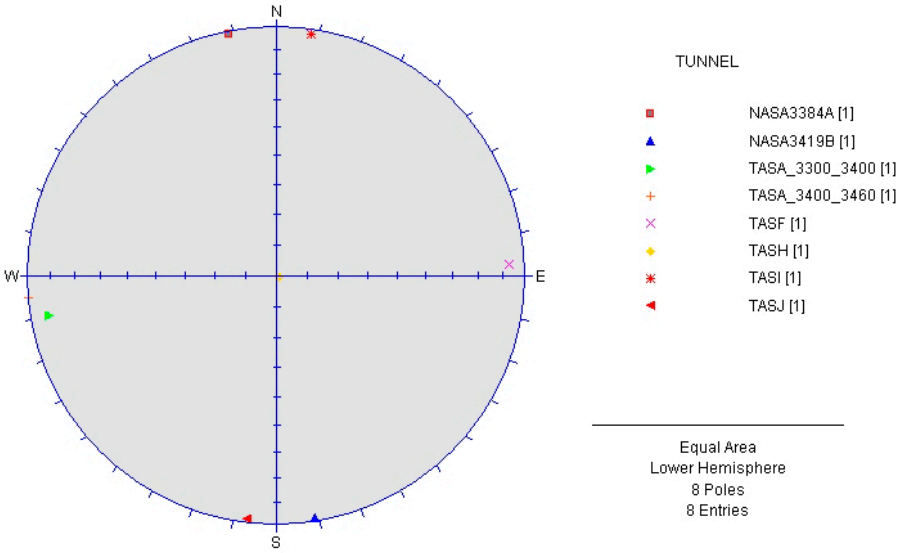

Figure 2-9. *Stereoprojection of tunnel sections orientation in the 200-m model*

Two fracture sets are clearly identified from the density plot of fractures in tunnels, see Figure 2-8. The dominant fracture set is sub-horizontal, and the second set is sub-vertical striking WNW. A third subsidiary set can be identified which is sub-vertical striking N.

The amount of fractures plotted in tunnels is almost a third of the amount plotted in boreholes, but the stereoplots are quite similar and the same fracture sets are identified in both cases, see Figure 2-3 and Figure 2-8.

2.5 Analysis of flow-logging data

The analysis presented in this section focuses primarily on the identification and when possible the characterization of water-bearing fractures and/or structures in the model area.

A short review of the used background data is done in section 2.5.1 and then the identification of potential isolated conductors is presented for each borehole with flow data in section 2.5.2. A discussion on the identified potential candidates is presented in section 2.5.3.

2.5.1 Background data

Flow / water data are provided from:

– In the tunnel system: water-bearing fractures are distinctly mapped (Rhén, 1995) and their characteristics (fracture orientation, inflow rate, mineral filling) are reported in SICADA;

– Raw flow data in the boreholes are obtained from different measurement methods: difference-log, spinner-flow and UCM-flow, see Table 2-6. Complementary information is found in Rhén (2000) and Andersson, P. *et al.* (2002).

Rhén (2000) presents the results of interpreted flow data for different boreholes in Äspö, and some are included in the 200m-model. These boreholes are KA2162B, KA2563A, KA2598A, KA3191F, KAS02 and KC0045F. For all boreholes the inflow in the boreholes is given as flow rate (l/min) and evaluated transmissivity (m^2/s), with the exception of KAS02 for which only evaluated transmissivity data are presented.

Andersson, P. *et al.* (2002) gives a detailed interpretation of water inflow points/sections in the TRUE Block Scale volume, which includes borehole KA2563A.

The difference-flow log in boreholes KF0066A01, KF0069A01, KA3376B01 and KA3386A01 are presented and analyzed in Pöllänen and Rouhiainen, 2002 and 2003, see Table 2-6.

Table 2-6. List of flow-logging data in the 200-m model

Borehole	Length of borehole in the model, m		Flow-logging methods	Source of data
	From	To		
KA2162B	232	288.1	Spinner-flow	SICADA Rhén *et al.* (2000)
KA2563A	13	115	Packer-flow, UCM-flow	SICADA Rhén *et al.* (2000)
KA2598A	16.5	87	Difference flow-logging, UCM-flow	SICADA Rhén *et al.* (2000)
KA3191F	119	210.41	UCM-flow	Rhén *et al.* (2000)
KA3376B01	0	80.19	Difference flow-logging	Pöllänen *et al.* (2003)
KA3385A	0	34.18	UCM-flow	SICADA
KA3386A01	0	64.96	Difference flow-logging	Pöllänen *et al.* (2002)
KC0045F	28	73		Rhén *et al.* (2000)
KF0066A01	0	60.01	Difference flow-logging	Pöllänen *et al.* (2002)
KF0069A01	0	69.85	Difference flow-logging	Pöllänen *et al.* (2002)

The interpreted data have been visualized in 3D with RVS, and the water-conducting points/sections are illustrated in Figure 2-10 and Figure 2-11.

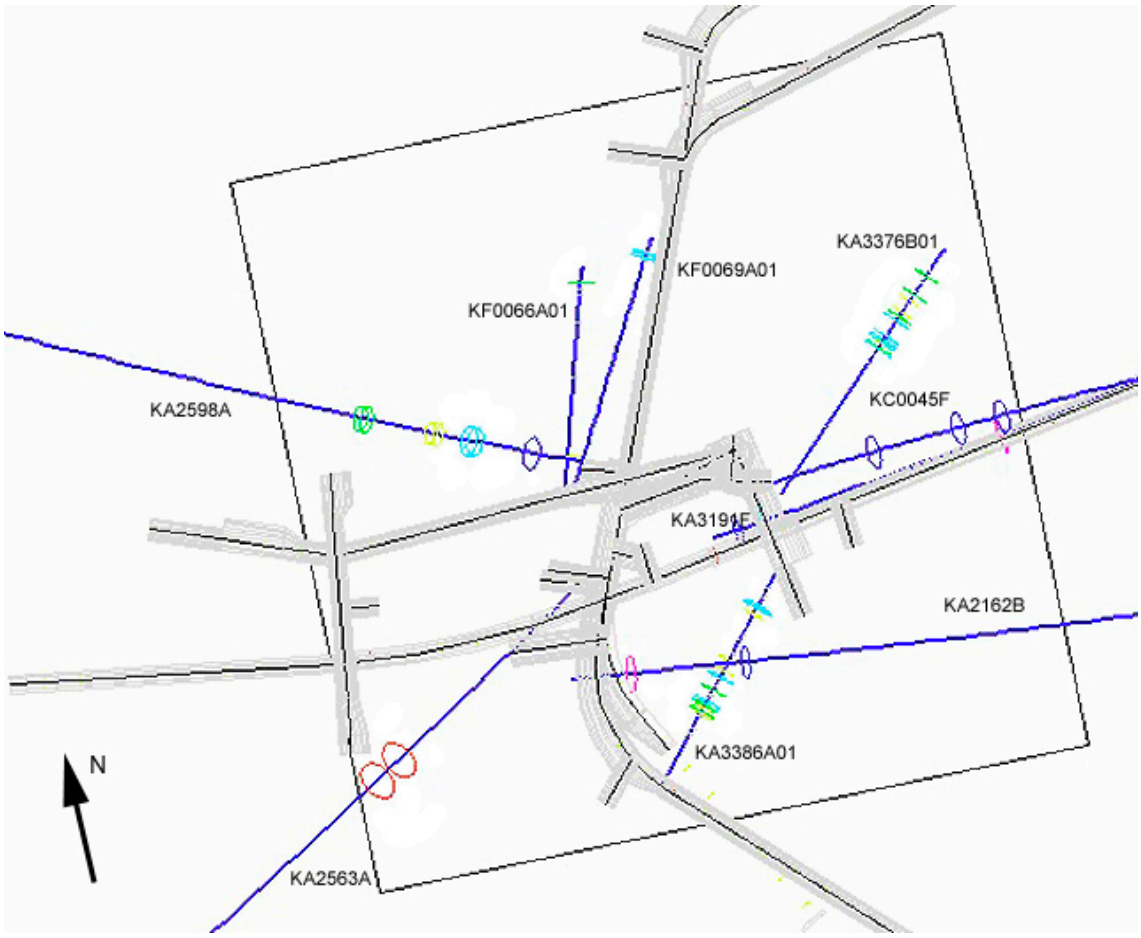

Figure 2-10. *Top view of the inflow points in the 200m-model. The diameter of the cylinders increase with the measured flow rate*

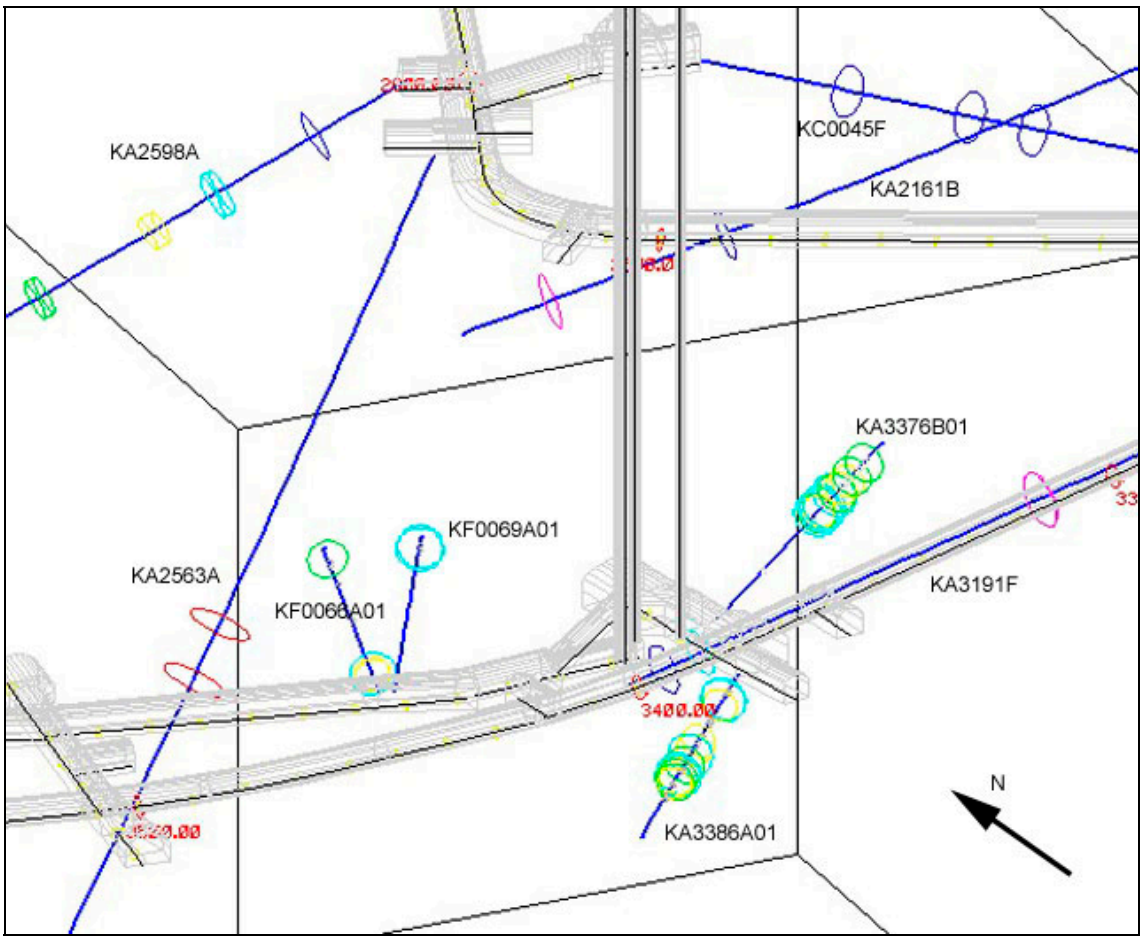

Figure 2-11. *Side view of the inflow points in the 200m-model. The diameter of the cylinders increase with the measured flow rate*

2.5.2 Identification of water-bearing features

The main cause of water inflow in the boreholes is assumed to occur at first in natural fractures and crush zones. Secondly water inflow related to contacts between two rock types can also be of significance (see Rhén, 2000).

The first stage in this work has been to identify the potential candidate(s) at each interpreted water inflow point/section. Water-bearing features have been identified along some boreholes and their characteristics presented in Andersson, P. *et al.* (2002). For other boreholes the identification of potential candidates was done by analyzing the different parameters provided by core mapping (such as RQD, occurrence of crush zone, natural fractures).

Natural fractures and crush zones mapped at the proximity of these inflows constitute likely candidates. A mapped contact between two rock types constitutes also a potential candidate.

The correlation of mapped observations in borehole cores and inflow depths has been listed in appendix B. The identification of potentially water-conducting fractures/features in each borehole is presented below, from Table 2-7 to Table 2-14. Only inflow points/sections with a measured or estimated inflow rate greater than 1 l/min are reviewed in these tables.

KA3386A01

A high number of inflow points/sections have been identified in this borehole, see Figure 2-11, and 26% of the water-bearing "sections" provide an inflow greater than 1 l/min. Most of the inflows occur between L=36 and L=44 m. The identification of potential candidates is presented in Table 2-7.

Table 2-7. Identification of water-bearing fractures based on flow and fracture data (Q>1 l/min), KA3386A01

Borehole	Inflow		Identification of feature						
	Depth	Q (l/min)	Depth, m	Strike	Dip	Width, mm	Ap, mm	Min.	Comments
KA3386A01	10.1	3.33	10.05 10.68	112.2 308.5	87.6 73.1	1 2	1 1	Ca,Fl,Py Ca,Ch	Nat. fract.
KA3386A01	10.7	3.33	10.72 10.75	328.2 317.4	68.5 59.2	1 1	0 1	Ca Ca,Ch	Nat. fract.
KA3386A01	32.4*	6.67	32.34	302.2	69.8	2	1	Ca,Ch	Nat. fract.
KA3386A01	36.4	2.17	36.46	298.1	83.3	1	0	Ch,Ca,Py	Nat. fract.
KA3386A01	40*	5.8	40.06	302	67.6	4	2	Q,Ch,Ca	Nat. fract.
KA3386A01	41	4.67	40.96	298.9	72.4	1	0	Ch,Ca	Nat. fract.
KA3386A01	41.2*	2.83	41.28	291.5	84.3	2	1	Ca	Nat. fract.
KA3386A01	43.1	2	43.09	343.6	27	2	0	Ch	Nat. fract.
KA3386A01	43.6	1	43.51	296.9	81	1	0	Ca,Ch,Py	Nat. fract.

Ca: calcite, Ch: chlorite, Ep: epidote, Q: quartz, Fl: fluorite, Py: pyrite

*. The presence of a leaky fracture is uncertain or the flow rate is uncertain (Pöllänen and Rouhiainen, 2002)

KA3376B01

The total inflow in the open borehole is measured to 95 l/min. 50% of inflow points in the borehole are above 1 l/min, and the flow rate exceeded the upper limit of measurement of the equipment at four fractures (Pöllänen and Rouhiainen, 2003). Only 46 l/min were "recovered" by the flow meter which implies that the "missing" 49 l/min might be unmeasured inflow from the four inflow points identified between L=49.8 and L=57 m.

The correlation of water inflow depths to RQD, rock type, occurrence of natural fractures and/or crush zone is presented in appendix B. All the water-conducting points are included in a 50-m long massive Diorite core, cut by local thin veins of fine-grained granite.

As the depth resolution is given to be 0.1 m, the correlation of inflow points to natural fractures or contacts was analyzed within 20 cm of the interpreted inflow depth. The potential candidates are listed in Table 2-8

Table 2-8. Identification of water-bearing fractures based on flow and fracture data (Q≥1 l/min), KA3376B01

Borehole	Inflow		Identification of feature						
	Depth	Q (l/min)	Depth, m	Strike	Dip	Width, mm	Ap, mm	Min.	Comments
KA3376B01	47.7	4.7	47.66 47.739	138 135.3	82.7 82.8	1 1	1 0	Ch,Ca Ch,Ca	Nat. fract.
KA3376B01	48.2	2.5	48.266	33.6	64.6	1	0	Ch,Ca,Py	Nat. fract.
KA3376B01	49.5	1.2*	*49.575*	*0.2*	*51.4*	*1*	-	*Ch,Ca*	*Sealed fracture*
KA3376B01	49.8	6.7**	*49.815*	*117.9*	*79.2*	*1*	-	*Ch,Ca*	*Sealed fracture*
KA3376B01	50.5	7.3**	50.424	125.7	85.8	1	1	Ca,Ch	Nat. fract.
KA3376B01	51.8	6.7**	51.782	123.2	70.4	1	1	Ca,Ch	Nat. fract.
KA3376B01	57	6.7**	56.995	130.7	78.4	1	1	Ca,Ch	Nat. fract.
KA3376B01	58.2	2.2	58.087	135.5	65.7	2	2	Ca,Ch	Nat. fract.
KA3376B01	59.8	0.9	59.692	153.5	77.8	1	1	Ch,Ca	Nat. fract.
KA3376B01	63.4	1.1	63.468 63.506	135.5 136.1	81.5 77.5	2 1	0 0	Ep,Ca,Ch Ca,Ch	Nat. fract.
KA3376B01	65.6	2.1	65.7	276.8	67.7	-	-	-	Contact rock/vein
			65.505 65.56	318.7 358.4	43.8 80.3	1 2	0 2	Ch,Ca Ca,Ch	Nat. fract.
KA3376B01	71.7	1.7	71.597	322.7	76.4	1	1	Ca	Nat. fract.

Ca: calcite, Ch: chlorite, Ep: epidote, Q: quartz, Fl: fluorite, Py: pyrite

*: flow rate uncertain / **: upper limit of measurement exceeded, the flow rate might be larger than the specified value (Pöllänen and Rouhiainen, 2003).

KA2162B

The water conductive sections in KA2162B have been interpreted from raw flow-log data by Rhén (2000). The pressure response monitored during the drilling of this borehole did not indicate significant water conductive structures at the end of the borehole, see Rhén *et al.* (1993). The analysis of core log parameters indicated that natural fractures might be potential candidates, see Table 2-9.

Table 2-9. Identification of water-bearing fractures based on flow and fracture data (Q>1 l/min), KA2162B

Borehole	Inflow		Identification of feature						
	Depth	Q (l/min)	Depth, m	Strike	Dip	Width, mm	Ap, mm	Min.	Comments
KA2162B	237-238	25	237.45 237.93 238.08	- - -	- - -	- - -	- - -	No data	Nat. fract.
KA2162B	252-254	1	253.61 253.98 254.05	- - -	- - -	- - -	- - -	No data	Nat. fract.
KA2162B	256-257	3	256.22 256.37	- - -	- - -	- - -	- - -	No data	Nat. fract.
KA2162B	270-271	28	271.43	-	-	-	-	No data	Contact
			270.06 270.1 270.45 270.48	- - -	- - -	- - -	- - -	No data	Nat. fract.

Only alpha and beta angles are available

KA2563A

Two water-conductive sections (L=90.35-94.85m and L=102-105m) inside the model domain are interpreted by Rhén (2000). The flow rates measured in these sections are very high, see Table 2-10, and are classified as High-permeability features (Rhén, 2000). In both cases the RQD is high to very high (RQD>75), and the fracture frequency vary from 0 to 6 fractures/m, see appendix B.

The interpretation of hydraulic pressure monitoring and hydraulic tests performed during the TRUE Block Scale experiment (Andersson, P. *et al.*, 2002) points out two deterministic conductive structures for these large single inflows, see Table 2-10.

Some other significant conductive features are also identified in the model area, at L=12.5 m and L=68.5 m. Strike and dip of the natural fractures, and the aperture estimation, are taken from Andersson, P. *et al.* (2002).

Table 2-10. Identification of water-bearing fractures based on flow and fracture data (Q>1 l/min), KA2563A

Borehole	Inflow		Identification of feature						
	Depth	Q (l/min)	Depth, m	Strike	Dip	Width, mm	Ap, mm	Min.	Comments
KA2563A	12.5		12.5	335	82	-	-	-	Nat. fract.
KA2563A	68.5		68.5	135	87	-	-	-	Nat. fract.
KA2563A	90.35-94.85	120	94.4	296	74	-	-	No data	Nat. fract.
KA2563A	102-105	714	103	114	89		10-20		Nat. fract.

KF0066A01

The inflow at L=8.1 m in KF0066A01 can be correlated to an open fracture mapped at L=8.09 m, see Table 2-11. Any mapped natural fracture can be associated to the inflow at L=56.1 m. The inflow point is in a body of schistose Diorite but very close to the contact with a massive xenolith of Amphibolite. The contact between the two rock types might be a potential candidate for the water inflow. Complementary information is required for the identification of the conductive structure at this depth.

Table 2-11. Identification of water-bearing fractures based on flow and fracture data (Q>1 l/min), KF0066A01

Borehole	Inflow		Identification of feature						
	Depth	Q (l/min)	Depth, m	Strike	Dip	Width, mm	Ap, mm	Min.	Comments
KF0066A01	8.1	3.5	8.09	225	20.7	1	0	Ca,Ch	Nat. fract.
KF0066A01	56.1	2.7	56.03	69	45.9	-	-	-	Contact

Ca: calcite, Ch: chlorite

KF0069A01

Two water inflow points are recorded closed to the bottom of the borehole. The RQD value is 100 in both sections and the fracture frequency is low, see appendix B. The inflow at L=64.8 m in KF0069A01 might be correlated to a mapped natural fracture at L=64.64 m, see Table 2-12.

No natural or sealed fractures have been mapped at proximity of the inflow at L=66.1m, and according to appendix B, no contacts occur. The measured inflow is nevertheless consequent. An error in the interpretation of depth of inflow might explain this situation.

Table 2-12. Identification of water-bearing fractures based on flow and fracture data (Q>1 l/min), KF0069A01

Borehole	Inflow		Identification of feature						
	Depth	Q (l/min)	Depth, m	Strike	Dip	Width, mm	Ap, mm	Min.	Comments
KF0069A01	64.8	4.3	64.64	290.3	80.9	1	1	Py	Nat. fract.
KF0069A01	66.1	4.3							?

Py: pyrite

KA2598A

The first and second water-conducting occurrences in KA2598A are mapped in a massive homogeneous body of granodiorite with exhibit high RQD and low fracture frequency (see appendix B). The third water-conducting section between L=49.8 and L=52.4 m is located in a faintly tectonized body of aplite, and a crush zone less than 1 m thick is mapped at L=49-50 m, see appendix B. This location is also indicated by 2 seismic reflectors (Olsson *et al.* 1994), located at L=50m (strike/dip: 62°/21°) and L=52 m (strike/dip: 106°/75°). Several natural fractures are possible candidates for the water inflow in these sections, see Table 2-13, and more information is required to identify the most probable candidate. True fracture orientation is not deliverable for some of these fractures.

Table 2-13. Identification of water-bearing fractures based on flow and fracture data (Q>1 l/min), KA2598A

Borehole	Inflow		Identification of feature						
	Depth	Q (l/min)	Depth, m	Strike	Dip	Width, mm	Ap, mm	Min.	Comments
KA2598A	18.5	12	18.07	-	-	1	-	Ca	Nat. fract.
KA2598A	37.4-39.4	4	37.47 38.35 39.32	357.13 359.96 156.26	89.82 85.7 88.83	1 1 1	- - -	Ch Ch Ca	Nat. fract.
KA2598A	49.8-52.4	1	49.72 49.82 49.94 50.2 50.73 51.16 51.21 51.27 51.42 51.9	- - - - - - - - - -	- - - - - - - - - -	0 0 1 1 1 1 1 1 1 1	- - - - - - - - - -	Ch,Ca Ch Ch,He Ca Ca Ch Ch,Ca Ca,Ch Ch,Ca Ch	Crush zone, Nat. fract.
KA2598A	73.5-75.5	3	73.52 73.56 73.6 73.8 74.03 74.35 74.97 75.17 75.31 75.41	345.55 318.39 - 352.62 52.48 - 152.5 57.78 52.4 224.59	34.03 41.39 - 9.22 52.37 - 10.65 59.66 56.60 2.31	1 1 1 1 1 1 1 1 1 1	- - - - - - - - - -	Ch Ca Ca Ch Ch Ch Ca,Ch Ch Ch Ca,Ch	Nat. fract.

Ca: calcite, Ch: chlorite, He: hematite

KA3191F

The two points with high flow rate in KA3191F at L=123.5 and L=124.1 m can be correlated to the occurrence of a crush zone mapped between L=122 and L=125m, see appendix B. Natural fractures are also mapped at the depth of occurrence of these inflows. Several natural fractures are potential candidates for the inflow at L=195m, see Table 2-14. True fracture orientation is not delivered for some of these fractures.

Table 2-14. Identification of water-bearing fractures based on flow and fracture data (Q>1 l/min), KA3191F

Borehole	Inflow		Identification of feature						
	Depth	Q (l/min)	Depth, m	Strike	Dip	Width, mm	Ap, mm	Min.	Comments
KA3191F	123.58	60	123.64	322.42	76.6	4	-	Ca,Ep,Ch	Crush zone
KA3191F	124.1	50	124.08	213.95	73.25	3	-	Ca	Crush zone
KA3191F	195	7	194.91 194.95 194.99 195.12	- - - -	- - - -	0 0 0 0	- - - -	Ch,Ep Ch,Ca,Ep - Ch,Ca	Nat. fract.
KA3191F	202.5	25	202.57	328.85	74.18	0	-	Ca	Nat. fract.

Ca: calcite, Ch: chlorite, Ep: epidote

KC0045F

Water inflows at L=31.6 and L=57.8 occur in minor sections of crushed rock with a very low RQD, see appendix B. The section of borehole between L=68 and L=72 shows an increased fracturing, and the inflows at L=68.1 and L=71.2 m can be associated to deterministic natural fractures, see Table 2-15.

The inflows in KC0045F within the model domain are related to minor local inflows and can not be directly correlated to any radar or seismic reflectors (Olsson *et al.*, 1994).

Table 2-15. Identification of water-bearing fractures based on flow and fracture data (Q>1 l/min), KC0045F

Borehole	Inflow		Identification of feature						
	Depth	Q (l/min)	Depth, m	Strike	Dip	Width, mm	Ap, mm	Min.	Comments
KC0045F	31.6	15	31.53 31.64	- -	- -	- -	- -	- -	Crush zone, Nat. fract.
KC0045F	57.8	21	57.7 57.85	- -	- -	- -	- -	- -	Crush zone, Nat. fract.
KC0045F	68.1	4	68.05	-	-	-	-	-	Nat. fract.
KC0045F	71.2	20	71.11	-	-	-	-	-	Nat. fract.

KA2511A

KA2511A is very closed to the upper SW corner of the model at L=21-22m, see Figure 2-11. Data from this borehole has not been included in the general study as the section included in the model is very short, but we took into consideration an inflow point at L=23 m. The water inflow is located in fine-grained granite and cannot be correlated to either seismic or radar events (Olsson *et al.* 1994). This inflow is correlated to a conductive natural fracture mapped at L=23 m, see Table 2-16, and identified by Andersson, P. *et al.* (2002).

Table 2-16. Identification of water-bearing fractures based on flow and fracture data (Q>1 l/min), KA2511A

Borehole	Inflow		Identification of feature						
	Depth	Q (l/min)	Depth, m	Strike	Dip	Width, mm	Ap, mm	Min.	Comments
KA2511A	23	30	23.1	300	80	-	-	-	Nat. fract.

2.5.3 Analysis of identified potential conductive features

The orientation of natural fractures identified as certain or probable conductive features in section 2.5.2 has been analyzed. The poles to fracture planes have been plotted on an equal area lower hemisphere stereographic projection. The plot is illustrated in Figure 2-12.

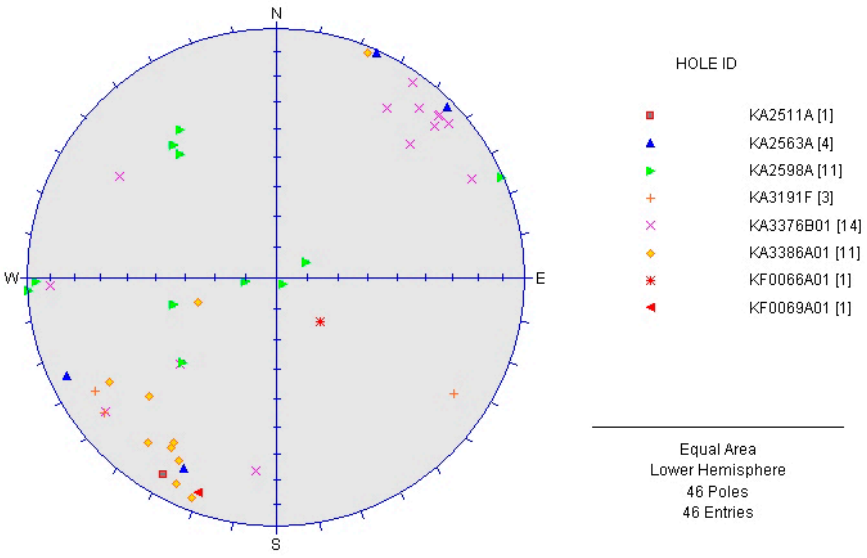

Figure 2-12. *Point plot of poles to certain and probable conductive fracture planes identified in boreholes within the 200-m model.*

Most of the potential candidates identified in the previous sections present a similar homogeneous orientation, striking WNW, dipping 80° to sub-vertical. This is remarkable for boreholes KA2563A, KA3386A01 and KA3376B01.

The possible candidates identified in KA2598A present a heterogeneous orientation and about half of them are sub-horizontal to gently dipping fractures.

2.6 Model of geological structures

2.6.1 Major structures mapped at Äspö HRL

According to the global structural model of Äspö, two major fracture zones are identified within the model domain: NE2 and EW1-b. EW1-b is striking NNE and dipping almost 80° East. NE2 is going through the SE corner of the model, striking NNE and dipping 75° SE. These major structures are forming an edge beside the SE corner of the model. The representation of the modeled fracture zones truncated at the boundary of the model boundary is illustrated in Figure 2-13.

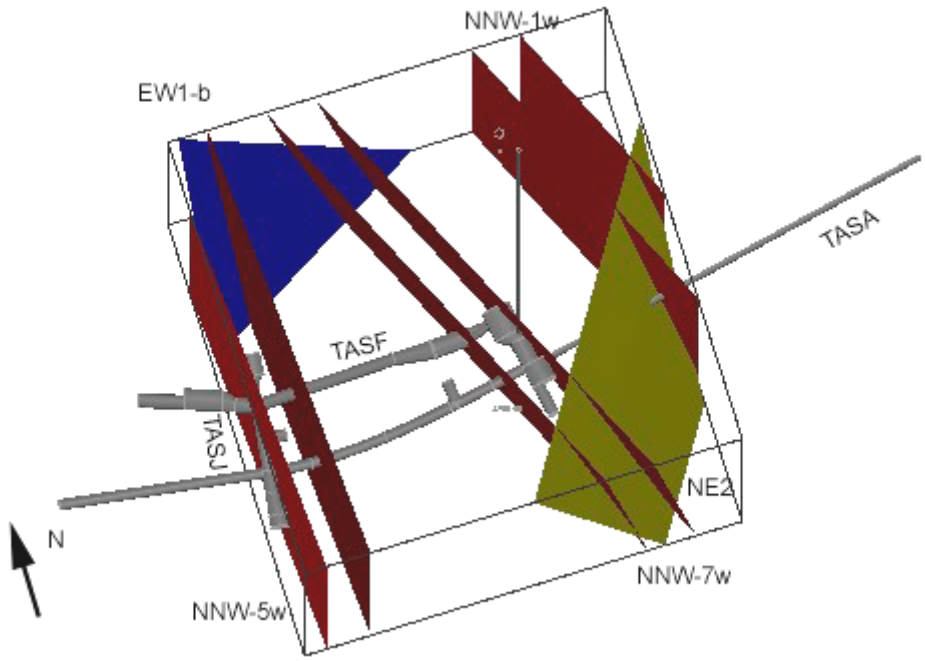

Figure 2-13. *Model of regional structures identified within the 200-m model domain*

Major hydraulic conductors that have been mapped at the Äspö site are mostly striking NNW-NW and dipping between 80°NE to 90°. Some of these hydraulic conductors present a clear increase of fracture frequency but some are rather diffuse and called fracture swarms (Stanfors *et al.*, 1997). However NNW-NW hydraulic conductors have been identified by interference tests in boreholes drilled from surfaces, and some are eventually mapped in the tunnel (Rhén *et al.* 1997). Three of these major structures are possibly going through the 200-m model: NNW-1w, NNW-5w and NNW-7w. The existence of feature NNW-1 is supported by a number of indications in the Äspö HRL, the existence of features NNW-5 and NNW-7 are supported by few indications and the features should be considered as possible (Rhén *et al.*, 1997). Their main characteristics are presented in Table 2-17. The width of these three structures is estimated to 20 m (uncertain values, or based on expertise judgment given in Rhén *et al.*, 1997). It seems more appropriate to call them hydraulic conductors rather than "fracture zones" as no clear identification of tectonic constraints have been reported. Nevertheless the vertical extension of these zones is highly uncertain.

Table 2-17. Interpreted hydraulic conductors at the Äspö site scale that intersect the 200-m model

ID	Strike	Dip	Mean T (m^2/s)	Comments	Data source
NNW-1w	143.7	90	8.6E-06	Certain conductive structure	Rhén *et al.*, 1997
NNW-5w	164.7	90	4E-06	Possible conductive structure	Rhén *et al.*, 1997
NNW-7w	323.2	85° NE	7.5E-06	Possible conductive structure	Rhén *et al.*, 1997

Strike and dip are extracted from RVS, the surfaces have been modeled from point coordinates (after Rhén et al., 1997).

The visualization of these hydraulic conductors according to their given geometry is presented in Figure 2-13.

2.6.2 Main structures at site scale

Beside these major structures one minor fracture zone, z4, and three water-bearing features, called WNW-1, WNW-2 and WNW-3, have been identified in the 200-m model. The description of the different structures is presented in this section.

Minor fracture zone z4

The main indications of the minor fracture zone z4 in tunnels or boreholes in the 200-m model are listed in Table 2-18.

The fracture zone z4 is mapped and clearly identified in TASF Ch.10 and TASJ Ch.20-30 (Table 2-18), and west of the model boundary in TASA Ch. 3520 (Rhén, 1995).

Table 2-18. Identification of the minor fracture zone in the 200-m model

ID	Mapped occurrences	Identification	Orientation	Source of data
Zone Z4	TASF, Ch. 10	Fracture zone, 0.5 to 3 m wide	NE sub-vert.	PR 25-95-28
Z4	TASJ, Ch. 20-30	Fracture zone, 1.5 to 3.3 m wide	NE sub-vert.	PR 25-95-28
Z4	KJ0044A01 L=16.7-17.26 m (end of the hole)	Mylonitic structure	No orientation	SICADA
Z4	KA2598A Section between 71 and 76 m	RQD=45 (71-72 m) Brecciated and tectonized structure	No orientation	SICADA
Z4	KF0066A01 L=42-43 m	Crush zone, Foliated hydride rock	No orientation	SICADA
Z4	KF0069A01, L=52.88 and L=53.14 m	Foliation	61/73.7 and 61.9/80.6	SICADA
Z4	KF0093A01	Foliation L=17 m	No orientation	SICADA

This zone exhibits shear-zone characteristics and is as such a dominant structure in the domain. Complementary data from boreholes in the 200-m model can be interpreted as an indication of the extension of the zone:

– KJ0044F01: Mylonitic structure at L=16.7 to L=17.26 m.

– KF0093A01: The diorite is schistose from L=30.59 to L=36.05 m.

– KF0066A01: The RQD is low at L=43-44 m, and is correlated to the occurrence of a crush zone. Nevertheless the core does not seem so loose when looking at the BIPS images. The crushed and fractured section is located in foliated hybrid rock. This crush sections is dry according to the flow measurements, see section 2.5.2.

– KA2598A: the section from 71 to 76 m shows an increased fracturing, and the RQD is low (45) at L=71-72 m. This section is located in tectonized and brecciated aplite.

– TASA, Ch.2740: there is a mapped indication of fracture zone, identified as z2 in Stanfors *et al.*, 1994, which can be associated to fracture zone z4. This mapped fracture zone is less than 1-m wide and strike to the NE. This indication is not located within the model boundary but is used as a lead to modeling the fracture zone.

The new indications of the zone in boreholes KF0066A01 and KF0069A01 consolidate the hypothesis that the zone might bifurcate to the E-NE towards the major fracture zone NE2. Hence this has been taken into account in the modeling of the fracture zone in RVS, and the zone has been modeled in two sections, one striking NNE at the SW corner of the model, the other section striking ENE towards the Eastern boundary of the model, see Table 2-19.

Table 2-19. Characteristics of the modelled minor fracture zone z4

	Strike, °	Dip, °	Indications
Z4_NNE	28.3	77	TASA Ch.3520, TASJ, TASF, KJ0044F01, KA2598
Z4_ENE	49.4	67.4	KF0066A01, KF0069A01, KF0093A01, KJ0044F01, TASA Ch.2740

The points used for defining the best fitting planes of both sections of the zone are visualized in Figure 2-14. The indications in tunnels and boreholes suggest that the zone is between 1 and 4 m wide.

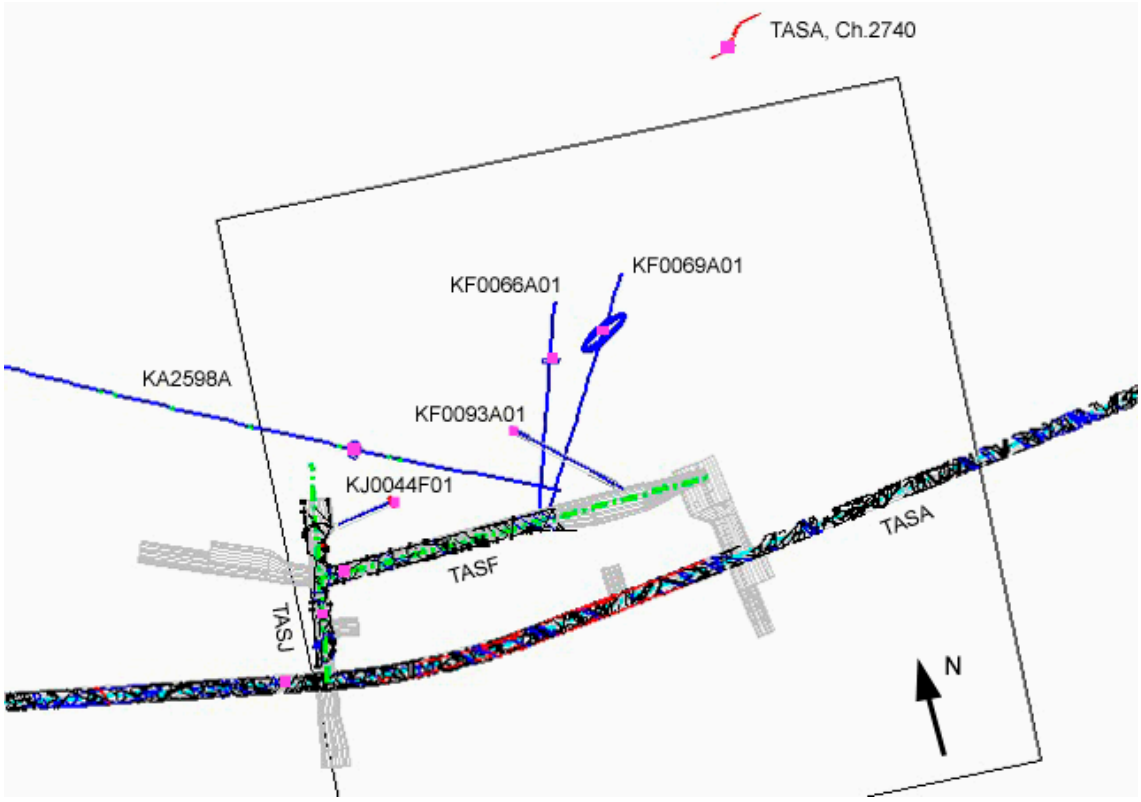

Figure 2-14. *Top view of the model: visualization of the points used for the identification and modeling of z4. The remarkable features are visualized as cylinders, and the intersection points are represented by the purple squares.*

The modeled minor fracture zone z4 is visualized in Figure 2-15. The intersection of the minor zone z4 and the major fracture zone NE2 might be located some hundred meters beside the NE boundary of the model.

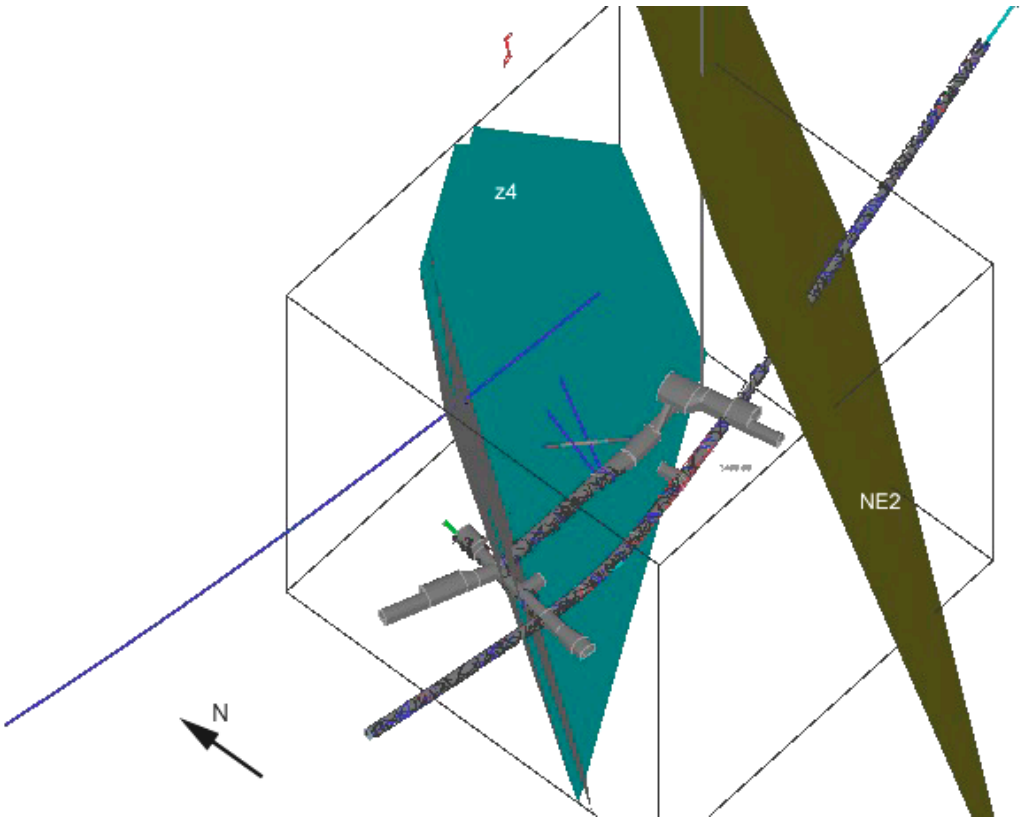

Figure 2-15. *Side view of the 200-m model with the modeled minor fracture zone z4.*

Few information are found on hydraulic conductivity in this minor fracture zone. The indications of the zones identified along KF0066A01 and KF0069A01 represent dry sections. Water inflow is recorded in KA2598A between L=73.5 and 75.3m, which correspond to the intersection depth of the interpreted zone. No flow logging data are available in boreholes KJ0044F01 and KF0093A01.

In both TASF and TASJ tunnels NW conductive fractures are mapped aside of the indication of the z4 fracture zone, see Rhén (1995), but no further indication is provided.

NW-hydraulic "fracture swarms"

In consideration of the three investigated experiment volumes three "main" WNW fracture swarms can be identified in the 200-m model. In the preliminary analysis the extension of WNW-2 and WNW-3 has been limited to the West to the minor fracture zone z4 and to the East to the major fracture zone NE2. The extension to the East of the hydraulic conductor WNW-1 can be discussed as indications of this structure are identified on both sides of NE2, and as this conductor might be correlated to the large scale NNW-1w hydraulic conductor, see the description of this conductor further down.

As the vertical extension of these hydraulic conductors is uncertain they have been modeled as 2D objects in the planes of indication points.

The three hydraulic conductors and their indications in the 200-m model are presented in the next sections.

- WNW-1

This structure is striking WNW and is located in the NE corner of the 200-m model. In the model domain this conductive feature is underlined by a swarm of fractures mapped in TASA, Ch.3310-3315, and conductive sections/points in boreholes KA3191F and KA3376B01, see Table 2-20. Several water inflows are measured in borehole KA3376B01, which is located North of TASA in line with the possible hydro-structure, see Figure 2-17. Several inflow points with a high inflow rate are identified between L=49 and L=57 m. The distance from the mapped water conductive fractures in TASA to the conductive sections in the borehole is around 47 m. Natural fractures that might cause the inflow has been identified in section 2.5.2.

Table 2-20. Identification of the hydraulic feature WNW-1 in the 200-m model

ID	Mapped occurrences	Identification	Orientation	Source of data
WNW-1	Ch.3310-3315 TASA	4 single open water-bearing fractures	NNW, sub-vertical	PR 25-95-28
WNW-1	KA3191F, L=123.58 and L=124.1 m	Radar reflector Natural fractures Crush zone (<1 m)	111/82 see Table 2-14	Rhén *et al.* 1995 SICADA
WNW-1	KA3376B01 L=49-56	Inflow likely correlated to several open fractures	See Figure 2-12 and Table 2-8	SICADA

The poles to planes of conductive fractures mapped in TASA, Ch. 3304-3319, as well as the poles to possible conductive features in boreholes KA3191F and KA3376B01 are plotted in Figure 2-16. The plot of fractures shows a clear trend for the orientation of fractures: most are striking WNW, with a dip between 80 and 90°.

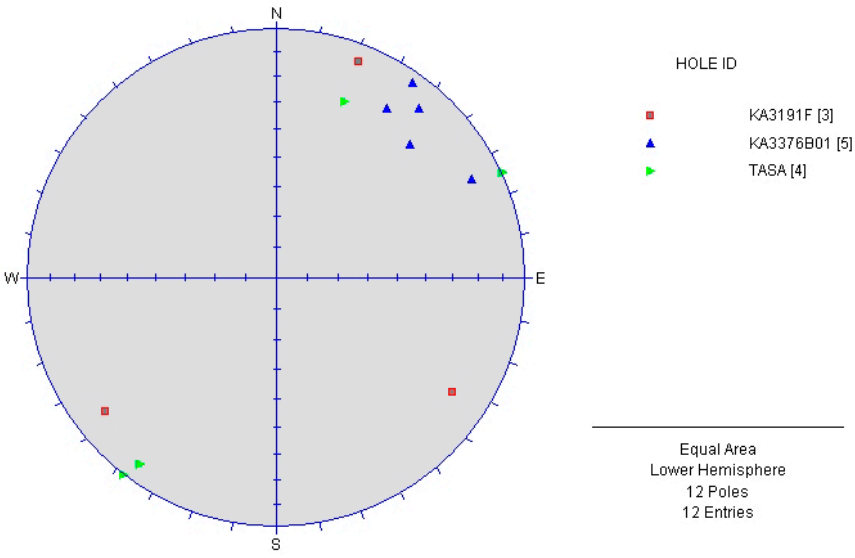

***Figure 2-16**. Point plot of poles of potential water-conductive fracture planes identified as indications of WNW-1.*

The visualization of the interpreted conductive feature WNW-1 is presented in Figure 2-17. The structure is modeled by drawing the best fit plane between the identification points listed in Table 2-20. The interpreted feature has a strike of 308° and a dip of 85°.

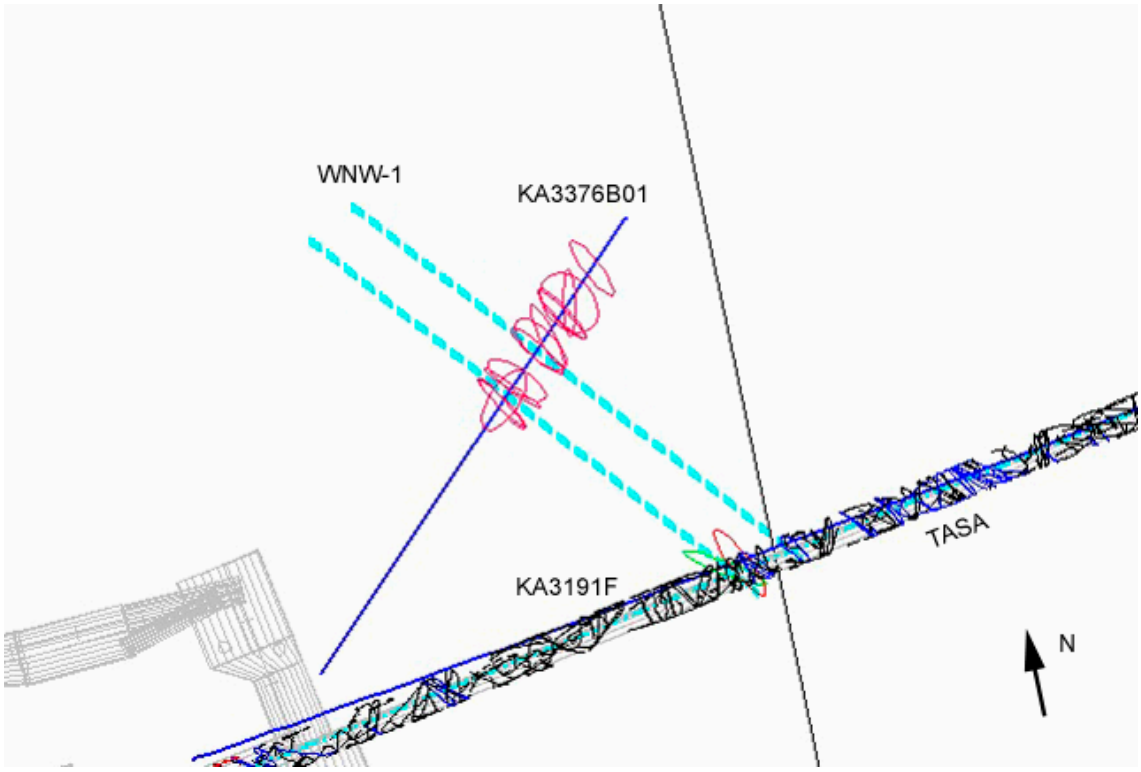

***Figure 2-17.** Detailed top view of hydraulic feature, WNW-1 in the 200-m model. The discs are representing the potential conductive fractures; the green disc is illustrating the orientation of the reflector.*

The hydraulic feature WNW-1 is located at the vertical of the regional hydraulic conductor NNW-1w, see section 2.6.1. The identification of structure NNW-1w is considered certain at the surface and confirmed from interference tests in KA2162B (Rhén *et al.*, 1994) and KC0045F (Olsson *et al.*, 1994). These inflow points are located respectively at -321m and -369m depth, whereas the identification of the local feature WNW-1 is based on observations made around -440/-450m.

The orientation planes of both structures are plotted on a lower hemisphere equal area stereoprojection illustrated in *Figure 2-18*. The orientation of structure NNW-1w is taken from Table 2-17.

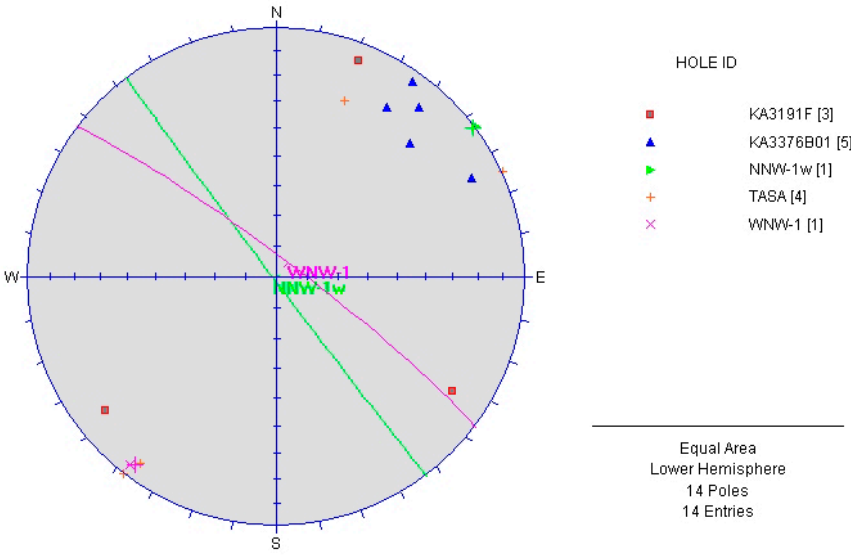

Figure 2-18 *Stereoplot of orientation planes of conductive features NNW-1w and WNW-1.*

Olsson *et al.* (1994) describes NNW-1w as structures most probably consisting of interconnected steep fractures striking NS to WNW, and forming conductors striking NW. Hence the conductive structure WNW-1 interpreted at depth in the 200-m model domain might be an indication of the regional hydraulic conductor NNW-1w.

- WNW-2

This feature is identified by fracture swarms both in TASA, Ch.3440-3450 and in TASF, Ch. 20-30. The existence of this feature is enhanced by a conductive section in the borehole KA3386A01, see Table 2-21.

Table 2-21. Identification of the hydraulic feature WNW-2 in the 200-m model

ID	Mapped occurrences	Identification	Orientation	Source of data
WNW-2	TASA ,Ch.3440-3450	4-5 water-bearing fractures	NNW, sub-vertical	PR 25-95-28
WNW-2	TASF, Ch. 20-30	2-3 water-bearing fractures	NNW, sub-vertical	PR 25-95-28
WNW-2	KA3386A01, L=32.3-40m	3 water-bearing fractures	See Table 2-7	SICADA

The elongation of the WNW-2 structure as defined from tunnel indications towards the SE of the model crosses three main water inflow points in borehole KA3386A01 between L=36 to L=41 m, see Figure 2-19. The orientation of the natural fractures that are likely to be correlated to the inflow in the borehole are also concordant to the main direction of the structure, see Figure 2-20.

The orientation of water-bearing fractures mapped in both tunnels are consequent and the relative small distance between the design lines support the persistency of these fractures and the occurrence of this conductive structure. The interpreted structure has a trend of 302° and plunge 85°.

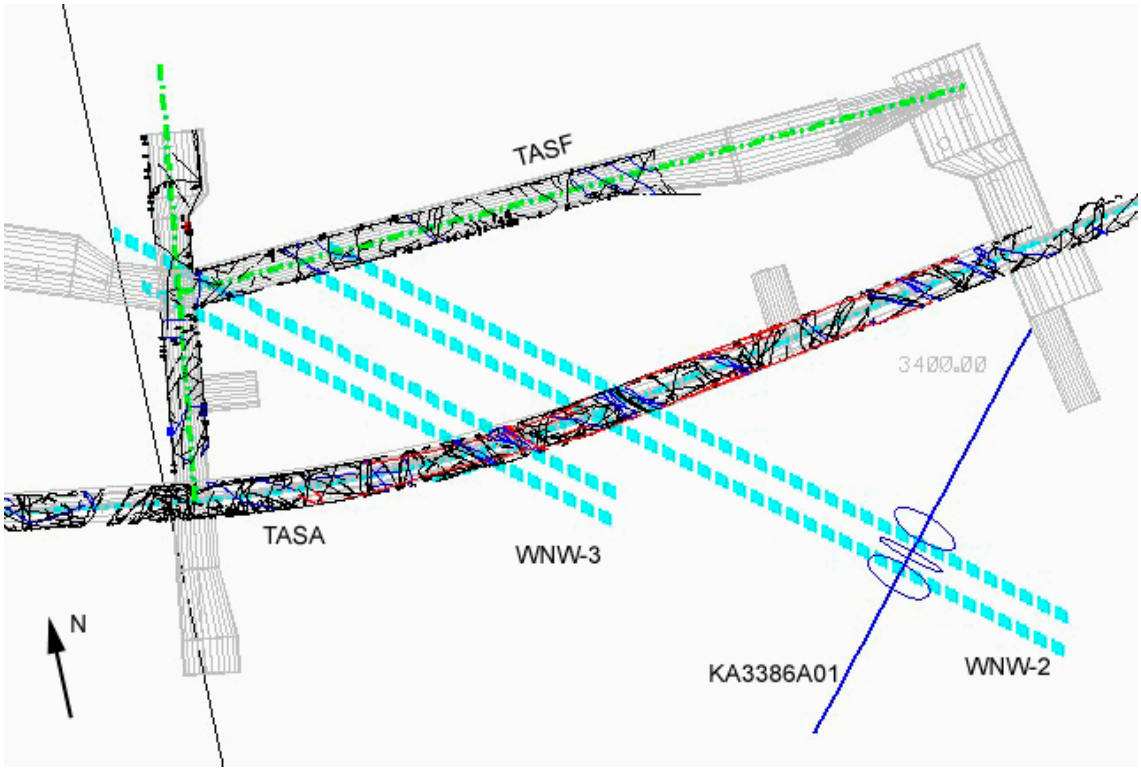

Figure 2-19. *Detailed top view of the hydraulic features WNW-2 and WNW-3. The discs represent potential conductive fractures.*

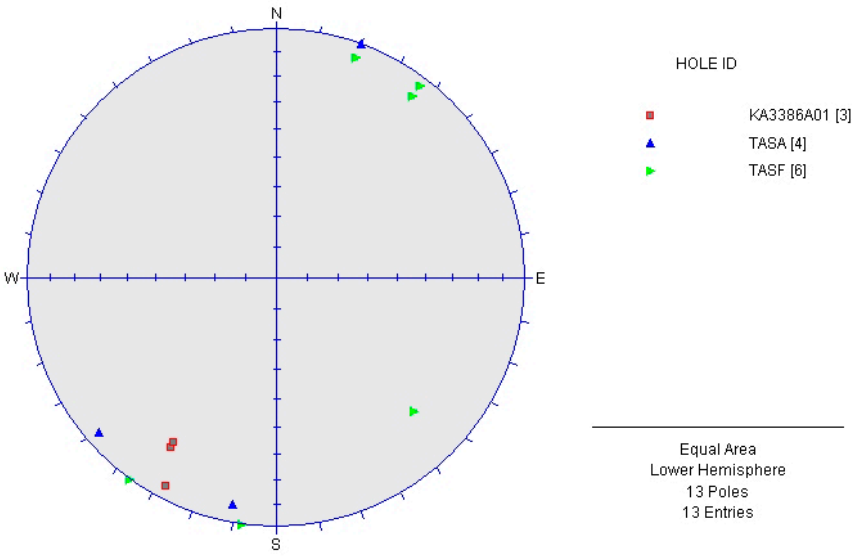

Figure 2-20. *Stereoprojection of the water-conductive fractures in the zone of WNW-2.*

- WNW-3

This feature is interpreted from the intercept in TASA at Ch.3460-3470 and TASF at Ch.0-10, see Table 2-22. The water-bearing fractures mapped in both tunnels are striking to the WNW and are almost sub-vertical (Figure 2-21). The orientation of fractures in WNW-3 is similar to the orientation of the fractures identified to belong to the structure WNW-2, see Figure 2-20.

Table 2-22. Identification of the hydraulic feature WNW-3 in the 200-m model

ID	Mapped occurrences	ID, width, min.	Orientation	Source of data
WNW-3	TASA , Ch.3460-3470	4-5 single open water-bearing fractures	NW, sub-vertical	PR 25-95-28
WNW-3	TASF, Ch. 0-10	2 single open water-bearing fractures	NW, sub-vertical	PR 25-95-28

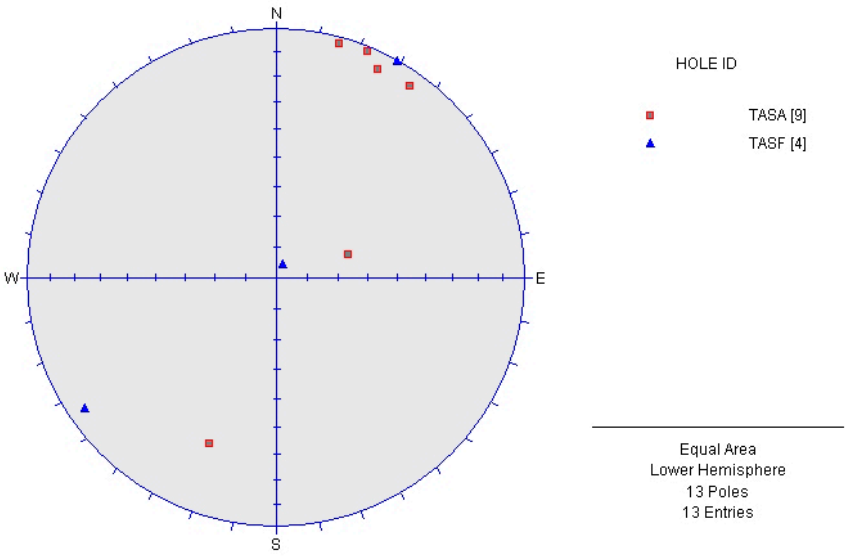

Figure 2-21. *Point plot of potential water-conductive fractures identified as indications of WNW-3 in the 200-m model.*

2.6.3 The hydro-structural 200-m model

The hydro-structural model achieved in this section is illustrated in *Figure 2-22*. The development of the hydro-structural model has been first based on the interpretation of flow data from boreholes KA0066A01, KF0069A01, KA3386A01 and JA3376B01, drilled in connection to the Äspö Pillar Stability Experiment.

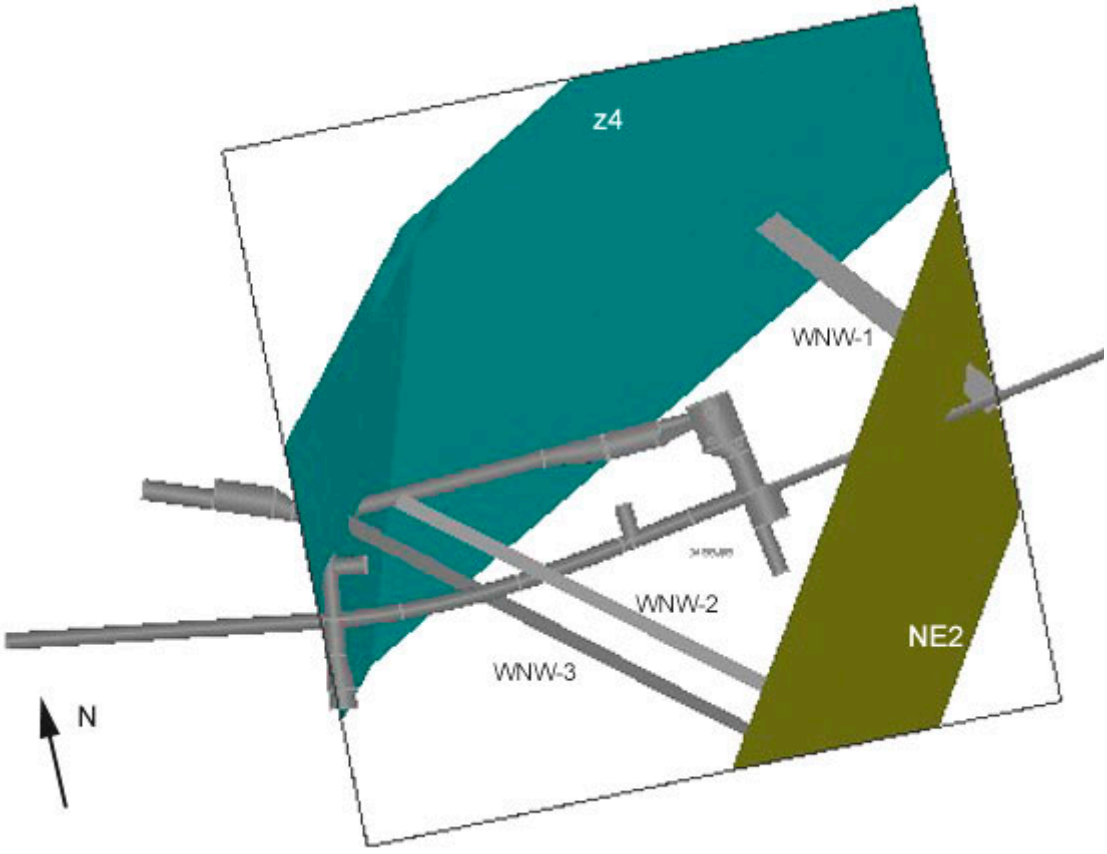

Figure 2-22. *Overview of the hydro-structural model.*

Three WNW hydraulic structures have been identified at the domain scale. The longitudinal and vertical extension of these structures is uncertain, and it had been assumed at first that they would end towards the North at the minor fracture zone z4, and towards South at the major fracture zone NE2. Nevertheless mapped indications in tunnels show that the conductive fractures intersect z4 and do not terminate at the zone. Moreover indications of WNW-1 are identified on both sides of NE2.

The relation / connectivity of these structures to the previously mapped local and regional structure has also been studied.

The hydraulic structures identified in the 200-m model domain are striking WNW whereas the regional structures presented in section 2.6.2 are striking NW-NNW, see Figure 2-23.

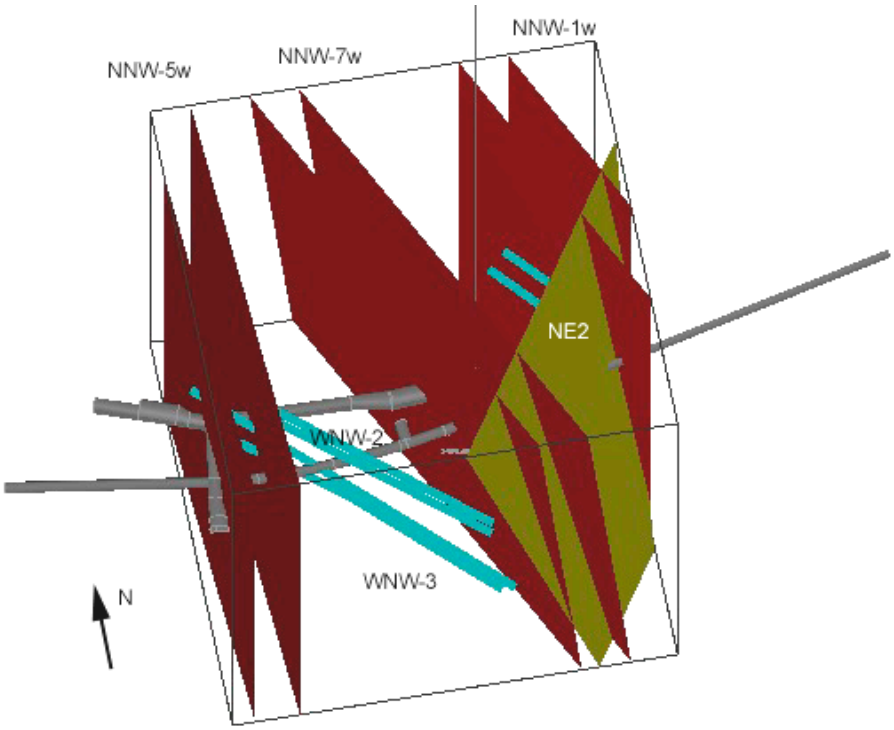

Figure 2-23. *Visualization of the local interpreted hydraulic features and of the regional hydraulic conductors.*

As mentioned in section 2.6.2, and illustrated in *Figure 2-18*, the site scale WNW-1 structure might be an indicator at -400/-450m depth of the regional NNW-1w. This structure might be interpreted as a branch interconnected to the major structure.

Indications of the regional structures NNW-5w and NNW-7w, see section 2.6.2, are not clearly found in the model domain. However the water inflow at L=10 m in KA3386A01 is located at the western border of the interpreted structure NNW-7w, and might be an indication of the occurrence of this structure at depth. The fractures identified as potential candidates for this inflow are striking NNW and are sub-vertical.

Some other deterministic conductive structures have been previously identified at depth in the TRUE Block Scale volume and its closed surrounding, see Andersson, P. *et al.* (2002). These are located near the SW corner of the model boundary. Some general comments can be made regarding the relation of these structures to the previously presented structures identified in the 200-m model:

– The structure#8 is almost parallel to the ENE section of the minor fracture zone z4.

– Structure#1 is a sub-vertical NW conductor that intersects z4 at top of the 200-m model.

– Structures#2, 3 and 4 are identified as almost W-E to WNW sub-vertical conductors. Structure#4 is sub-parallel to the identified structures WNW-2 and WNW-3.

The characteristics of the cited structures that are going through the 200-m model are summarized in Table 2-23. Trend and plunge of the interpreted structures have been calculated from the geometry of the intercepts in boreholes.

Table 2-23. Intercepts in the 200-m model and geometry of the conductive structures identified in the TRUE Block Scale boreholes

ID	Intercepts in the 200-m model				Structure geometry			
	Depth	Strike	Dip	Hole	Trend	Plunge	Comments	Data source
1	12.5	335	82	KA2563A	335	82		TR-02-13
2	68.5	135	87	KA2563A	279.6	61.4		TR-02-13
3	68.5	135	87	KA2563A	267.2	53.7		TR-02-13
4	94.4	296	74	KA2563A	299.1	48		TR-02-13
	23.1	300	80	KA2511A				TR-02-13
8	242.4	26	84	KA2563A	208	22.8		TR-02-13

The visualization of some of these structures is presented in Figure 2-24.

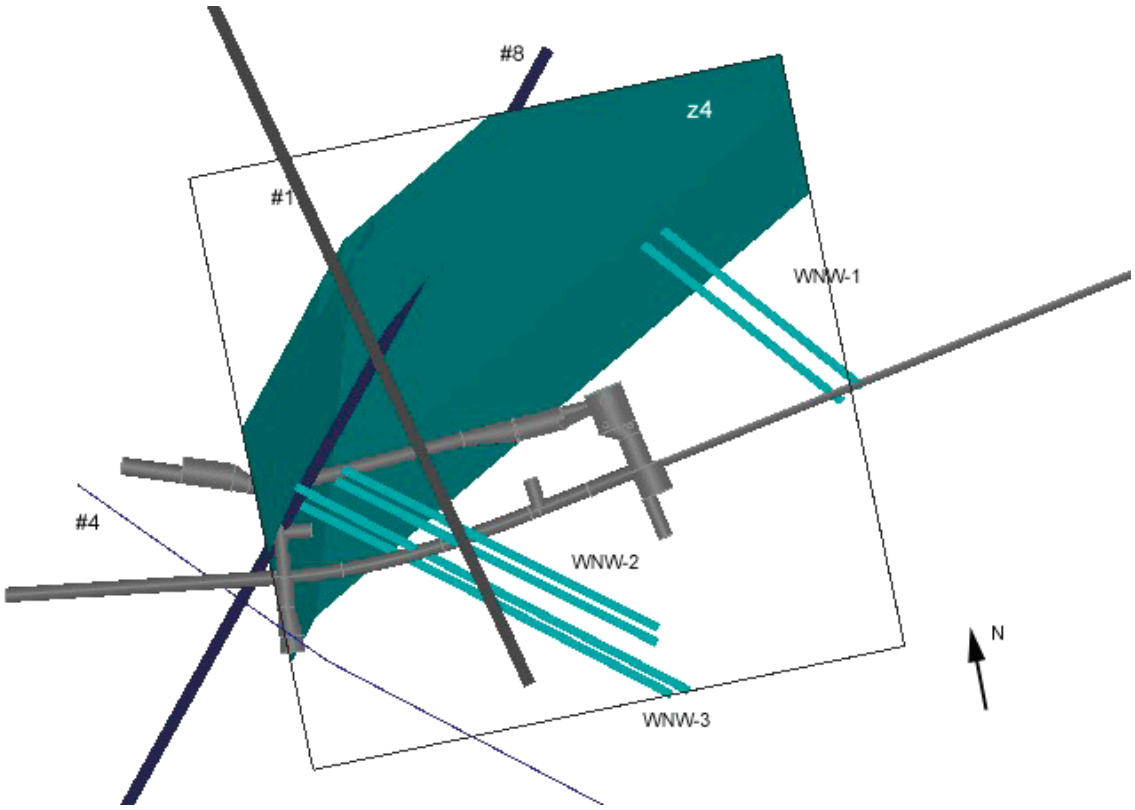

Figure 2-24. *The hydro-structures identified in TRUE Block Scale, and their relation to the structures identified in the 200-m model, top view. Note: the different structures are at different depths and do not intersect.*

The further identification and characterization of the WNW-1w hydraulic structure is of importance for the localization of the experiment, especially if it can be confirmed that this structure is an indication of NNW-1w at depth. The connectivity of the fractures in WNW-1 hydraulic structure to other structures such as fracture zones NE2 and z4 in the model is important to investigate. The hydraulic conductivity and connectivity of z4 might in this case be a significant parameter to establish.

3 Initial stresses

This section provides *in situ* stress measurement results and their interpretation in the experimental volumes.

3.1 In situ stress measurements

3.1.1 General

Stress measurements have been conducted in four boreholes located closed to the three experimental volumes that are KA2599G01, KF0093A01, KAS02, and KA3579G (see Figure 3-1 to Figure 3-3). All measurements at that depth in these boreholes are located inside the same "rock unit" block, which is delimited by fracture zones EW-1b and NE-2, see Figure 3-1. This block is identified as block H according to the geological model (see Figure 3-4). Outside the block and at levels -450 m and -480 m stress measurements are also available in one borehole, KKG0045G01.

In borehole KA2599G01 two stress measurement methods have been applied: one overcoring method, Deep Doorstopper Gauge System (DDGS), and hydraulic fracturing (HF). In borehole KF0093A01 stress measurement have be performed with three methods: two overcoring methods, DDGS respective Borre Probe, and hydraulic fracturing.

Only one method has been used for the 3 other boreholes, which is hydraulic fracturing in borehole KAS02, overcoring (method Borre Probe) in boreholes KA3579G and KK0045G01.

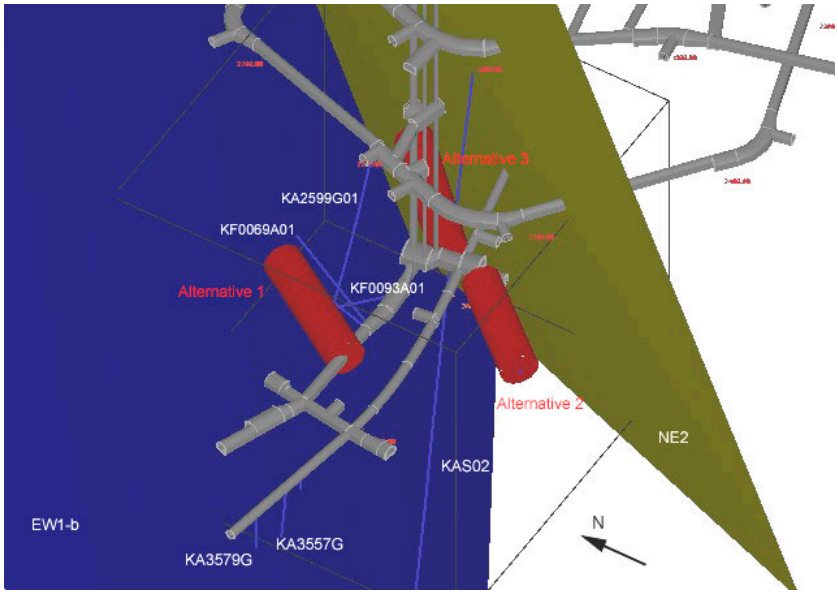

Figure 3-1. *Side view of the 3 experiment volumes (red cylinders), their localisation towards the regional fracture zones and the boreholes providing stress measurements.*

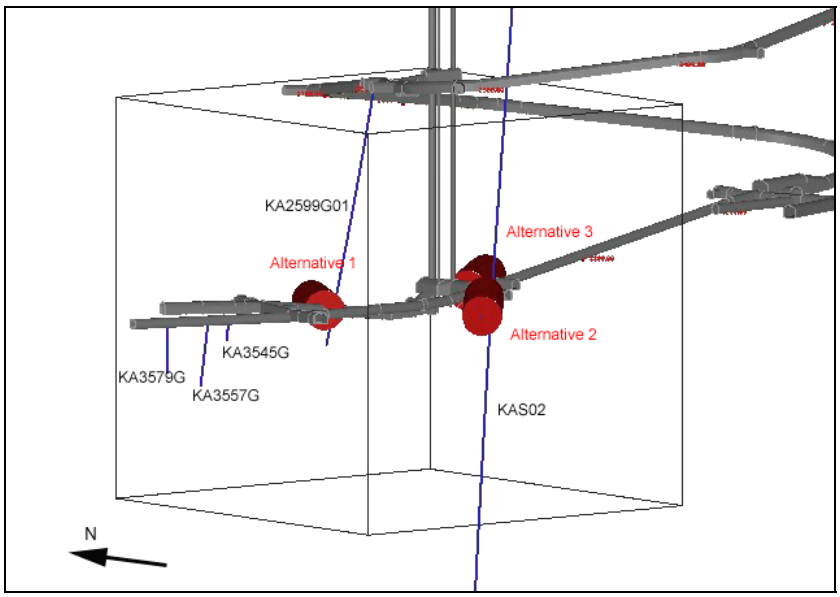

Figure 3-2. *Side view of the 3 experiment volumes (red cylinders), and their localization towards the boreholes providing stress measurements.*

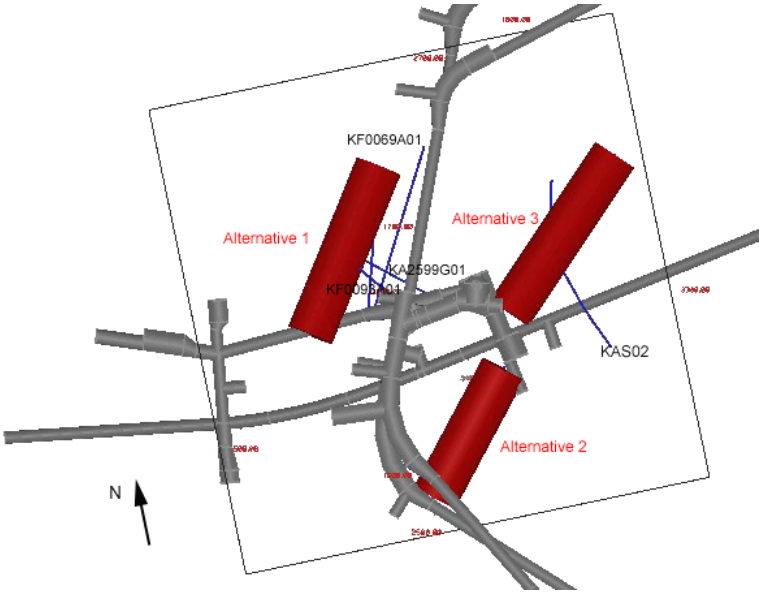

Figure 3-3. *Top view of the 3 experiment volumes (red cylinders), and their localization towards the tunnel and the boreholes providing stress measurements.*

The DDGS method is a 2D method that gives the state of stresses perpendicular to the borehole. The hydraulic fracturing method gives directly the minimum stress perpendicular to the borehole and secondly, after theoretical assumption, the maximum stress perpendicular to the minimum stress. The tested boreholes are either vertical or horizontal.

The analyses of field measurement results of *in situ* stresses are presented in both horizontal and vertical stress components, and principal stresses. In the presentation of the horizontal and vertical stresses a complete comparison could be done between the different stress measurement methods. In the presentation of the principal stresses the results are exclusively based on interpretation of the Borre Probe test measurements.

The presented results, see Table 3-1 to Table 3-3, are based on data from Klasson *et al.* (2000), and Janson and Stigsson (2002).

3.1.2 Results

The stress measurement results are summarized in Table 3-1, for the minimum horizontal, the maximum horizontal and the vertical stresses.

Table 3-1. Summary of the measured stresses in the vertical and horizontal plane, for all five boreholes

	Method and borehole	Min horizontal stress, MPa	Max horizontal stress, MPa	Trend max horizontal stress (Äspö96)	Vertical stress, MPa
Inside the block H	***DDGS, KA2599G01***	22.2 ± 0.6	36.7 ± 2.6	126^{o}	-
	HF, KA2599G01	11.0 ± 1.2	21.8 ± 4.5	130^{o}	-
	DDGS, KF0093A01	12.4 ± 0.3	-	-	32.6 ± 5.6
	Borre Probe, KF0093A01	10.2 ± 2.1	25.8 ± 3.5	125^{o}	18.0 ± 8.8
	HF, KF0093A01	11.0 ± 1.4	-	127^{o}	19.8 ± 1.6
	HF, KAS02	14.2 ± 1.8	25.0 ± 3.0	142^{o}	-
	Borre Probe, KA3579G	13.3 ± 2.6	34.1 ± 9.5	141^{o}	17.6 ± 3.5
Outside the block H	***KKG0045G01, -450m***	11.0 ± 2.4	18.8 ± 2.6	162^{o}	14.1 ± 3.6
	KKG0045G01, -480m	13.5 ± 4.5	25.9 ± 3.6	127^{o}	15.5 ± 4.7
	Theoretical	-	-		12.2

From results provided in Table 3-1, the following state of stress is obtained in the "rock unit" block H (Janson and Stigsson, 2002). The minimum horizontal stress is between 11±2 MPa. The maximum horizontal stress is 24 ±5 MPa most likely within the upper range and the orientation of the maximum stress is about 130^{o} from local north. The vertical stress is between 17±3 MPa.

Table 3-2 presents magnitudes of the principal stresses measured at different depths in two boreholes, KF0093A01 and KA3579G by the Borre Probe method. Table 3-3 presents the corresponding principal stress orientation - measured in the same boreholes KF0093A01 and KA3579G by the Borre Probe method, at the same depths.

Table 3-2. Values of principal stress magnitude in boreholes: KF0093A01 and KA3579G

Borehole	σ_1 (MPa)	σ_2 (MPa)	σ_3 (MPa)
KF0093A01	32.5	13.8	8.7
KF0093A01	36.0	17.7	8.9
KF0093A01	23.2	14.2	6.9
Average KF0093A01	**29.8**	**14.8**	**9.4**
KA3579G	34.5	17.6	11.4
KA3579G	29.0	15.1	11.0
KA3579G	43.7	20.5	15.8
KA3579G	30.4	18.2	12.7
Average KA3579G	**34.2**	**17.7**	**13.1**

Table 3-3. Results of the principal stress orientations in boreholes: KF0093A01 and KA3579G. All orientations are given in the Äspö local co-ordinate system (Äspö96)

Borehole	σ_1 Trend/plunge	σ_2 Trend/plunge	σ_3 Trend/plunge
KF0093A01	307/38	096/48	204/16
KF0093A01	310/38	114/51	214/08
KF0093A01	308/10	044/30	204/58
Average KF0093A01	**310/31**	**088/52**	**206/21**
KA3579G	138/01	034/86	229/04
KA3579G	150/00	240/60	060/30
KA3579G	135/02	238/80	044/09
KA3579G	145/10	276/76	053/11
Average KA3579G	**141/03**	**245/80**	**050/10**

The average magnitudes have been obtained by transformation of all applicable results to one co-ordinate system, and then by solving the average stress tensor for its eigen values. Plunge is defined as being zero in the horizontal plane.

The magnitudes presented in Table 3-2 are in the same range in the both boreholes. The major principal stress is between 25 to 35 MPa, the intermediate principal stress is between 14 to 20 MPa and the minor principal stress is between 8 to 12 MPa.

Table 3-4 presents the average magnitudes of the measured principal stresses and orientations at different depths in borehole KKG0045G01, which is located further away from the experimental volumes and outside the “rock unit” block H.

Table 3-4. Values of principal stress magnitude and orientations in borehole KKG00445G01

Stress component	*Depth – 450 m*	*Trend/plunge*	*Depth – 480 m*	*Trend/plunge*
σ_1 *(MPa)*	22	146/35	27	122/20
σ_2 *(MPa)*	15	030/32	17	012/43
σ_3 *(MPa)*	7	270/039	10	230/40

At the experimental volume areas the principal stress orientations seem not to follow the horizontal and vertical plane, see Table 3-3. The stress orientations in the experimental volumes are for the major principal stress between 310/10 and 310/40, for the intermediate principal stress between 045/30 and 115/50 and for the minor principal stress between 200/10 and 215/60.

3.1.3 Discussion

In the Simpevarp domain, which includes Oskarshamn, Laxemar and Äspö HRL, a lot of *in situ* stress measurements have been performed. In the frame of the SKB project "Geomod" the measurement data from different methods that are available in this domain were analyzed and interpreted. The data set includes data from both boreholes located in the experiment volumes. The results of the analyses are presented in a model for *in situ* stress magnitudes and orientations (SKB, 2002).

Hence the results in Table 3-2 and Table 3-3 could be compared with the results obtained from the developed Simpevarp *in situ* stress model. At level –450 m the model gives a magnitude for the major principal stress of 32.7 MPa and an orientation of 132/00, the magnitudes of the intermediate principal and minor principal stress are respectively 12.1 MPa and 10.9 MPa. The orientation of the intermediate and minor principal stress follows the orientation of the major principal stress in the horizontal and vertical plane.

3.2 Numerical stress calculations

In the SKB project "Strategy for a rock mechanical site descriptive model" Hakami *et al.* (2002) have studied the differences in stress values between the different "rock unit" blocks identified in the Äspö HRL volume, see *Figure 3-4*. The simulations were conducted by using the distinct element code 3DEC. The "rock unit" blocks are delimited by fracture and shear zones in the model cube. Both experimental volumes are included in block H that forms a wedge, and due to the geometry higher stresses are simulated in this block compared to stresses simulated in the surrounding blocks at the same depth level. The results of the numerical calculations are presented in Table 3-5.

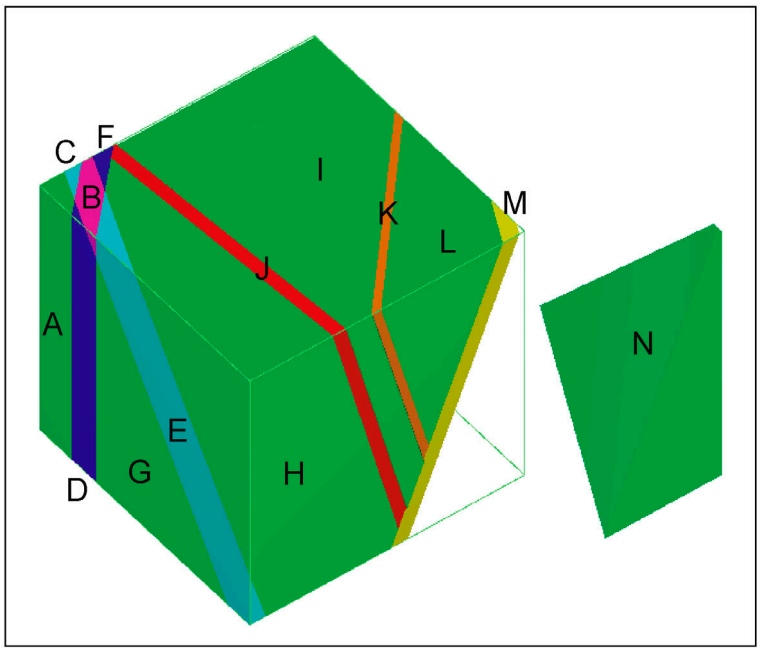

Figure 3-4. *Presentation of the "rock unit" and "deformation zone" blocks in the rock mechanical site descriptive model.*

Table 3-5. Principal stresses from the 3DEC numerical calculations in the block including the experimental volumes

	σ_1	σ_2	σ_3
Magnitude (MPa)	25	15	12
Trend (Äspö 96)	150	-	-
Plunge (°) from the horizontal plane	03	35	55

An analysis of the mechanical conditions in the Äspö HRL tunnels has also been done (Andersson C. *et al*., 2002). The calculations are done with the numerical program Examine3D. The results from the calculation were compared with the tunnel observation and support performance, and are in good agreement. The *in situ* stress values used as input data for the simulations at the experimental volumes' level are presented in Table 3-6. The input data in Table 3-2 give also a good indication of the *in situ* stress situations in the Äspö HRL.

Table 3-6. Input stress data for the numerical calculations of the stress situation in the Äspö tunnel at level –450m

	σ_1	σ_2	σ_3
Magnitude (MPa)	29	21	10
Trend (Äspö 96)	133°	49 °	234 °
Plunge (°) from the horizontal plane	19	42	33

3.3 Conclusions

The major principal stress and orientation in the "rock unit" block H, where the three experimental volumes are located, differ from the surrounding blocks. The discrepancy could be observed both from the stress measurements in boreholes and from results of the 3DEC numerical calculations. This difference might be due to the wedged form of this block H (see Figure 3-4).

The *in situ* stress measurements available that have been evaluated in this report are close to the experiment volume 1. As no measurements closed to the experiment volumes 2 and 3 are actually available, and taking into account that both experiment volumes are located in the same "rock unit" block, it is assumed in the first stages of modeling that the state of *in situ* stresses is identical in both experiment volumes.

In order to assess the influence of stress values on the model three sets of data for principal stresses are defined in the experimental volumes on the basis of the measurements evaluated in the previous sections. The major principal stress is the only parameter that is changed in the different sets. The reason for varying exclusively major principal stress is that the experimental tunnel is perpendicular to the orientation of the major principal stress. Consequently the major stress gives the largest effect on the experiment. The principal stresses in the experimental volumes are estimated as:

Group I, based on the most probable value of major stress:

σ_1: 30 MPa and an orientation of 310/30 (Äspö96)
σ_2: 15 MPa and an orientation of 090/53 (Äspö96)
σ_3: 10 MPa and an orientation of 208/20 (Äspö96)

Group II, based on the lowest value of major stress:

σ_1: 25 MPa and an orientation of 310/30 (Äspö96)
σ_2: 15 MPa and an orientation of 090/53 (Äspö96)
σ_3: 10 MPa and an orientation of 208/20 (Äspö96)

Group III, based on the highest value of major stress:

σ_1: 35 MPa and an orientation of 310/30 (Äspö96)
σ_2: 15 MPa and an orientation of 090/53 (Äspö96)
σ_3: 10 MPa and an orientation of 208/20 (Äspö96)

4 Preliminary mechanical and thermal properties of the rock mass

This section presents the preliminary mechanical and thermal properties of the rock that are expected in the experimental volumes.

The evaluation of the parameters is made on the basis of information from previously drilled boreholes (Note: no mechanical or thermal investigations have been done at this stage on samples from boreholes KF0066A01, KF0069A01, KA3386A01 and KA3376B01, which have been drilled in connection to the Pillar experiment). Two boreholes, KA2599G01 and KF0093A01, are crossing the experiment volume of alternative 1 but none is going through the experiment volumes of alternatives 2 and 3. Complementary data are supplied from several boreholes in the surrounding volumes, see Table 4-1. Detailed views of the experimental volumes and the localization of boreholes used for the determination of mechanical and thermal properties are presented in Figure 3-1 to Figure 3-3.

Table 4-1. Nature of data analyzed in nearby boreholes

	Type of data
KA2599G01	fracture frequency and orientation, thermal properties, density, lithology
KF0093A01	fracture frequency and orientation, lithology
KA3579G	lithology
KAS02	fracture frequency and orientation, mechanical properties, lithology
KA3545G	mechanical properties
KA3557G	mechanical properties

On the eve of the initial analyses of the experiment with a numerical 2-D model, a number of mechanical and thermal properties are required. The preliminary properties are determined on results provided by earlier investigations at Äspö HRL. The preliminary properties should later be updated during the project when detailed investigations are performed during drilling in the experimental volume.

4.1 Geology and structure in the rock mass

The geology and structures at the site scale around the 3 experiment volumes have been studied and discussed in section 2.

This chapter will shortly give information on geological, and structural data on the basis of specific data provided by detailed geological and geochemical mapping.

4.1.1 Rock types

The most dominant rock type identified in the 200-m model is the Äspö diorite, see section 2.3. Some subordinate rock types are also identified. The distribution as presented in the aforementioned section is based on general geological mapping on cores.

However detailed geological and geochemical mapping show that the term "Äspö diorite" is a general term that might indicate other subordinate rock types that can not be identified by eyes. The detailed characterization of rock types is important further on for the study of spatial variability of the different mechanical and thermal properties.

In the following detailed geological mapping results on boreholes KA2599G01 and KF0093A01 are presented. These results are of importance later on for the determination of properties of the rock mass.

Detailed core mapping of KA2599G01 revealed that the term "Äspö Diorite" involved a range of various rock types identified as Ävrö Granite, mingled Ävrö Granite/Äspö Diorite, and altered Ävrö Granite (Sundberg, 2002a).

The rock types identified in boreholes KA2599G01 (Sundberg, 2002a) and KF0093A01 (Janson and Stigsson, 2002) and theirs share in the hole sections are summarized in Table 4-2 and Table 4-3.

Table 4-2. Rock types in borehole KA2599G01, between length 56 to 128.3 m and detailed core mapped (Sundberg, 2002a)

Core length, m	Rock type	Share of the total length
37	Äspö Diorite	51 %
21.5	Ävrö Granite	30 %
7.4	Fine grained Granite	10 %
1.5	Meta-basite	2 %
4.9	Mingled Granite/Diorite	7 %

Table 4-3. Rock types in borehole KF0093A01, between length 2.4 to 36 m and ordinary mapped (Janson & Stigsson, 2002)

Core length, m	Rock type	Share of the total length
26.9	Äspö Diorite	80 %
1.3	Fine grained Granite	4 %
5.4	Diorite with a schistose structure	16 %

4.1.2 Fractures and fracture zones

The hydro-structural model developed in section 2 focused mostly of the analysis of natural fractures, and did only consider fracture data from tunnels and boreholes. As the mechanical properties of the rock mass are subjected to the fracture network stochastic data on fracture length, orientation and set density were required.

The statistical fracture network in the area can be derived from the input parameters for the Discrete Fracture Network determined from fracture data in the Zedex tunnel (Hermanson *et al.*, 1998; Staub *et al.*, 2002). Input parameters for the DFN on the prototype area were judged unsuitable as the analysis of fracture data was aimed to study hydraulic fractures. The localization of the Zedex tunnel is illustrated in Figure 1-1.

Three fracture sets have been identified and their characteristics are summarized in Table 4-4.

Table 4-4. Input parameters for the DFN model from the Zedex tunnel

Parameter	Value	Comments
Set 1		
Orientation (Mean pole trend and plunge, dispersion)	348.2, 4.2, K= 8.69 Fisher model	
Intensity (P32, m2/m3)		
Small fractures	0.4	*Small frac: traces shorter than 2 m*
Large fractures	0.23	*large frac: traces longer than 2 m*
Size, radius (m)		
Small fractures	R=0.25, std dev= 0.25	*Normal distribution*
Large fractures	R=4, std dev= 2	
Set 2		
Orientation (Mean pole trend and plunge, dispersion)	46.4,7.4, K= 10.5 Fisher model	
Intensity (P32, m2/m3)		
Small fractures	0.87	*Small frac: traces shorter than 2 m*
Large fractures	0.7	*large frac: traces longer than 2 m*
Size, radius (m)		
Small fractures	R=0.5, std dev= 0.25	*Normal distribution*
Large fractures	R=5, std dev= 1	
Set 3		
Orientation (Mean pole trend and plunge, dispersion)	142.8, 63.7, K= 8.99 Fisher model	
Intensity (P32, m2/m3)		
Small fractures	0.44	*Small frac: traces shorter than 2 m*
Large fractures	0.11	*large frac: traces longer than 2 m*
Size, radius (m)		
Small fractures	R=0.25, std dev= 0.25	*Normal distribution*
Large fractures	R=4, std dev= 2	

The reliability of the application of the DFN parameters for the experiment volume can be established by looking at local fracture data in the 200-m model. Figure 2-8 shows contours of poles of more than 450 fractures observed in tunnels around the tested area and Figure 2-3 shows contours of poles to 1300 fractures observed in boreholes in the 200-m model.

Figure 4-1 illustrates plots of poles to fracture planes mapped in the Zedex tunnel. The same sets of fractures as enhanced in Figure 2-3 and Figure 2-8 are identified, but the intensity of each set is not in agreement between the DFN model and the 200-m model. The dominant set in the Zedex tunnel is the sub-vertical striking NNW while the dominant set in the 200-m model is the sub-horizontal set.

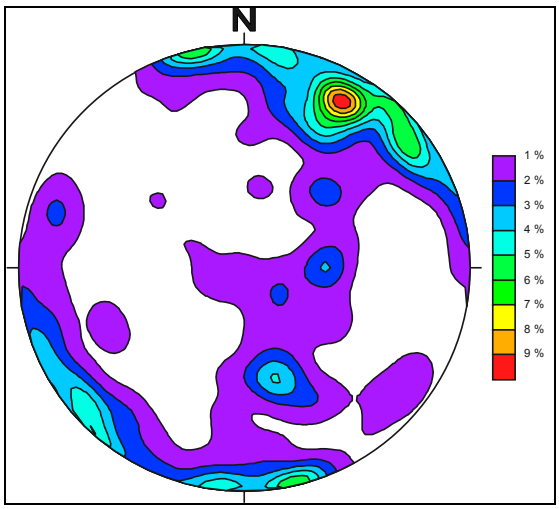

Figure 4-1. *Poles of SPRI data set (Zedex tunnel) fracture planes on a lower hemisphere, equal area projection. Terzaghi correction have been applied (Hermanson et al., 1998)*

4.2 Mechanical and thermal properties from previous investigations

4.2.1 Mechanical properties

The mechanical properties are evaluated for the intact rock, the rock mass, and the fractures. Only parameters required for modeling of the experiment are tackled in this report. The properties for the intact rock and rock mass are described by the following parameters:

- Young's modulus, E (GPa)
- Poisson's ratio, ν (–)
- Cohesion, c (MPa)
- Friction angle, ϕ (°)
- Tensile strength, σ_t (MPa)
- Uniaxial compression strength, σ_c (MPa)

The required properties for the fractures are:

- Normal stiffness, K_N (MPa/m)
- Shear stiffness, K_S (MPa/m)
- Residual angle of friction, ϕ_r (°)
- Aperture, a (mm)
- Fracture toughness, K_{IC} (MPa/m)

Mechanical properties of the intact rock

Mechanical properties of the intact rock have already been determined prior to this experiment in the Äspö HRL and in the experiment volume 1. No data are provided from experiment volumes 2 or 3. Preliminary data estimated for experiment volume 1 will then be applied to both areas.

Within the volume of the pillar stability experiment 1 (Figure 3-3) the Young's modulus and Poisson's ratio were determined on cores from boreholes KA2599G01 and KF0093A01 (Janson and Stigsson, 2002). The investigations were performed both in laboratory and in the field. The laboratory investigations are uniaxial compression test and diametrical measurements of the P-wave velocity on cores. The results from the laboratory investigations are summarized in Table 4-5.

Table 4-5. Determination of Young's modulus and Poisson's ratio, laboratory investigations on cores from boreholes KA2599G01 and KF0093A01

Deep and hole	Method	Rock type	Young's modulus, GPa	Poisson's ratio
-455 m, KA2599G01	Uniaxial	Diorite	70 ± 5	0.24 ± 0.04
-450 m, KA2599G01	P-wave	Diorite	78 ± 4	-
-470 m, KA2599G01	P-wave	Diorite	69 ± 7	-
-455 m, KF0093A01	Uniaxial	Diorite	60 ± 5	0.24 ± 0.04
-455 m, KF0093A01	P-wave	Fine Grained Granite	61 ± 7	-
-455 m, KF0093A01	P-wave	Diorite	65 ± 12	-

The results present a high dispersion for cores collected in the same borehole, but also high discrepancy between the two nearby orthogonal boreholes. The degree of inhomogeneity is locally in KA2599G01 about 5 % and in the horizontal hole between 15 and 20 %. The scattering of data between the two holes can be explained by small differences in geology, and especially the development of a schistose structure in the end of the horizontal hole. A conclusion from the laboratory investigations is that the local heterogeneity in the rock mass may be the main cause of the scattering in Young's modulus.

The field investigations were done in connection to *in-situ* stress measurements and are biaxial pressure test on the overcoring cores. The field investigations give scattered results in a wide range of magnitudes, and the results are not presented in this report. The discrepancy of results might be related to micro cracks that develop during the overcoring process, and to the scaling between the gauge length and the intact rock grain size. Despite wide range of values, the mean value of all scattered results is about the same as the mean value obtained for each sample from laboratory investigations (Table 4-5).

Mechanical properties determined in the experiment volume 1 can be compared to data obtained in the surrounding rock volume of the Äspö HRL. Laboratory investigations have been previously conducted on intact rock cores from boreholes KAS02, KA3545G and KA3557G by Stille and Olsson (1989), and Nordlund *et al.* (1999).

In order to determine the mechanical properties required for the intact rock, which are listed in the introduction of section 4.2.1, two mechanical tests were conducted: uniaxial compression tests (Stille and Olsson, 1989) and triaxial compression tests (Nordlund *et al.*, 1999). True cohesion and friction angle could only be determined from triaxial compression tests. The cohesion obtained from uniaxial compression test has been back-calculated on the assumption basis of a friction angle of 45°. The results of these investigations are analyzed and compiled by Staub *et al.* (2002), and the estimated mechanical properties for each rock type are summarized in Table 4-6. Raw data from the laboratory investigations (Nordlund *et al.*, 1999) are presented in Appendix C.

Table 4-6. Determination of Young's modulus, Poisson's ratio, cohesion and friction angle on intact rock in Äspö HRL (Staub *et al.*, 2002)

Hole	*Method*	Rock type	Young's modulus, GPa	Poisson's ratio	Cohesion, MPa	Friction angle, ^{o}
KAS02	*Uniaxial*	Greenstone	52.5 ± 17	0.22	23.8	45
KA3545G/ KA3557G	*Triaxial*	Diorite	73 ± 3	0.27	31	49[(1)]
KAS02	*Uniaxial*	Granite	62 ± 1	0.24	37.7	45
KAS02	*Uniaxial*	Aplite	65 ± 4.3	0.22	47.2	45

[(1)] The cohesion and friction angle for the Diorite were determined to 49 MPa respective 44^{o} by Nordlund *et al.* (1999), but have been re-evaluated by Staub *et al.* (2002).

The Young's modulus and Poisson's ratio of granite and diorite samples were also determined from laboratory investigations by Olsson (1998) and Lanaro (2001). The samples tested by Olsson (1998) are taken in the access tunnel, Ch.1623, and the samples studied by Lanaro (2001) are from the prototype area. Localization of the sampling areas towards the experimental volumes 1, 2 and 3 is illustrated in Figure 1-1. For comparison to the aforementioned values (Table 4-6), the obtained Young's modulus is 59 ± 3 GPa for the granite (Olsson, 1998) and 67 GPa for the diorite (Lanaro, 2001). The Poisson's ratio is given to be 0.25 for both intact rock types.

Measurements for tensile strength of intact rocks were only available for the diorite (Nordlund *et al.*, 1999). Values for other rock types were determined on the basis of the ratio of the tensile strength to uniaxial compression strength of the diorite samples (Staub *et al.*, 2002). Measured and calculated values for the 4 rock types are presented in Table 4-7.

The uniaxial compression strength of intact rocks is measured and determined from laboratory investigations (Stille and Olsson, 1989, and Nordlund *et al.*, 1999), see Table 4-7.

Table 4-7. Tensile strength and uniaxial compression strength of intact rock

Rock type	*Tensile strength, MPa*	*Uniaxial compression strength, MPa*
Diorite	*14.8*	*214*
Aplite	*15*	*228*
Granite	*12.8*	*182*
Greenstone	*8*	*115*

Mechanical properties of the fractures

The properties required for fractures, and listed in section 4.2.1, have earlier been investigated by Stille and Olsson (1989), Olsson (1998) and Lanaro (2001), for fractures on cores in the Äspö HRL. The investigations by Stille and Olsson (1989) and Lanaro (2001) have afterwards been analyzed and re-evaluated (Staub *et al.*, 2002). The results from Olsson (1998) and Staub *et al.* (2002) are summarized in Table 4-8. Raw data from the laboratory investigations (Stille and Olsson, 1989, and Lanaro, 2001) are shown in Appendix D.

Table 4-8. Determination of normal stiffness, shear stiffness, residual friction angle and aperture (Olsson, 1998, Staub *et al.*, 2002)

Orientation/ references	Normal stiffness, MPa/m	Shear stiffness MPa/m	Residual angle ^{o}	Aperture mm
Sub-vertical/ Staub *et al.*, 2002	$61.5 .10^3$ (1)	$35.5 .10^3$ (1)	29.2 ± 3.6	0.56
Sub-vertical/ Olsson, 1998	$60.7 .10^3$ (2)	$3.1 .10^3$ (2)	31	0.25 ± 0.24
Sub-horizontal/ Staub *et al.*, 2002	$21.9 .10^3$ (1)	$15.7 .10^3$ (1)	29.2 ± 3.6	0.2

(1) with a normal stress of 23 MPa

(2) with a normal stress of 2-6 MPa

The magnitude of the apertures could also be compared with the investigations conducted by Hakami (1995). The target fracture was sub-vertical and in Granite, and the studied sample had an area of 80 cm^2. The measurement gave an aperture of $0.36 \pm$ 0,15 mm.

Fracture toughness of rock material is determined by three-point bending tests, and the procedure is described in Nordlund *et al.* (1999). Data in the experimental volume are available only for Diorite, and measurements have been done on core samples from boreholes KA3557G (4 samples) and KA3545G (1 sample). Only fracture toughness in mode I has been investigated. From test results presented in Nordlund *et al.* (1999), K_{IC} for the Diorite is 3.21 ± 0.14 MPa.

Mechanical properties of the rock mass

The determination of the mechanical properties of the rock mass has been achieved by numerical analysis (Staub *et al.*, 2002). A 2D numerical model was set up that simulate a plain strain loading test. The input data consider the fracture geometry, as well as mechanical properties of intact rock and fractures, as presented and evaluated in section 4.2.1. Statistical data on fractures were used as input to simulate a three-dimensional Discrete Fracture Network (DFN) in the FracMan software. The model used in this project is the DFN developed from the Zedex tunnel (as referred to in section 4.1.2). The numerical modeling was achieved by using the two-dimensional code UDEC, and the rock block models were generated from 2D trace sections extracted from the 3D DFN model. Simulations were run on "homogeneous" rock blocks (constituted on only one rock type) at different in-situ stress values in order to compute the influence of depth on the rock mass mechanical behavior. Simulations for each experiment set-up were conducted at two different stress levels in order to estimate the uniaxial compressive strength of the rock, according to Mohr-Coulomb criterion.

The mechanical properties obtained by simulations for the rock mass are summarized in Table 4-9. Values are impaired to the state of *in-situ* stresses. Values of the uniaxial compressive strength are valid in the interval [5.6 MPa – 22.4 MPa].

Table 4-9. Determination of Young's modulus, Poisson's ratio, cohesion, friction angle and uniaxial compression strength on rock mass in Äspö HRL (Staub *et al.*, 2002)

Rock type	Young's modulus, GPa[(1)]	Poisson's ratio [(1)]	Cohesion, MPa	Friction angle, °	Uniaxial compression strength, MPa
Greenstone	34.3 ± 9	0.24 ± 0.02	14.8 ± 3	38 ± 3	61.0 ± 13
Diorite	46.6 ± 4	0.26 ± 0.01	16.4 ± 3	41.4 ± 4	73.3 ± 16
Granite	40.3 ± 3	0.24 ± 0.02	22.5 ± 8	38.6 ± 5	97.5 ± 27.8
Aplite	41.1 ± 4.1	0.23 ± 0.02	22.3 ± 5.9	40.4 ± 5.5	95.0 ± 37.4

[(1)] The values of Young's modulus and Poisson's ratio are determined for a horizontal stress of 22.4 MPa

4.2.2 Thermal properties

The thermal properties are:

- Thermal conductivity, λ (W/m, K)
- Volume heat capacity, C (MJ/m^3, K)
- Coefficient of linear expansion, α (m/mK)
- Density, ρ (ton/m^3)
- Initial temperature in the rock mass, T_i (°C)

Thermal conductivity, volume heat capacity and density

The lower section of borehole KA2599G01 is located in the volume targeted for the experiment volume 1, see Figure 3-2. Eleven samples were selected from the drill core of borehole KA2599G01 (Sundberg, 2002a). Each sample was split into three sub-samples. Two of the sub-samples were used for thermal properties and density measurements. The other sample was used for chemical analyses. The thermal conductivity and volume heat capacity were evaluated from the thermal measurement (TPS-method) and the density was determined according to standards DIN 52102-RE VA. The results obtained at temperature of 25°C are summarized in Figure 4-2 and Table 4-10. Raw data from the investigations (Sundberg, 2002a) are shown in Appendix E.

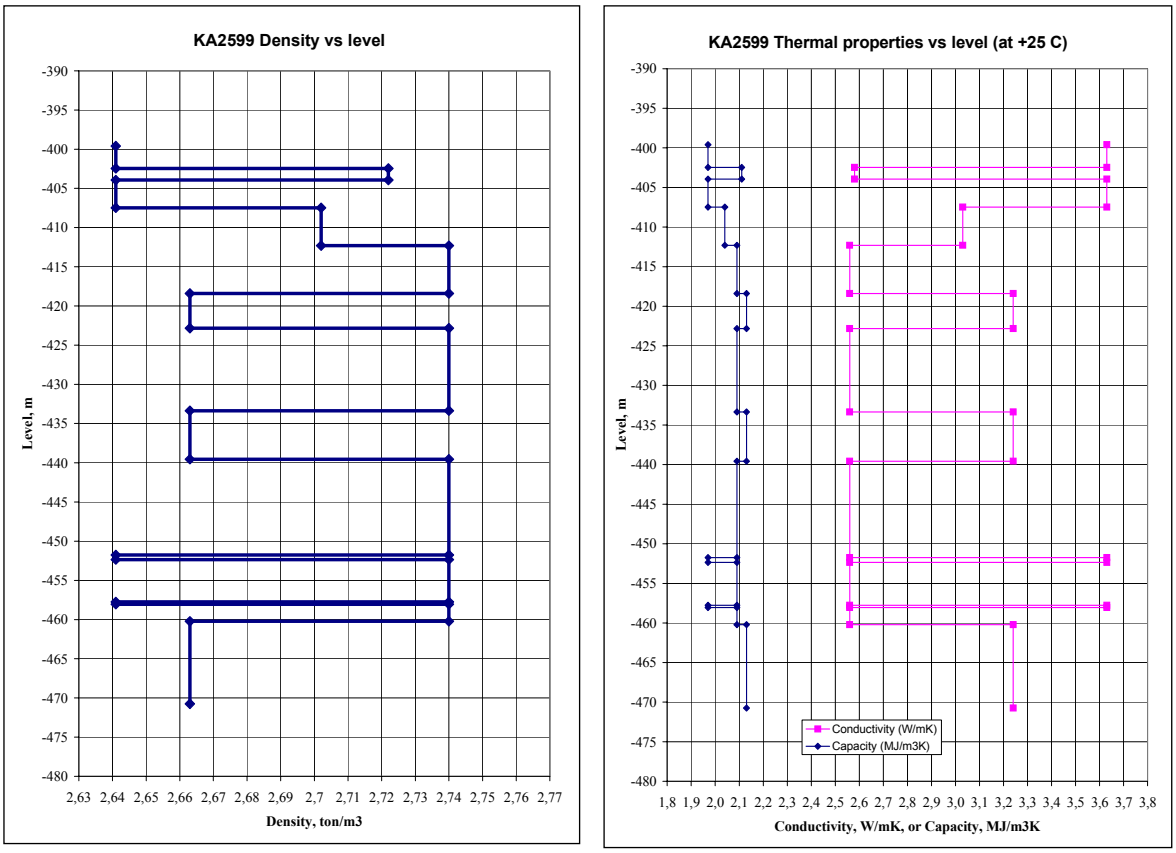

Figure 4-2. *Density and thermal properties vs depth in borehole KA2599G01. Results at temperature + 25°C, based on the rock type distribution and measured properties on samples (Sundberg, 2002a).*

Table 4-10. Observed rock types, measured density and thermal properties, in borehole KA2599G01 (Sundberg, 1991, and Sundberg, 2002a)

Rock type	Density, ton/m^3	Thermal properties, at temperature +25^{o}C	
		Conductivity, W/mK	Capacity, MJ/m^3,K
Äspö Diorite	2.740	2.56	2.09
Meta-basite[(1)]	2.722	2.58	2.13
Mingled Granite/Diorite[(2)]	2.702	2,90	2.11
Fine grained Granite	2.641	3.63	1.97
Ävrö Granite	2.663	3.24	2.13

(1) Thermal properties of meta-basite have been obtained from Sundberg, 1991.

(2) Thermal properties of mingled Äspö diorite/Ävrö granite have been approximated with mean values of the two rock types.

The results obtained in the experiment volume 1 could be compared to previous thermal properties investigated in the surrounding rock volume of the Äspö HRL (Sundberg, 1991 and Sundberg and Gabrielsson, 1999). The thermal conductivity and volume heat capacity determined from these investigations are in the same range as the results presented in Table 4-10. The slight discrepancy between the results could be explained by changes in mineral composition at different locations (Sundberg, 2002a). From the results obtained in borehole KA2599G01 a clear relationship is established between density and thermal properties, for the investigated rock types, see Figure 4-3.

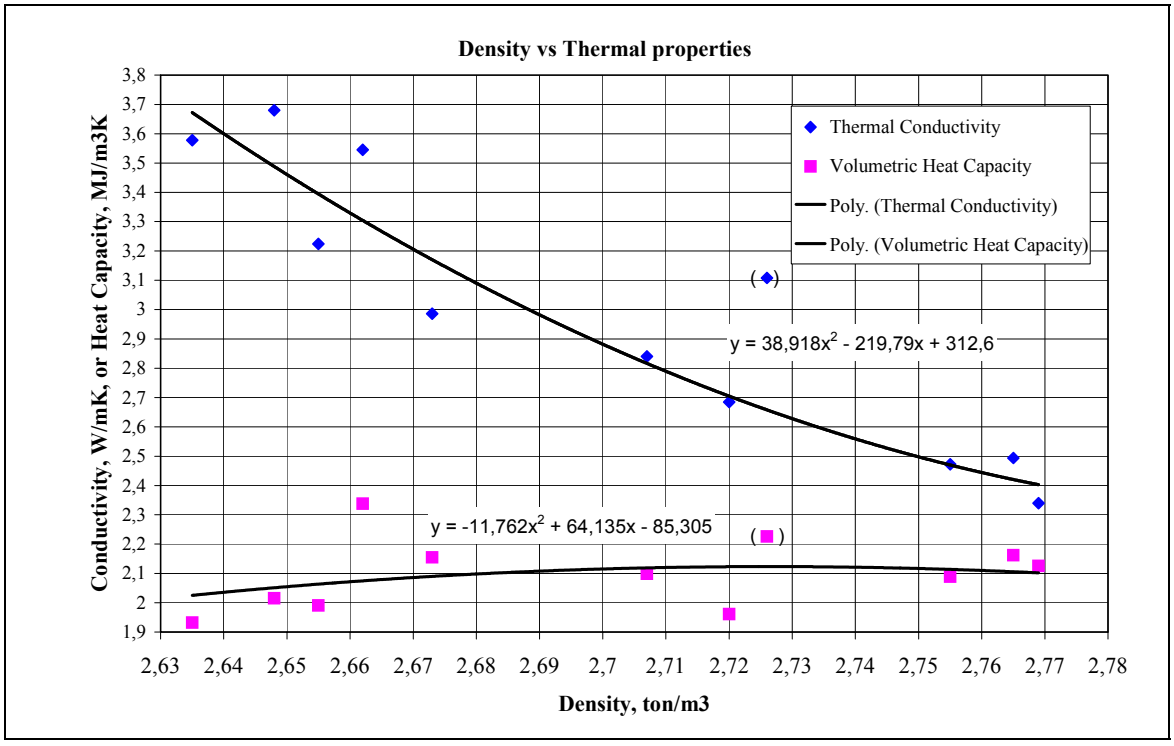

Figure 4-3. *The relation between density and thermal properties, measured at cores from borehole KA2599G01, at a temperature of 25˚C.*

These relationships provide useful indirect methods for a first predicting the thermal properties on cores when no thermal measurements have been performed:

1. If a density logging is done in the borehole, the relationship determined in Figure 4-3 can be used.

2. If only a core mapping on rock types is available, the relationship in Figure 4-3 can be used together with estimation of density in Table 4-10.

On the basis of these relationships thermal conductivity and thermaö heat capacity can be estimated from density logging in the drilled boreholes of the three location alternatives.

The variations of thermal properties with temperature have been investigated. Measurements at 25 and 80°C were conducted on dry samples of diorite and granite. The results are presented in Table 4-11. The results at 25°C cannot be compared to those presented in Table 4-10. Indeed those values represent the thermal conductivity and heat capacity of water-saturated samples, and not dry samples as in Table 4-11. Focus should be made on the relative changes in values at two different temperatures in Table 4-11.

Table 4-11. Thermal conductivity and heat capacity of dry samples at 25 and 80°C

Rock type	*Conductivity, W/mK*		*Heat Capacity, MJ/m^3,K*	
	+ 25 ^{o}C	*+ 80 ^{o}C*	*+ 25 ^{o}C*	*+ 80 ^{o}C*
Äspö Diorite	*2.419*	*2.395*	*2.012*	*2.367*
Ävrö Granite	*2.83*	*2.805*	*2.017*	*2.323*

Coefficient of linear expansion

11 core samples taken from borehole KA2599G01 were analyzed according to ISO 4897 and DIN 53752 (Sundberg, 2002b). The samples were collected from the same sections along the core as the samples used for the determination of thermal conductivity and capacity. The measurements were carried out mainly in three different temperature intervals: 5-50 °C, 50-105 °C and 5-95 °C. The investigations were done on cores of Äspö diorite, Ävrö granite, fine-grained granite and altered Äspö diorite. The mean values of coefficient of thermal expansion for all measurements at different temperature intervals are presented in Figure 4-4. Raw data from the investigations (Sundberg, 2002b) are shown in Appendix E.

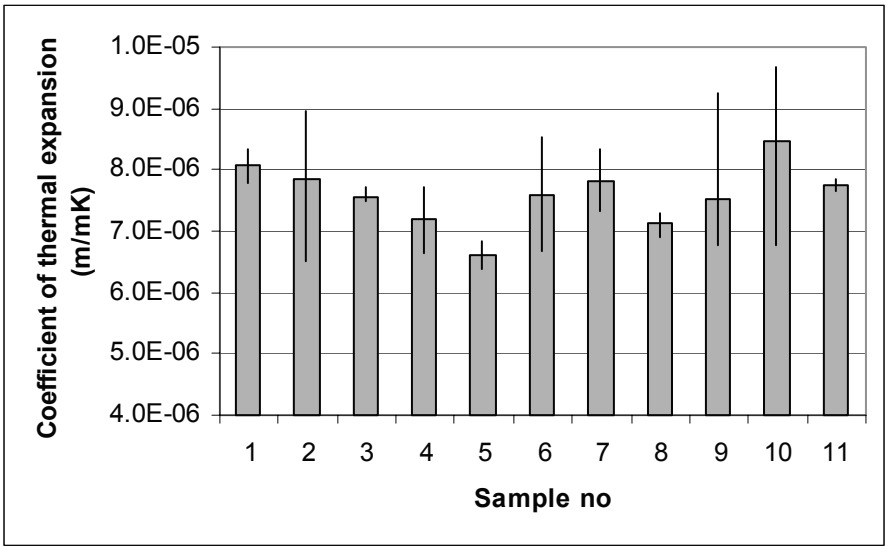

Figure 4-4. *Mean value of coefficient of thermal expansion for all measurements at different intervals of temperature. Highest and lowest values are also shown (Sundberg, 2002b)*

On the basis of the core mapping and of the previous mean values the coefficient of thermal expansion can be calculated for each rock type. The results are presented in Table 4-12. No significant difference between the different rock types can be observed. There is a large dispersion in the results within each rock type.

Table 4-12. Mean value of coefficient of thermal expansion for different rock types

Rock type	***Coefficient of thermal expansion (m/mK)***		***Sample ID****, see* Figure 4-4
	Mean value	***Standard deviation***	
Äspö Diorite	*7.89E-06*	*0.545E-06*	*1, 2, 3, 7 and 8*
Altered Äspö Diorite	*7.25E-06*	-	*9*
Ävrö Granite	*8.0E-06*	*0.889E-06*	*4, 10 and 11*
Fine-grained Granite	*7.11E-06*	*0.841E-06*	*5 and 6*

The correlation between density and coefficient of thermal expansion is not so obvious.

The data obtained by Sundberg (2002b) can be compared to results from laboratory investigations done in the surrounding rock volume on cores from the Prototype tunnel (Larsson *et al.*, 2002). The investigations were done on cores of diorite and granite and the cores were placed in a container filled with water. The strain was measured using electric strain gauge glued to the cores and during temperature cycling between 20^{o} C and 70^{o} C.

The coefficient has been measured to $(4.5 \pm 0.5)\ 10^{-6}$ /K for both rock types (Larsson *et al.*, 2002). The reliability of these results could be questioned as the measurement procedure implies some uncertainties, like the reaction of glue in water at different temperatures. Hence, data obtained for the coefficient of linear expansion for both granite and diorite were looked up in the literature. In the Swedish technical books, TEFYMA and Bygg, the coefficient given is 8.3E-06 /K for granite and 10E-06 /K for the diorite.

Within the so-called Decovalex project values ranging from 9.0E-06 /K to 10.0E-06 /K have been used in different analysis (Börgesson and Hernelind, 1995, and Hudson and Stephansson, 1995). In Larsson *et al.* (2002) two reference investigations provide two distinct intervals for this coefficient measured on Granite that are: 7.7 – 11.2E-06 /K and 3.4 – 6.6E-06/K.

No data were found for the coefficient of linear expansion of meta-basite.

The values provided by Sundberg (2002b) are slightly lower for both Diorite and Granite than the one found in the literature, but higher than the one presented in Larsson *et al.*, 2002. It is then recommended to use the mean values determined by Sundberg (2002b) for the modeling of the experiment.

Initial temperature

The initial temperature in the rock mass has been measured in KA2599G01 at level – 400 m (Sundberg, 2002a). The temperature was continuously measured during one week and the hole was closed at the top. The obtained temperature was 13.2 ^{o}C.

4.3 Preliminary mechanical and thermal properties

The preliminary mechanical and thermal properties are determined from the analysis of the results of previous investigations that have been presented in section 4.2. A precession has been applied to properties determined in the experiment volumes, when the reliability of the results was not questionable. Previous boreholes and data are located in the surrounding of experiment volume 1, see Figure 3-2 and Figure 3-3. Nevertheless as discussed in section 4.1 the geological model is expected to be similar in both experiment volumes, as well as the in situ state of stress (see section 3). Hence mechanical and thermal properties are expected to be similar for each rock type in the three experiment volumes.

The present properties are used in the first stages of 2D modeling of the experiment, and will be adjusted as further detailed investigations are performed in connection to the drilling in the experiment volumes.

The preliminary mechanical properties for intact rock and the rock mass are summarized respectively in Table 4-13 and Table 4-14, preliminary mechanical properties for fractures in Table 4-15, and preliminary thermal properties in Table 4-16.

It should be noted that the mechanical properties for the rock mass are subjected to the fracture network used for the simulations and to the state of stress (Staub *et al.*, 2002). The results might be affected by modifications of fracture geometry in the area. Nevertheless, preliminary assumptions are made in the early stages of the modeling that the fracture geometry in the experiment volumes is similar to the one analyzed from mapping in the Zedex tunnel, see section 4.1.2, which has also been used in the 2D simulations conducted by Staub *et al.* (2002).

Table 4-13. Determination of the preliminary mechanical intact rock properties, in the volume of the pillar stability experiment

Rock type	Young's modulus, GPa	Poisson's ratio	Cohesion, MPa	Friction angle, °	Tensile strength, MPa
Greenstone	53 ± 17	0,22	23.8	45	8
Diorite	68 ± 8	0,24	31	49	14.8
Granite	61 ± 7	0,24	37.7	45	12.8
Aplite	65 ± 4.3	0.22	47.2	45	15

Table 4-14. Determination of the preliminary mechanical properties of the rock mass, in the volume of pillar stability experiment

Rock type	Young's modulus, GPa(1)	Poisson's ratio(1)	Cohesion, MPa	Friction angle, °	Uniaxial compression strength, MPa
Greenstone	34 ± 9	0.24	14.8	38	61 ± 13
Diorite	47 ± 4	0.26	16.4	41	73.3 ± 16
Granite	40 ± 3	0.24	22.5	39	97.5 ± 27.8
Aplite	41 ± 3	0.31	22.3	40.4	95 ± 37.4

(1) The values of Young's modulus and Poisson's ratio are determined for an horizontal stress of 22.4 MPa.

Table 4-15. Determination of the preliminary mechanical properties of fractures, in the volume of pillar stability experiment

Orientation	Normal stiffness, MPa/m	Shear stiffness, MPa/m	Residual angle, °	Aperture, mm
Sub-vertical	$61.5.10^3$	$35.5 .10^3$	31	0.4 ± 0.2
Sub-horizontal	$21.9 .10^3$	$15.7 .10^3$	30	0.2 ± 0.1

Table 4-16. Determination of the preliminary thermal properties of intact rock, in the volume of pillar stability experiment

Rock type	Density ton/m^3	Thermal conductivity W/m, K	Volume heat capacity, MJ/m^3, K	Coefficient of linear expansion, 1/K
Äspö Diorite(1)	2.71	2.83	2.10	(7.9 ± 0.5) E-06
Green-stone	2.77	2.58	2.13	-
Aplite	2.64	3.63	1.97	(7.1 ± 0.8) E-06

(1) The term "Äspö Diorite" is generally used in "normal mapping", but involves different rock types, see section 4.1. The values are a mean value for all rock types defined under the general term.

The initial temperature in the rock mass is 13.2 °C.

5 Complementary information from boreholes KA3376B01, KA3386A01, KF0066A01 and KF0069A01

This section presents the analysis of mapping data from the four new core boreholes. The boreholes are named KF0066A01, KF0069A01, KA3376B01 and KA3386A01, and their localization towards the tunnel system is illustrated in Figure 5-1. Boreholes KF0066A01 and KF0069A01 are located in experiment volume 1, borehole KA3386A01 is located in experimental volume 2 and borehole KA3376B01 is located in experimental volume 3, see Figure 1-1 and Figure 3-3.

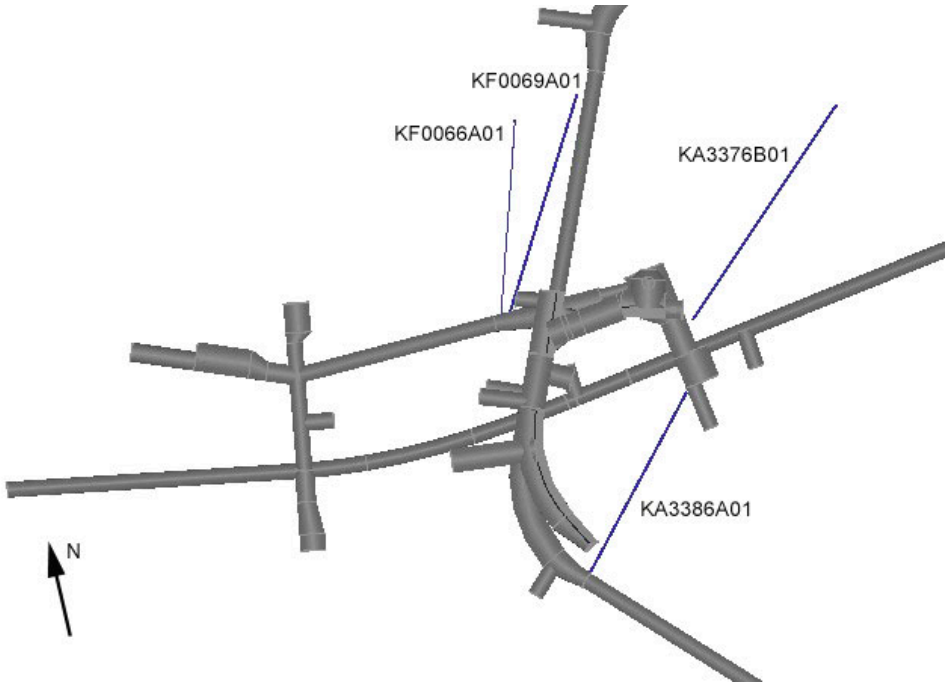

Figure 5-1. *Localization of the new drilled boreholes*

The data mapped and available in each borehole are listed in Table 5-1. The detailed analysis of the borehole data in consideration to the hydro-structural model developed in a 200-m cube (section 2) and including the three experiment volumes will be a support for decision of the localization of the experiment.

Table 5-1. Information available for the boreholes KF0066A01, KF0069A01, KA3376B01 and KA3386A01

Borehole	Borehole length, m	Information
KF0066A01	60.11	Lithology, fractures, density-logging, flow-logging
KF0069A01	70.09	Lithology, fractures, density-logging, flow-logging,
KA3376B01	79.80	Lithology, fractures, density-logging, flow-logging, stress measurements
KA3386A01	65.11	Lithology, fractures, density-logging, flow-logging,

Lithology, fractures and density logging are summarized in the following sections, the original flow logging are shown in Appendix F, and the results of the stress measurements for borehole KA3376B01 are summarized in Sjöberg (2002).

The thermal properties could be estimated on the results from the density logging on the basis of the relationships between density and thermal properties established on earlier results in the Äspö HRL, see section 4. The estimated thermal properties are presented in section 5.3.

5.1 Rock types and fracture frequency

The information of rock types and fractures are based on the ordinary core mapping at site, with BIPS logging.

The rock types identified are diorite, fine grained granite (or aplite), and hybrid rock. The distribution of rock types along the boreholes is illustrated in Figure 5-2.

The denomination for diorite is the same as described in section 4, section 2.1. Rocks mapped as diorite can vary in chemical composition and alteration degree. The term hybrid rock is used to define a mixture of Äspö diorite and greenstone in such a way that the parent rock cannot be distinguished. At this stage the rock type identification is based on "general" mapping, which implies that no differentiation is made on the different rocks in the "diorite" group.

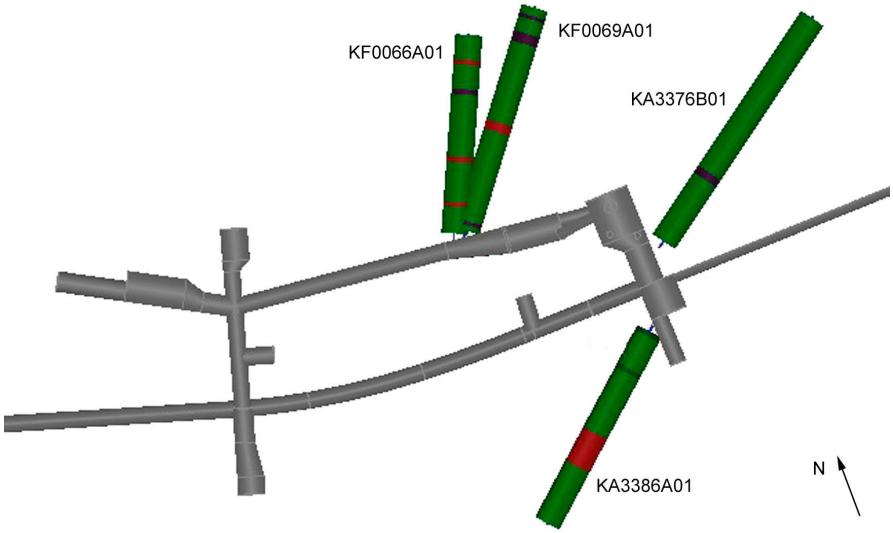

Figure 5-2. *Rock type distribution along the new boreholes (green: diorite; red: aplite; violet: hybrid rock)*

The rock type distribution has been studied in each borehole, and the fracture frequency of natural fractures has been calculated for each rock type in each borehole. The results are presented in Table 5-2 to Table 5-5 for the respective boreholes.

Table 5-2. Rock types and fracture frequency in borehole KF0066A01

Rock type	Core length, m	Share of the total length, %	Fracture frequency, /m
Diorite	52.0	90	1.2
Fine Granite	4.2	7	3.1
Hybrid rock	1.4	3	3.6
All	-	-	1.38

Table 5-3. Rock types and fracture frequency in borehole KF0069A01

Rock type	Core length, m	Share of the total length, %	Fracture frequency, /m
Diorite	59.6	88	0.6
Fine Granite	2.7	4	2.2
Hybrid rock	5.1	8	1.2
All	-	-	0.66

Table 5-4. Rock types and fracture frequency in borehole KA3376B01

Rock type	Core length, m	Share of the total length, %	Fracture frequency, /m
Diorite	74.1	96	1.9
Fine Granite	1.1	1	-
Hybrid rock	2.3	3	1.3
All	-	-	1.92

Table 5-5. Rock types and fracture frequency in borehole KA3386A01

Rock type	Core length, m	Share of the total length, %	Fracture frequency, /m
Diorite	48.9	80	1.4
Fine Granite	10.9	18	4.3
Hybrid rock	1.5	2	4.7
All	-	-	1.95

The rock type distribution and fracture frequency observed in KA3386A01 (alternative 2) are significantly different from the one mapped in both KF0066A01 and KF0069A01 (alternative 1) and KA3376B01 (alternative 3). The proportion of diorite is much less in KA3386A01 than in the three other boreholes. This is mainly explained by the occurrence of a large slab of fine grained granite (between section 35.5 and 46.4 m) in KA3386A01, whereas only narrow veins occur in KF0066A01, KF0069A01 and KA3376B01.

Nevertheless the analysis of tunnel and core mapping in the Äspö HRL indicates that fine grained granite mostly appear in narrow veins. It seems then unlikely that the geometry and occurrence of aplite when drilling the tunnel will be different in KA3386A01 than in the three other boreholes in the experiment volumes. The most probable explanation is that the borehole KA3386A01 went through a slab along the major axis, which is supported by the fact that the borehole is almost parallel to the orientation of some aplite slabs mapped in the TBM tunnel, see Rhén (1995).

When looking at the core-log it can be observed that the higher fracture frequency in KA3386A01 can be explained by the high fracturing degree of the aplite. The higher fracturing frequency in KA3376B01 can be explained by the fact that the borehole is located near the edge of the block H, see section 3.

5.2 Density logging

Density logging has been done in each borehole by Raycon AB. The density is measured in a 30-cm interval designed between the emitter and the receiver. The monitoring device is moved down the hole by 10-cm steps.

The raw values at every measurement points are plotted in Figure 5-3 to Figure 5-6 (curves with markers). The average density value in 6-m blocks has been calculated down the hole by moving the calculation interval 10 cm down. The results are presented in Figure 5-3 to Figure 5-6.

In the first stage of the experiment, the density measurements are used to evaluate thermal properties along the borehole, by using the relationships between density and thermal conductivity / thermal capacity that have been established in section 4.2.2. These relationships are based on data from earlier laboratory measurements in KA2599G01 at the Äspö HRL (Sundberg, 2002). The range of density values obtained in this preliminary study is $2.63.10^3$ kg/m^3 to $2.78.10^3$ kg/m^3. The relationships are therefore valid in this interval of density value, but it would be "hazardous" to extrapolate them outside of the intervals. The values from density logging of the 4 cored boreholes were cut off at $2.63.10^3$ kg/m^3 (minimal value) and $2.78.10^3$ kg/m^3 (maximal value).

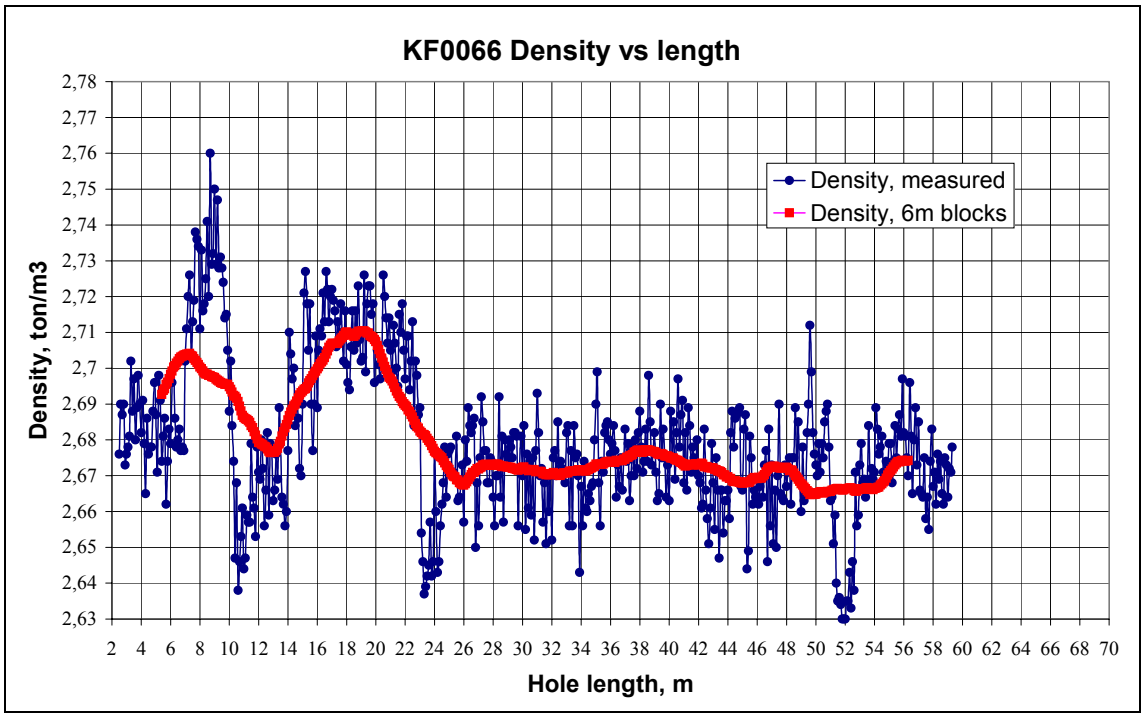

Figure 5-3. *Density logging along borehole KF0066A01, every measured points and the average values in six meters block along the borehole.*

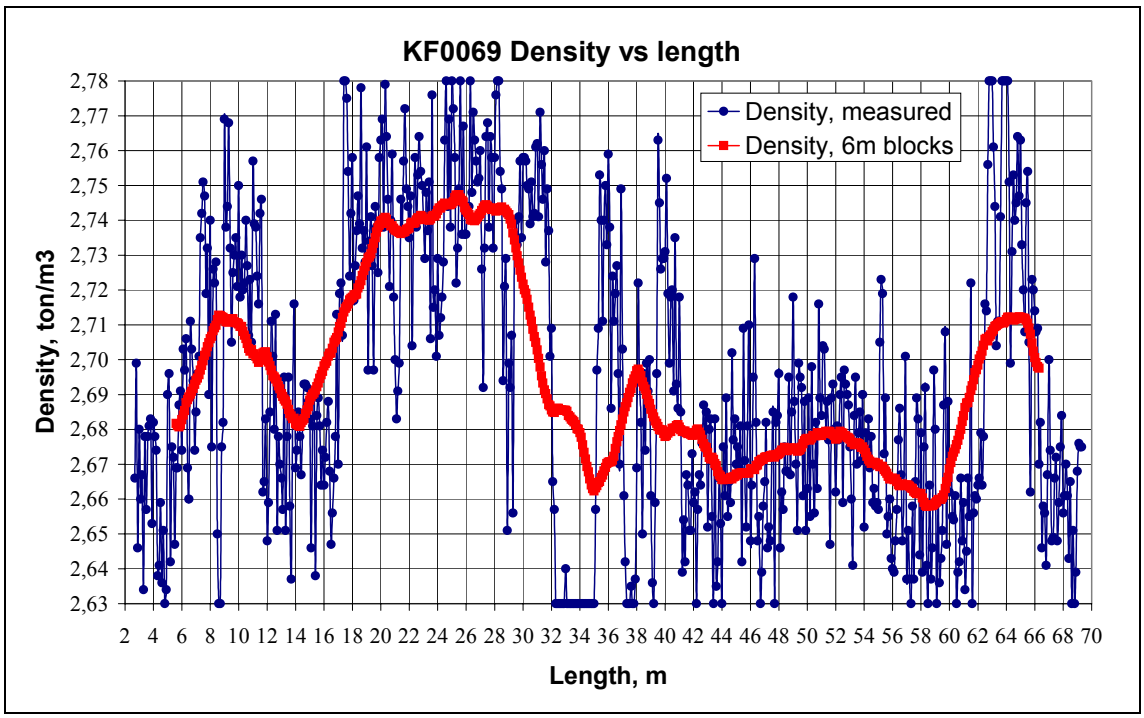

Figure 5-4. *Density logging along borehole KF0069A01, every measured points and the average values in six meters block along the borehole.*

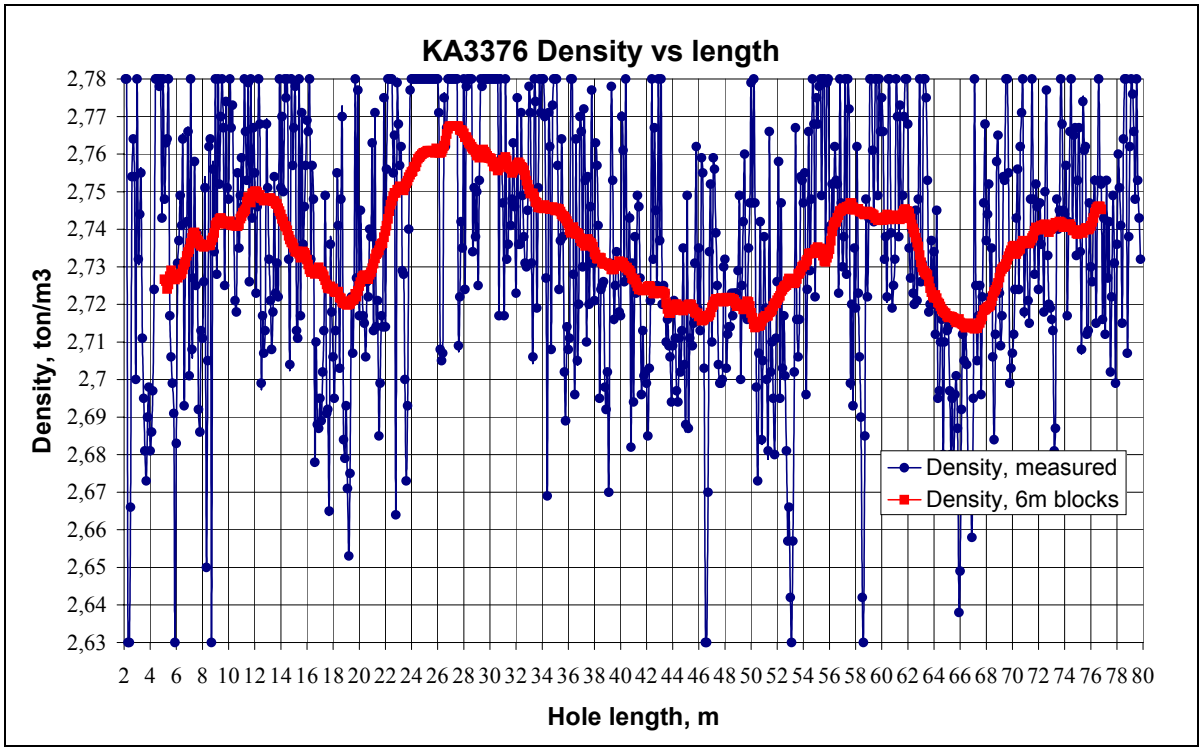

Figure 5-5. *Density logging along borehole KA3376B01, every measured points and the average values in six meters block along the borehole*

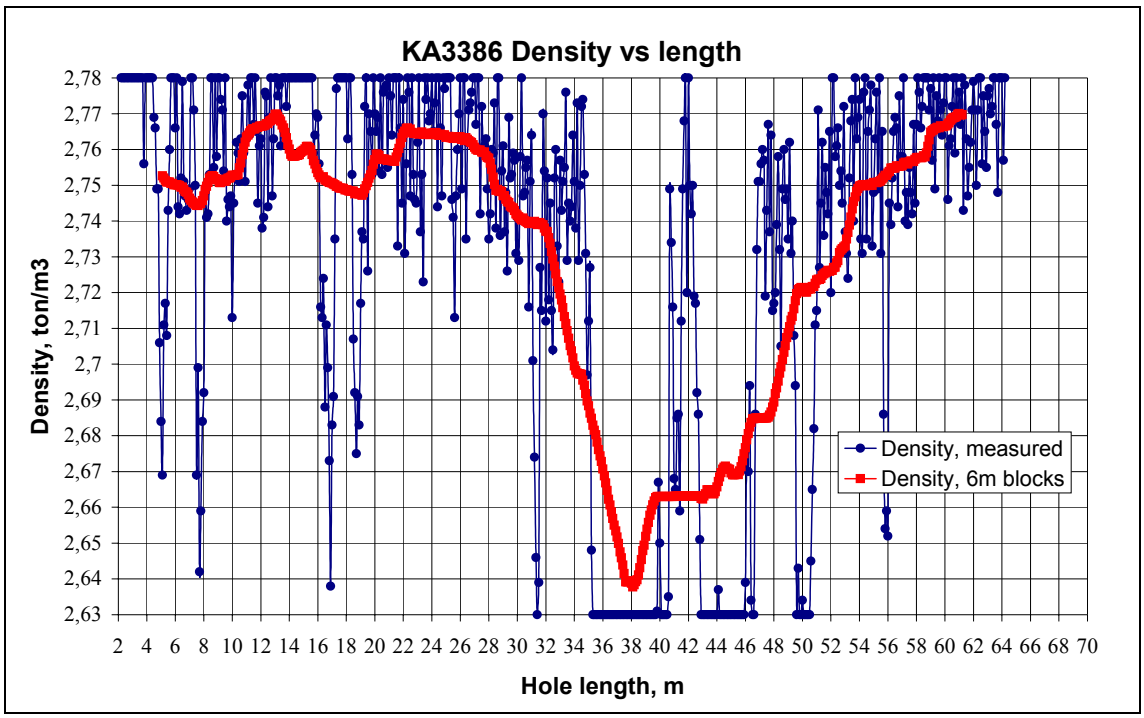

Figure 5-6. *Density logging along borehole KA3386A01, every measured points and the average values in six meters block along the borehole*

There is a clear difference between the results of the density logging for the three experimental volumes. The density values in experiment volume 1, illustrated by data from boreholes KF0066A01 and KF0069A01, are generally lower than density values in volumes 2 and 3. The observed scattering of the results is highest in volume 2 (borehole KA3386A01). As it can directly been observed on the curves in Figure 5-6, the density values are in general higher and the amount of cut-off values quite significant. The high frequency of measured values that are outside of the interval might be related to errors in the calibration of the equipment, or to differences in the diorite (chemical composition, alteration degree).

The density logging of borehole KA3386A01 shows high variation in density values, see Figure 5-6. The decrease in density between lengths 35.5 to 46.4 m is correlated to the occurrence of fine grained.

The calculated mean value and standard deviation of the measured density for the boreholes are presented in Table 5-6. The calculation of the statistic terms over 6 m tends to smooth the variation of the raw density data.

Table 5-6. The mean value and standard deviation of the density.

Borehole	Density, 10^3 kg/m^3, raw data		Density, 10^3 kg/m^3, 6-m blocks	
	Mean value	Standard deviation	Mean value	Standard deviation
KF0066A01	2.679	0.021	2.680	0.013
KF0069A01	2.692	0.048	2.695	0.026
KA3376B01	2.742	0.05	2.736	0.013
KA3386A01, including the granite section	2.734	0.076	2.729	0.039
KA3386A01, excluding the granite section	2.759	0.053	2.745	0.021

5.3 Predictions of thermal properties

The predicted thermal properties, conductivity (λ) and heat capacity (C), have been calculated from the following relationships, which are based on results analyzed and presented in section 4.2.2:

$$\lambda = 38.918 \cdot \rho^2 - 219.79 \cdot \rho + 312.6 \quad (4.1)$$

$$C = -11.762 \cdot \rho^2 + 64.135 \cdot \rho - 85.305 \quad (4.2)$$

where ρ is the density.

It must here be pointed out that the above relationships are based on only ten measured samples in one borehole, called KA2599G01 (Sundberg, 2002). The thermal properties predicted from the relationships must be verified and validated later on by laboratory measurement on samples from the three boreholes. Density measurements on the same samples are also required.

The thermal properties predicted from equations (4.1) and (4.2) are presented in Figure 5-7 to Figure 5-10. The results are based on the processed density logging, see section 5.2. As for the density the results are presented for each measured point along the borehole (cut-off values) and for the "smoothed" values calculated in 6-m blocks.

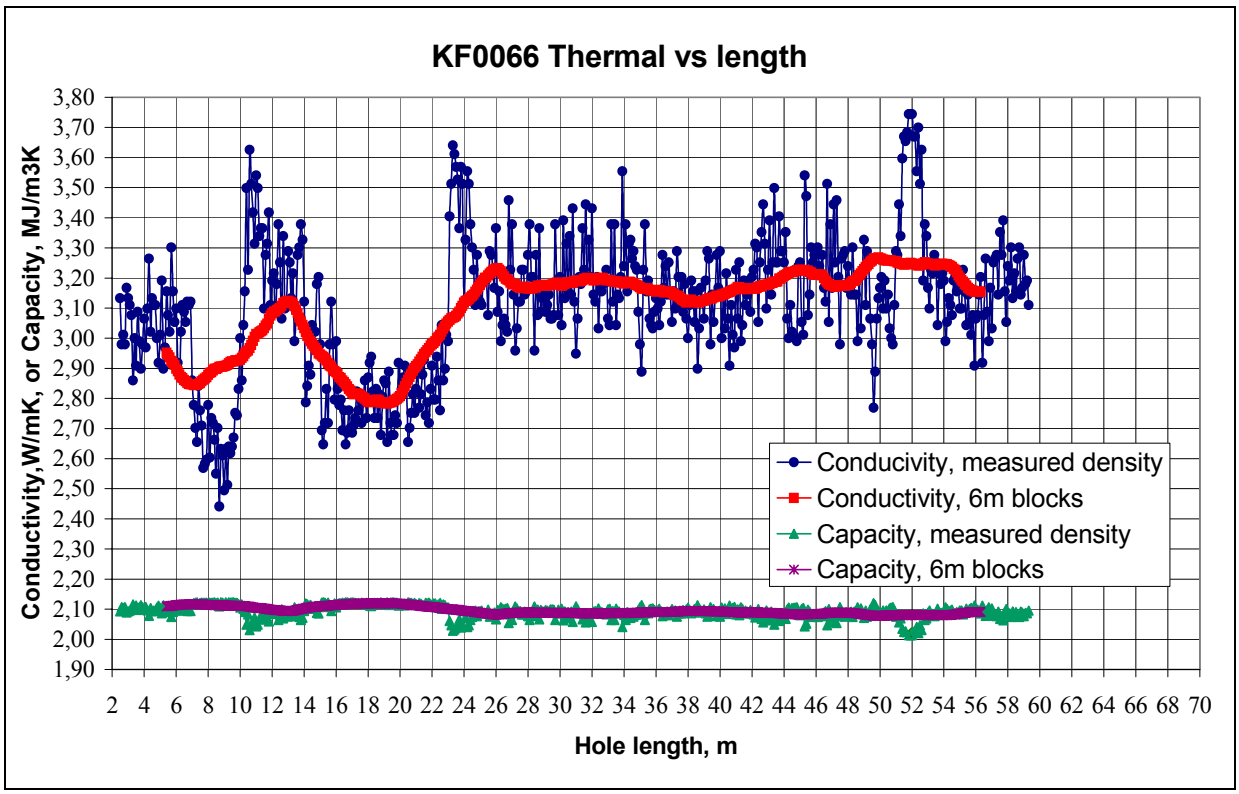

Figure 5-7. *Predicted thermal properties in borehole KF0066A01.*

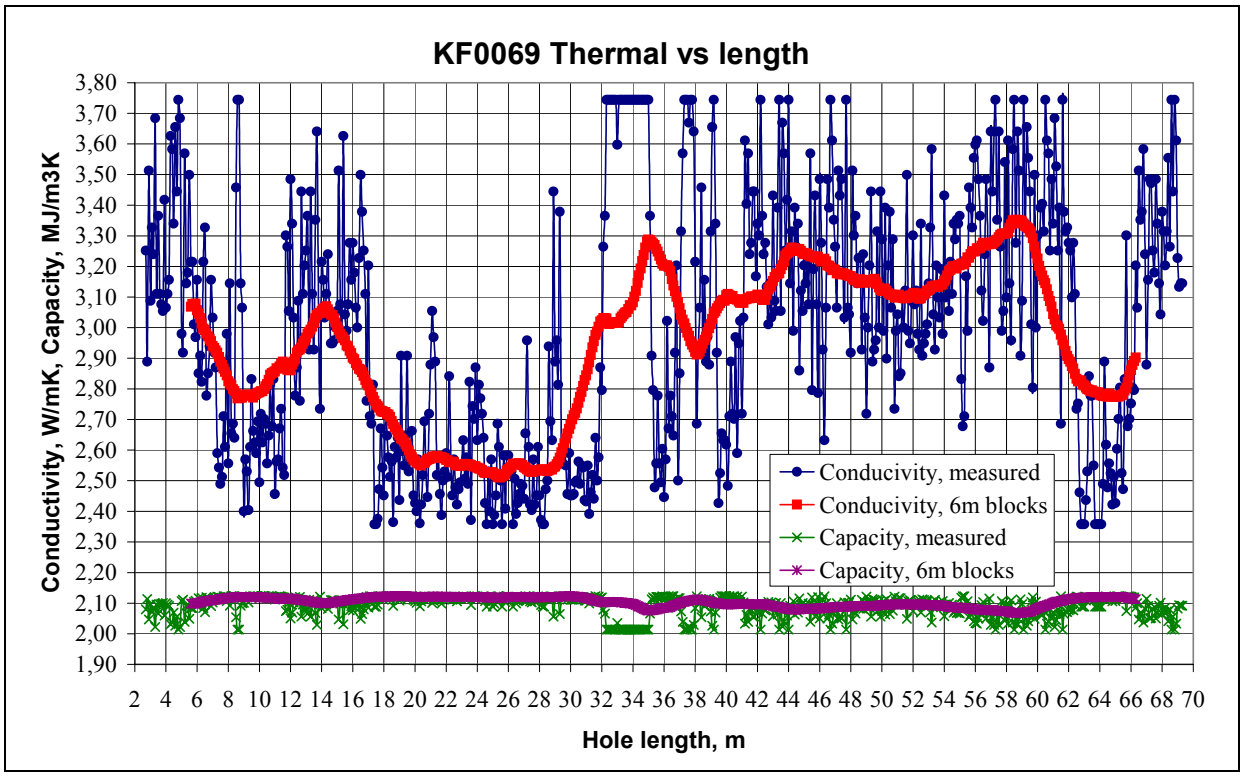

Figure 5-8. *Predicted thermal properties in borehole KF0069A01.*

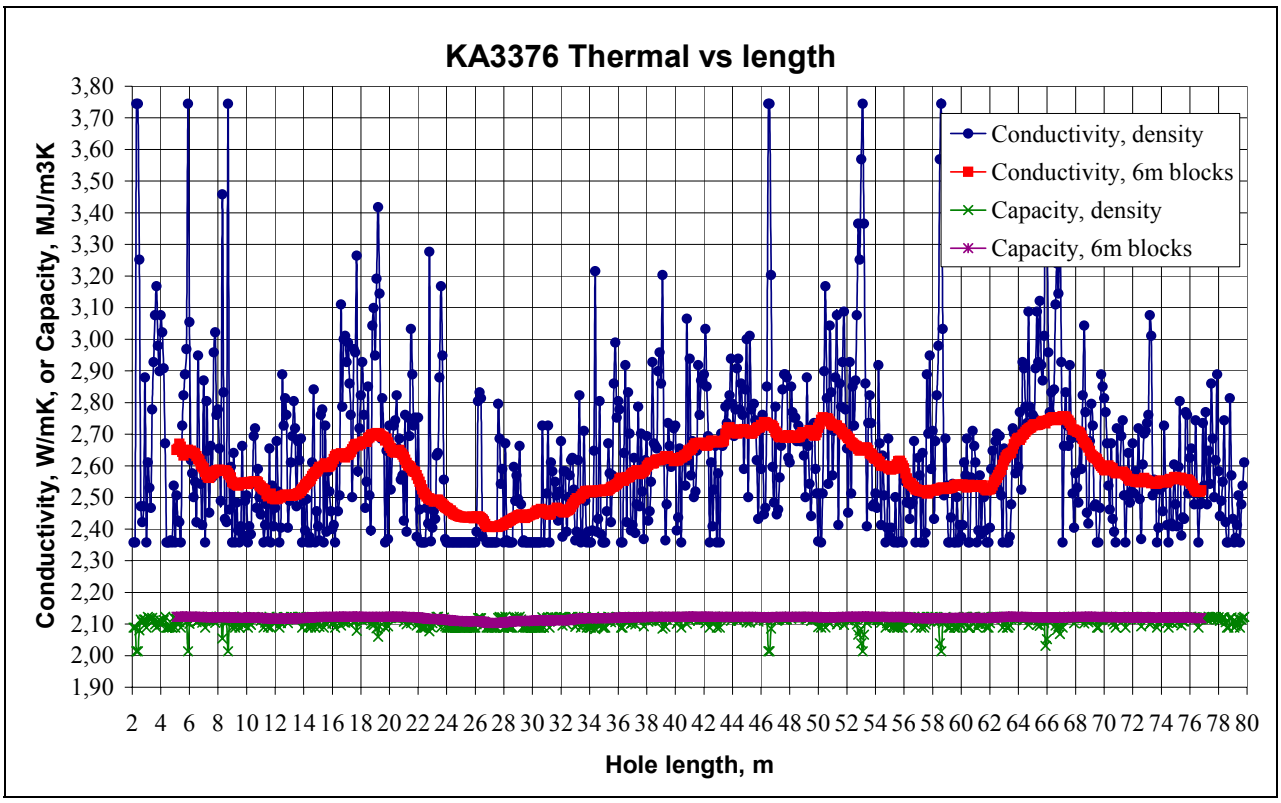

Figure 5-9. *Predicted thermal properties in borehole KA3376B01.*

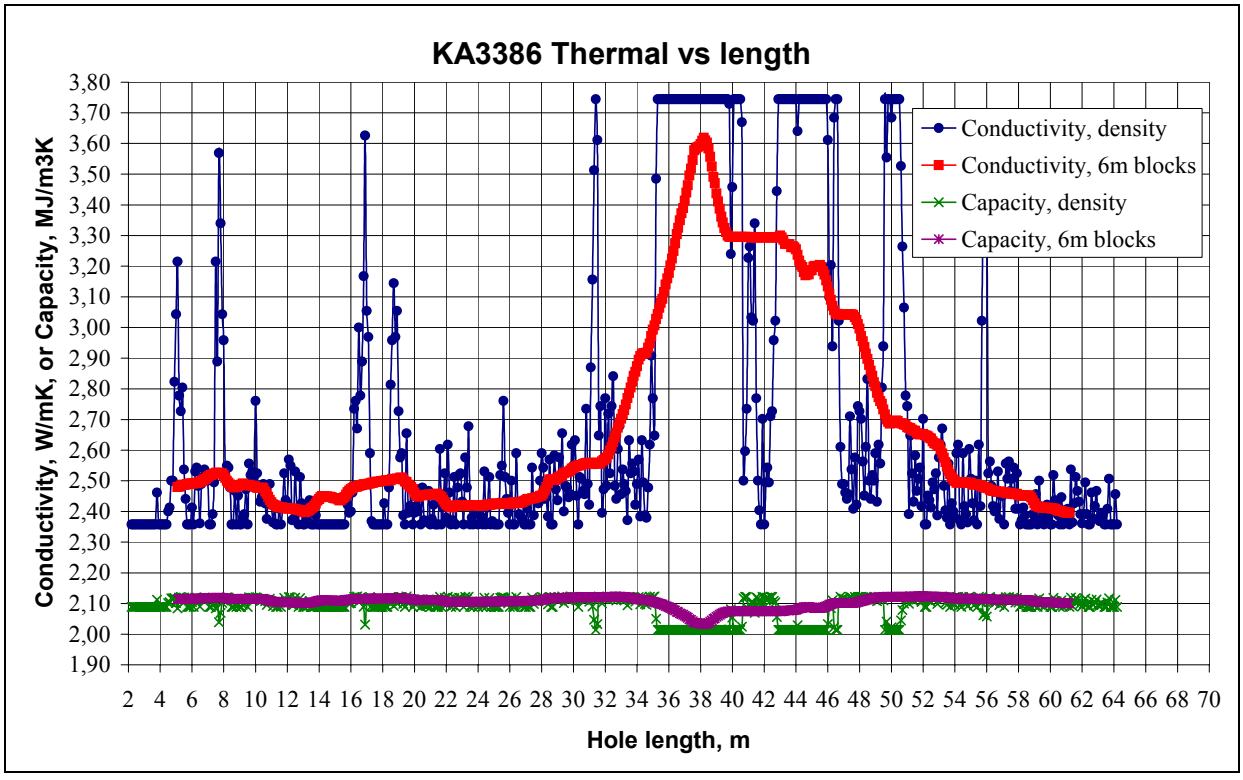

Figure 5-10. *Predicted thermal properties in borehole KA3386A01.*

There is a significant difference in the predicted thermal properties between the three experimental volumes. The heterogeneity in density is reflected in the thermal properties, and might be overestimated by the use of the relationships (see equations (4.1) and (4.2)). The occurrence of fine grained granite between lengths 35.5 and 46.4m in KA3386A01 is marked by high thermal conductivity and low thermal capacity values.

The variations in thermal capacity are almost insignificant between the 4 boreholes, see Table 5-7. Thermal conductivity is more sensitive to the geology, and to the chemical composition of rock types. The discrepancy observed on density in section 5.2 is also enhanced for thermal properties between the three experiment volumes, see Table 5-7.

Table 5-7. Mean value and standard deviation for predicted thermal properties

Borehole	Thermal conductivity, W/m, K		Thermal capacity, MJ/m^3, K	
	Mean value	Standard deviation	Mean value	Standard deviation
KF0066A01	3.107	0.229	2.092	0.022
KF0069A01	3.012	0.411	2.089	0.033
KA3376B01	2.626	0.257	2.108	0.017
KA3386A01, including the granite section	2.715	0.494	2.090	0.035
KA3386A01, excluding the granite section	2.545	0.305	2.101	0.021

The natural variation in thermal properties in KA3386A01 (Figure 5-10) might be affected by the cut-off applied on raw density data. Indeed from top down to 30m the curve exhibits a most uniform shape.

Curves drawn for boreholes KF0066A01 (Figure 5-7) and KF0069A01 (Figure 5-8) do not exhibit the same trend and present a larger standard deviation in the calculated thermal properties.

5.4 Conclusions

The density logging and predicted thermal conductivity observed in KA3386A01 and KA3376B01 are slightly different as those obtained for boreholes KF0066A01 and KF0069A01.

Density is in average higher for the same rock type, and predicted thermal properties lower, in experiment volumes 2 and 3 (KA3386A01 and KA3376B01) than in experiment volume 1. Two main explanations can be found to explain this discrepancy:

- calibration problems when the measurement equipment was moved from a borehole to another;
- the diorite encountered in experiment volumes 2 and 3 is of different composition as the one found in experiment volume 1. The higher density and lower thermal conductivity point to dominance of “pure” Äspö diorite while the diorite in KF0066A01 and KF0069A01 might be a mixture of the different rock types identified as diorite (Ävrö granite, mingled Ävrö/Äspö diorite and altered Ävrö granite) in the preliminary mapping, see Sundberg (2002a).

6 Analysis of the spatial variation of mechanical and thermal properties

6.1 Objectives

The mechanical and thermal properties determined in sections 4 and 5 are to be used in the coupled thermo-mechanical modeling done in correlation to the Äspö Pillar Stability Experiment. As illustrated especially in section 5 properties might vary significantly along a borehole and also between different boreholes.

An important issue is to be able to predict the mechanical and thermal properties with a good accuracy in the experiment volumes, and between the pilot boreholes. This might be assessed by studying and characterizing the spatial variability and correlation of the parameters.

The success of the experiment is partially based on the accuracy of the estimated properties on which the modeling is grounded. In the eve of the Äspö Pillar Stability Experiment mechanical and thermal properties in the rock mass prior to the experiment are based on general knowledge of the site, and data processes from the 4 new drilled boreholes.

The issue is then how to determine mechanical and thermal properties of the rock mass in the potential pillar from data obtained at discrete points in the pilot boreholes. What confidence do we have in the estimation of the properties and that they are valid for the pillar.

One of the issues is to determine how many pilot holes are required to drill from the floor of the tunnel to have a good and confident estimation of the parameters in the potential pillar.

6.2 Methodology

The analysis of density, thermal conductivity and thermal heat capacity enhanced a correlation between density and thermal properties, see section 4.2.2. This implies that the variation of thermal properties can be assessed from the variation of density combined with the uncertainty given in the equation of the relationships. Density along the boreholes can be considered completely known as measurements are done every 10 cm.

The spatial variability of density has been studied by means of:

– basic statistics analysis: mean value and standard deviation of density along each borehole, all rock types and according to rock type;

– variogram modeling on density: based on core logging data for each borehole.

6.3 Presentation of results from basic statistics

The stochastic distribution of a parameter is generally described by its mean value and standard deviation. Density logging data in the 4 new drilled boreholes, see section 5, have been studied and the mean value and standard deviation are listed for each alternative in Table 6-1.

Table 6-1. Mean value and standard deviation of density in the three alternative locations

All geology	*BH_id*	*Nb of samples*	*Density(g/cm^3)*	
			Mean value	Std dev.
Alternative 1	KF0066A01	569	2.679	0.021
	KF0069A01	667	2.692	0.048
	KA2599G01	28	2.691	0.042
	Combined	**1264**	**2.686**	**0.038**
Alternative 2	KA3386A01	621	2.734	0.076
Alternative 3	KA3376B01	778	2.742	0.05

As the occurrence of aplite is shown to have a significant influence on density, see section 5.2, the density data corresponding only to the diorite have been extracted, and the calculated mean values and standard deviation are presented in Table 6-2.

Table 6-2. Mean value and standard deviation of density of the diorite in the three alternative locations

Only diorite	*BH_id*	*Nb of samples*	*Density (g/cm^3)*	
			Mean value	Std dev.
Alternative 1	KF0066A01	513	2.682	0.019
	KF0069A01	379	2.712	0.045
	KA2599G01	23	2.695	0.042
	Combined	**915**	**2.695**	**0.036**
Alternative 2	KA3386A01	483	2.751	0.042
Alternative 3	KA3376B01	754	2.738	0.046

Some comments can be made from the results of this analysis:

- There is a significant difference in the mean value of density for diorite along KA338601 and KA3376B01 compared to what is observed along KF006601 and KF006901. This might be caused by problems in calibration of the equipment, or differences of geology.
- The term diorite refers to different rock types, and the density inside the diorite can vary quite a lot (see section 5.2).
- Further analyses are required to identify the origin of discrepancy, and whether the diorite body can be assumed similar in the three alternative locations or if distinct geological areas must be determined and characterized.

6.4 Variogram modeling

The aim of the variogram modeling is to assess the spatial correlation of density along the four boreholes.

6.4.1 Assumptions

– The diorite is older than the aplite and we can consider that the variogram is valid even if the data corresponding to occurrence of aplite or other subordinate rock types are removed from the data sets. These occurrences are generally less than 1 m thick, except in KA3386 where the aplite occurrence is about 15 m thick).

– Based on geographical position of the boreholes we assume that it is the same diorite body we encounter in the different boreholes. We are then able to calculate a variogram on data from the 3 boreholes KF0066A01, KF0069A01 and KA3386A01. *Note: density logging data from KA3376B01 could not be integrated in the study for time reason.*

6.4.2 Presentation of the variograms

The variograms obtained on density data for boreholes KF0066A01, KF0069A01 and KA3386A01 are illustrated in Figure 6-1 to Figure 6-3.

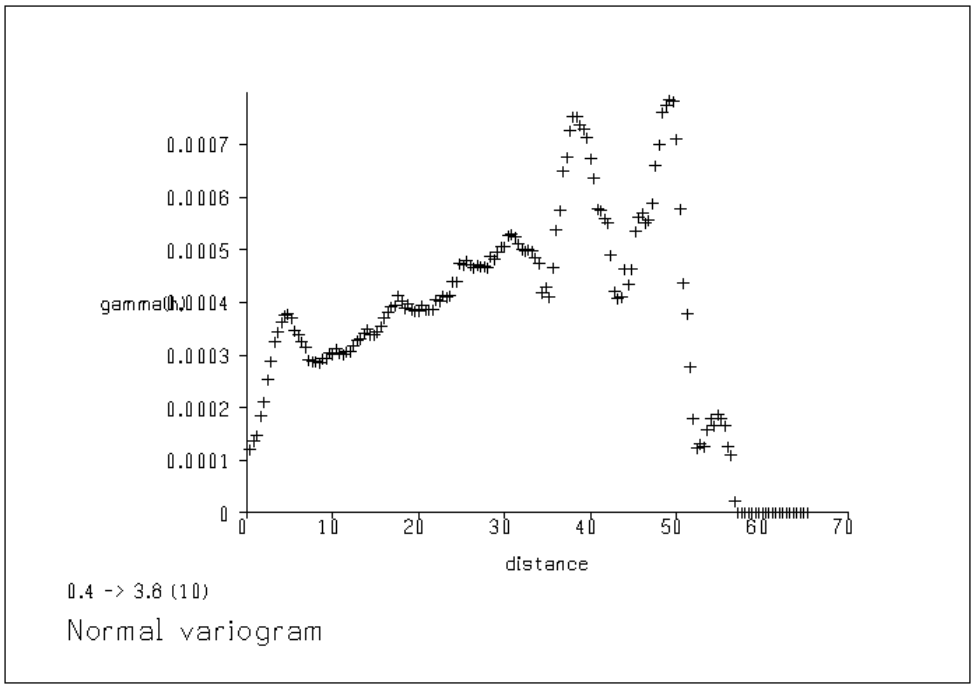

Figure 6-1. *Variogram of density logging data for the diorite, KF0066A01.*

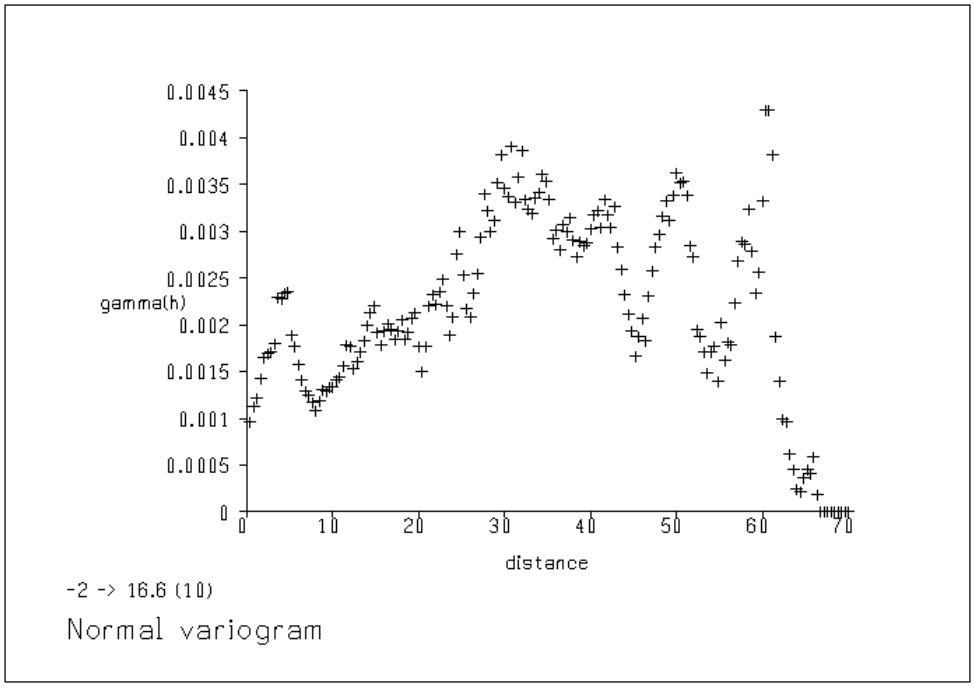

Figure 6-2. *Variogram of density logging data for the diorite, KF0069A01.*

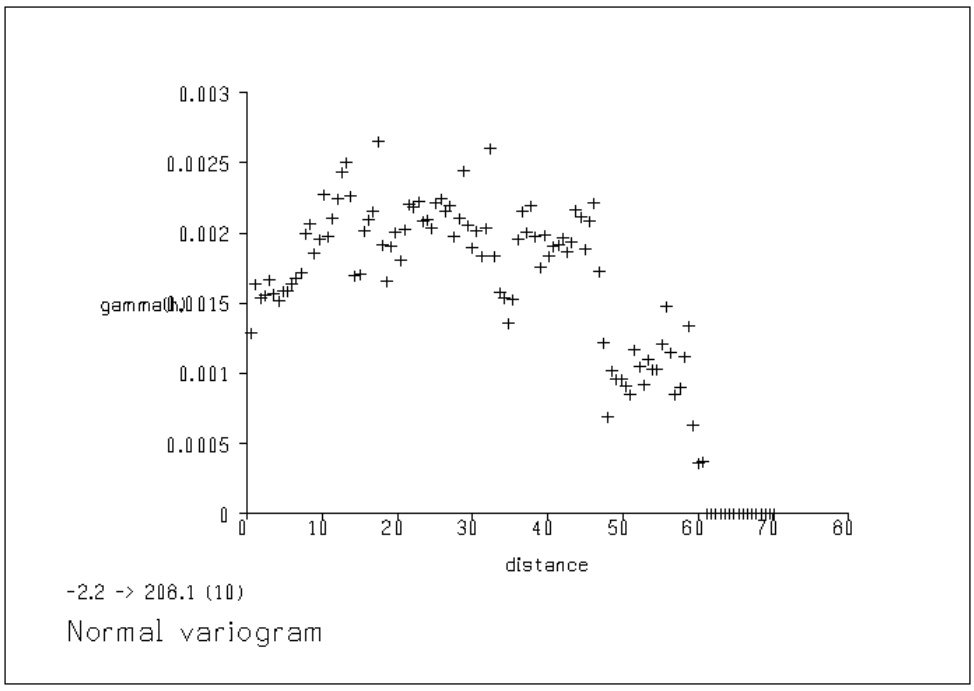

Figure 6-3. *Variogram of density logging data for the diorite, KA3386A01.*

The following comments can be made from the analysis of the variograms:

– The variograms calculated from density logging data on diorite show a poor correlation along all three boreholes.

– The correlation distance estimated from the different boreholes is around 5 meters, and the variograms present a high nugget.

– The significant variations in the variograms indicate changes in population though only the diorite has been analysed. But the identification of diorite sections is based on general geological mapping, and no distinction could be made between the different rock types mapped under the term "Äspö diorite", see section 4.1.1.

The analysis of the variograms leads to the conclusion that the spatial variability of density can be described as the sum of locally independent fluctuations, and density is considered as an "average building" process.

As there is apparently no clear spatial correlation on density the spatial variability can be studied by means of the average value. According to Vanmarcke (1977) the stochastic description of a soil property u(z) consists of the average value, $\overline{u}$, the standard deviation $\tilde{u}$, which have been presented in section 6.3, and the scale of fluctuation δ_u. The scale of fluctuation defines a distance within which the property u(z) shows a relatively strong correlation or persistence from point to point. This parameter might be a way to better characterise the spatial variability of density.

6.5 Determination of the scale of fluctuation

A short review of the definition of the scale of fluctuation is presented in section 6.5.1. Then the methodology is applied to density data from boreholes drilled in the three experiment volumes and the results are presented in section 6.5.2.

6.5.1 Definition of the rms reduction factor

The definition of the scale of fluctuation δ_u is related to the use of spatial averages. This means that the raw data along the borehole are averaged by increasing the averaging distance n.

The standard deviation is then calculated from the averaged values for each n value, and the spatial variability of the soil/rock properties is assessed by studying the decay of the standard deviation when the averaging distance increases. The main idea is that the larger the length over which the property is averaged, the more fluctuations of the parameter tends to disappear in the process of spatial averaging. This tends to cause a reduction in standard deviation as the size of the averaging length increases. The rms (root-mean square) reduction factor expresses the ratio between the "point" standard deviation (as calculated in section 6.3) and the "spatial average" standard deviation:

$$\Gamma_u(n) = \frac{\tilde{u}_n}{\tilde{u}}$$

with $\tilde{u}_n$ "spatial averages" standard variation

$\tilde{u}$ "point" standard deviation

Practically the first step is to evaluate the mean ū and the "point" standard variation ũ of the all population. Then the spatial averages are calculating by increasing the averaging distance n. Adjacent observations are averaged pairwise, and the standard deviation $\tilde{u}_n$ of the resulting "spatial averages" is computed (Vanmarcke, 1977). The process is repeated by increasing the number of adjacent observations that are averaged, n. The rms reduction factor, $\Gamma_u(n)$, is plotted against n.

Vanmarcke (1997) studied the relationships between the scale of fluctuation and the parameters of correlation functions. He gives that the theoretical expression of the rms reduction factor can be expressed by the following expression:

$$\Gamma_u(n) = \left[\frac{\delta_u}{\Delta z} \right]^{1/2} \quad \text{for } \Delta z > \delta u$$

with $\Delta z = n \cdot \Delta z_0$

$$\Gamma_u(n) = 1 \quad \text{for } \Delta z \le \delta u$$

Δz is the interval depth of spatial averaging, and Δz_0 is the interval between measuring points.

Vanmarcke (1977) also illustrates that this function gives an appropriate approximation of the variance function regardless the form of the underlying correlation function. This equation does however not provide information on the pattern of the correlation decay at small intervals ($\Delta z \le \delta u$).

The scale of fluctuation is approximated when the curve for predicted values reaches an asymptote and approaches the theoretical values. The scale of fluctuation δu is obtained by the following equation:

$$\delta_u = n \cdot \Gamma_u^{\,2}(n) \cdot \Delta z_0 = n^* \cdot \Delta z_0$$

in which

$$n^* = n \cdot \Gamma_u^{\,2}(n)$$

If n* is closed to one, the scale of fluctuation will seriously be overestimated and it means that the discrete observations are essentially uncorrelated.

6.5.2 Application to density data from boreholes KF0066A01, KF0069A01, KA3376B01 and KA3386A01

The rms reduction factor has been calculated for different averaging distances from raw density data for the new drilled boreholes in the three experiment volumes. The curves are illustrated in Figure 6-5 and Figure 6-4 for KF0066A01 and KF0069A01, boreholes in alternative 1. The theoretical curve has been back-calculated from the defined parameters to check the validity of the values. The interpreted scale of fluctuation is presented in Table 6-3.

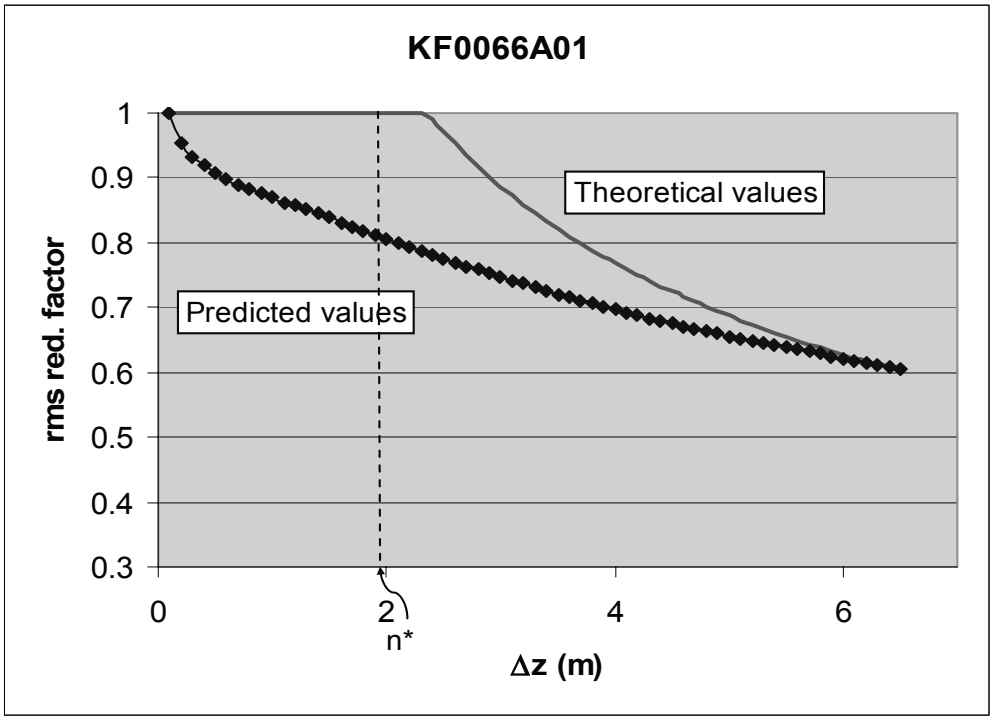

Figure 6-4. *rms reduction factor for an increasing averaging distance n, borehole KF0066A01.*

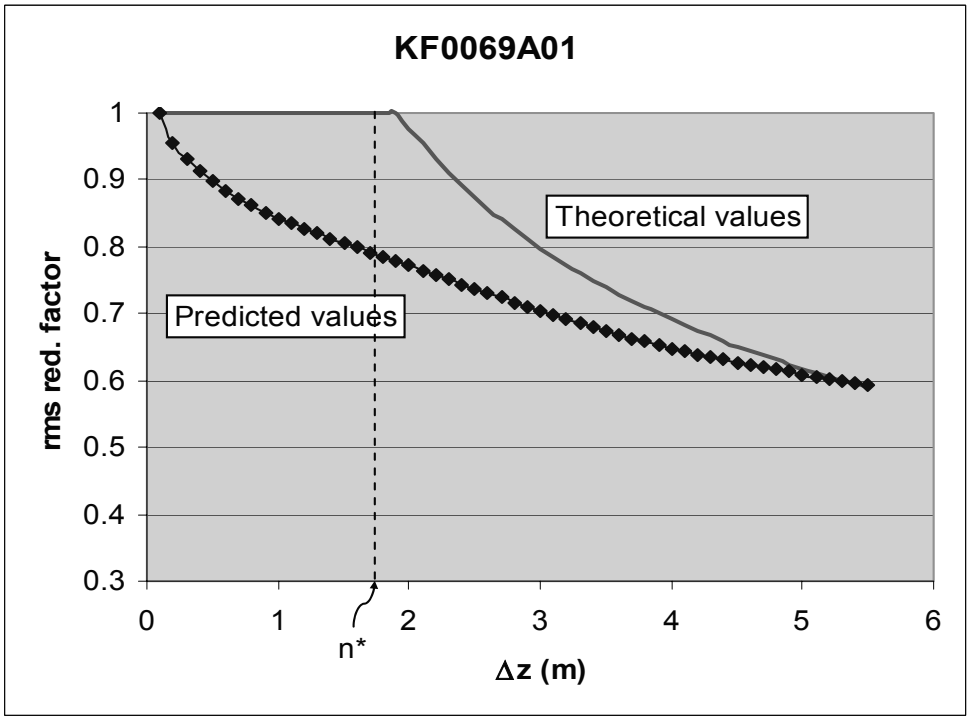

Figure 6-5. *rms reduction factor for an increasing averaging distance n, borehole KF0069A01.*

Considering the occurrence of the 15-m thick granite slab between 35.4 and 46.4 m along borehole KA3386A01 (alternative 2), the core might be divided in three independent sections, of which two have almost the same geology, diorite. Hence the spatial variability and scale of fluctuation of the diorite might be analysed by defining two populations:

– Population 1, from 3.6 down to 35.4 m;

– Population 2, from 46.4 to 64.2 m.

The rms reduction factor for both populations is illustrated in Figure 6-6 and Figure 6-7. The interpreted scale of fluctuation is presented in Table 6-3.

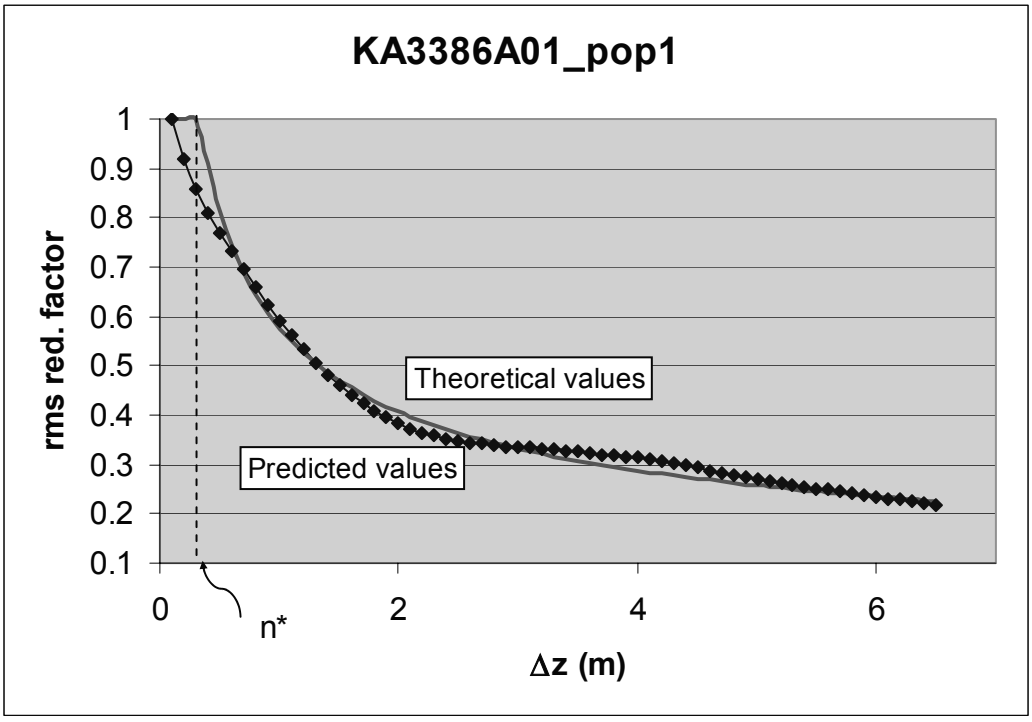

Figure 6-6. *rms reduction factor for an increasing averaging distance n, population 1, borehole KA3386A01.*

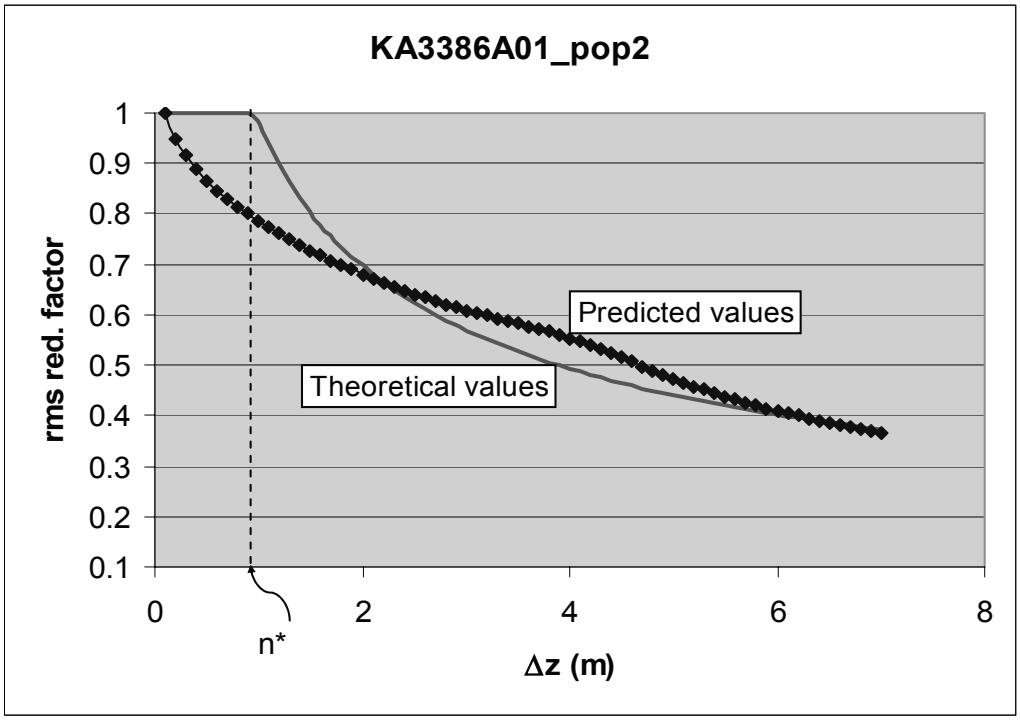

Figure 6-7. *rms reduction factor for an increasing averaging distance n, population 2, borehole KA3386A01.*

The geology core logging along KA3376B01 (alternative 3) can be considered as homogeneous and constituted of diorite. The estimation of the rms reduction factor vs the averaging distance n is illustrated in Figure 6-8.

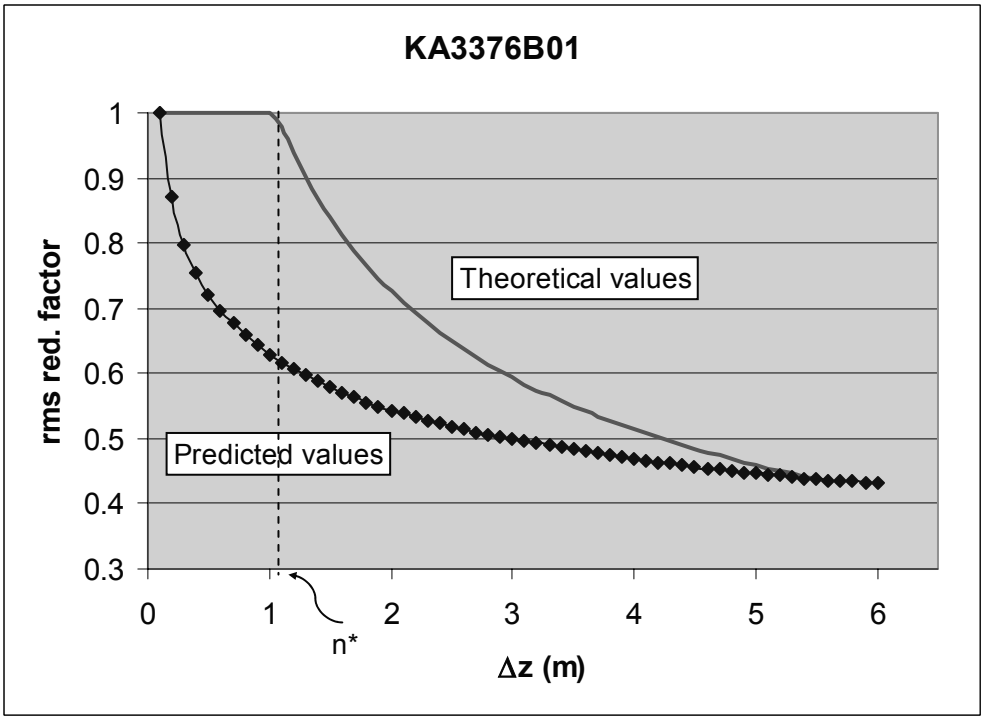

Figure 6-8. *rms reduction factor for an increasing averaging distance n, borehole KA3376B01.*

The interpretation of the curve and the estimated scale of fluctuation is presented in Table 6-3.

Table 6-3. Interpretation of the rms reduction factor and estimation of the scale of fluctuation

Hole ID	Δz (m)	Γ_u (n)	Scale of fluctuation, δ_u (m)
KF0066A01	6.3	0.612048	2.36
KF0069A01	5.3	0.600314	1.91
KA3386A01_pop1	6	0.234884	0.33
KA3386A01_pop2	6.5	0.386751	0.97
KA3376B01	5.5	0.438124	1.06

We can notice a distinct difference between boreholes of alternative 1 (KF0066A01 and KF0069A01) and boreholes of alternative 2 (KA3386A01) and 3 (KA3376B01). The scale of fluctuation for alternatives 2 and 3 is very low, less or equal to 1, whereas the scale of fluctuation in alternative 1 is closed to 2.

This can be correlated to the shape of the curves. The rms reduction factor decreases very fast in KA3386A01, especially for population 1, see Figure 6-6, and KA3376B01, see *Figure 6-8*, but the curves are much more regular in alternative 1 (see Figure 6-4 and Figure 6-5).

Another method can be applied to estimate the scale of fluctuation, δ_u. This is based on the approximate relationship between the scale of fluctuation δ and the average distance, $\overline{d}_u$, between the intersections of the fluctuating property and its mean value (Vanmarcke, 1977). The scale of fluctuation can be expressed approximately:

$$\delta_u = \frac{1}{\sqrt{\pi/2}} \cdot \overline{d}_u \approx 0.8\overline{d}_u$$

The results obtained of the boreholes for the three alternatives are summarized in Table 6-4.

Table 6-4. Scale of fluctuation estimated from "mean crossings"

Hole ID	Sum of "mean crossings"	$\overline{d}_u$, m	δ_u, m
KF0066A01	138	0.41	0.33
KF0069A01	108	0.62	0.49
KA3386A01_pop1	96	0.33	0.26
KA3386A01_pop2	48	0.37	0.3
KA3376B01	270	0.29	0.23

We can notice a significant difference in the values of the scale of fluctuation regarding the evaluation method, see Table 6-3 and Table 6-4. An explanation might be that most of the "mean crossings" recorded along the boreholes are "point" variations of the property around the mean value and not "long wave" variations. If we take into consideration only the "mean crossings" sections over a distance greater than 0.5 m the results are significantly different, see Table 6-5.

Table 6-5. Scale of fluctuation estimated from "mean crossings", for sections longer than 0.5 m

Hole ID	Sum of "mean crossings"	$\overline{d}_u$, m	δ_u, m
KF0066A01	16	3.55	2.83
KF0069A01	22	3.03	2.41
KA3386A01_pop1	20	1.59	1.27
KA3386A01_pop2	10	1.78	1.42
KA3376B01	40	1.94	1.55

The scale of fluctuation evaluated from "mean crossings" on sections longer than 0.5 m , Table 6-5, is still slightly different as the one estimated from the rms reduction factor, Table 6-3, but both methods reflect the same process for each borehole.

6.6 Discussion and conclusions

On the basis of variogram modelling, spatial variability of density has been identified to be appropriately described by the spatial variability of its average value. As a consequence the most appropriate parameter to describe the spatial correlation, or persistence of the parameters, is the scale of fluctuation δ_u.

The estimated scale of fluctuation δ_u is significantly different between the 4 boreholes drilled in the three experiment volumes. The persistence is found to be around 2m in alternative 1 (boreholes KF0066A01 and KF0069A01), and closed to 1 m in alternatives 2 and 3 (boreholes KA3386A01 and KA3376B01). An exception must be made for the population 1 in KA3386A01 which shows almost no correlation at all.

The scale of fluctuation might be a decisive parameter to know for the estimation of the pre-experiment investigations. Indeed the distance between pilot boreholes might be defined from the knowledge of the scale of fluctuation. In this case considering the results presented in section 6.5 pilot boreholes every 2 meters might be recommended in alternative 1, but it might be required to drill pilot boreholes every meter in alternatives 2 and 3 to get an accurate estimation of density, and as a consequence of thermal properties, in the pillar.

7 Conclusions

Three experiment volumes have been investigated for the location of the Äspö Pillar Stability Experiment. These volumes are located close to -450 m depth. This report aimed to study the geology and properties of the rock mass around the experiment volumes in order to provide input data for the thermo-mechanical modeling and give support for the decision of location of the experiment.

A 200-m model domain was defined which includes the three experiment volumes and the 4 new drilled boreholes at these locations. A hydro-structural model has been established in order to identify the main structures and hydraulic conductors at the model scale. The following comments can be made on the developed model:

– All three alternatives are located in a "rock unit" block delimited by two major fracture zones that form an edge beside the model boundary. Nevertheless a minor fracture zone z4 cuts through boreholes KF0066A01 and KF0069A01 (alternative 1).

– The model illustrates that both alternatives 2 and 3 cut through sub-vertical hydraulic conductors oriented WNW. Moreover the structure identified at alternative 3 might be an indication at depth of the regional hydraulic structure NNW-1w.

– On the basis of indications in tunnels and in the new boreholes the hydraulic conductor WNW-1 might be connected to the major fracture zone NE2 and the minor fracture zone z4. The characterization of the transmissivity and connectivity pattern is required to establish the relations between these structures.

In situ stress data were estimated to be similar in the three experiment volumes as they are located in the same geological and structural unit. However the fact that these locations are quite close to the edge formed by two major fracture zones might influence the in situ stress field.

No mechanical or thermal determination tests were conducted on cores from the 4 drilled boreholes at the 3 alternative locations. However density and flow log were conducted. Hence mechanical and thermal properties of the rock mass around the three experiment volumes have been estimated from previously drilled boreholes.

A relationship was established between density and thermal conductivity and thermal heat capacity in a previously drilled borehole. This was applied on density data from the new drilled boreholes to obtain a representation of the spatial variability of the thermal properties at the experiment volumes. A detailed analysis of the variation of density and thermal properties along each borehole and between the different alternatives has been conducted.

The study of stochastic distribution of parameters could only be conducted in details on density. The spatial correlation of density along the 4 boreholes is very poor and the analysis shows that the spatial variability of density is best described by the spatial variability of its mean value. The scale of fluctuation can be used to describe the correlation distance or persistence of values from point to point.

The study of core data from the boreholes in the three experiment volumes combined to the results of the spatial variability analysis enhances that there is significant differences between alternative 1, and alternatives 2 and 3:

- Density is in general higher in boreholes KA3386A01 (alternative 2) and KA3376B01 (alternative 3) than in boreholes KF0066A01 and KF0069A01 (alternative 1). The difference might be due to discrepancy in the geology, or to calibration problems. Density data along borehole KA3386A01 exhibit extreme values and the log shows important variations from point to point.

- The correlation distance on density data is estimated to be around 2m in alternative 1, and close to 1m in alternatives 2 and 3. One section of borehole KA3386A01 (alternative 2) even shows almost no correlation.

References

Andersson, C. (2003). Äspö Pillar Stability Experiment, Feasibility study. SKB, IPR-03-01.

Andersson, C., Christiansson, R., Söderhäll, J. (2002). A correlation of rock mechanical conditions and maintenance records for the tunnels at the Äspö Hard Rock Laboratory. Proceeding for the NARMS Symposium. Toronto July 2002.

Andersson, P., Byegård, J., Dershowitz, B., Doe, T., Hermanson, J., Meier, P., Tullborg, E-V., and Winberg, A. 2002. Final report of the TRUE Block Scale project. 1.Characterisation and model development. TR-02-13, SKB.

Börgesson, L. and Hernelind, J. (1995). Decovalex I – Test case 3. Calculation of the Big Ben experiment. TR 95-29. Stockholm.

Hakami, E. (1995). Aperture distribution of rock fractures. Dr. Thesis, PHD 1003. Department of Civil and Environmental Engineering, Royal Institute of Technology. Stockholm.

Hakami, H., Hakami, E., Cosgrove, J. (2002). Strategy for a rock mechanics site descriptive model – development and testing of an approach to modelling the state of stress. SKB Report R-02-03.

Hansen, L.M., and Hermansson, J., 2002. Äspö Hard Rock Laboratory. Local model of the geological structures close to the F-tunnel, IPR-02-48, SKB.

Hermanson, J., Stigsson, M., and Wei, L. (1998). A Discrete Fracture Network model of the Äspö Zedex tunnel section. SKB PR-HRL-98-29, Stockholm.

Hudson, J and Stephansson, O. (1995). Thermo-hydromechanical coupling in rock mechanics. Int. J. of Rock Mech. and Min. Scie. & Geomech. Abstr. Vol 32, no 5. Pergamon.

Janson, T., Stigsson, M. (2002). Test with different stress measurement methods in two orthogonal bore holes in Äspö HRL. R-02-26, SKB.

Klasson, H., Persson, M., Ljunggren, C. (2000). Overcoring rock stress measurements at the Äspö HRL – Prototype repository: Borehole KA3579G (revised data) and K-tunnel: Borehole KK0045G01. SKB Report IPR-02-03.

Lanaro, F. (2001). Geometry, mechanics and transmissivity of rock fractures. Dr. Thesis, PHD 1043. Department of Civil and Enviromental Engineering, Royal Institute of Technology. Stockholm.

Larsson, K., Nordlund, E. and Dahlström, L-O. (2002). Determination of the coefficient of thermal expansion for two Äspö rocks, diorite and granite. NARMS-TAC 2002, Hammah et al (eds). 2002 University of Toronto.

Nordlund, E., Li, C. and Carlsson, B. (1999). Mechanical properties of the diorite in the prototype repository at Äspö HRL. SKB, IPR-99-25. Stockholm.

Olsson, O., Stanfors, R., Ramqvist, G., and Rhén, I. 1994. Localization of experimental sites and layout of turn 2 – results of investigations. PR 25-94-14, SKB.

Olsson, R. (1998). Mechanical and hydromechanical behaviour of hard rock joints, A laboratory study. Dr. Thesis. Deparment of Geotechnical Engineering, Chalmers Univesity of Technology. Göteborg.

Pöllänen, J., and Rouhiainen, P., 2002. Äspö Hard Rock Laboratory. Difference flow measurements in boreholes KA3386A01, KF0066A01 and KF0069A01 at the Äspö HRL. SKB, IPR-02-55.

Pöllänen, J., and Rouhiainen, P., 2003. Äspö Hard Rock Laboratory. Difference flow measurements in borehole KA3376B01 at the Äspö HRL. SKB, IPR-03-07.

Rhén, I., Danielsson, P., Forsmark, T., Gustafson, G., and Liedholm, M. 1993. Geohydrological evaluation of the data from section 1475-2265 m. PR 25-93-11, SKB.

Rhén, I., 1995. Comparative study between cored test borehole KA3191F and the first 200m extension of the TBM tunnel. SKB, PR 25-95-09.

Rhén, I., 1995. Documentation of tunnel and shaft data – Tunnel section 2874-3600 m, hoist and ventilation shafts 0-450 m. PR 25-95-28, SKB.

Rhén, I., Gustafson, G., Stanfors, R., and Wikberg, P. 1997. Äspö HRL – Geoscientific evaluation 1997/5. Models based on site characterization 1986-1995. TR 97-06, SKB.

Rhén, I., and Forsmark, T., 2000. Äspö Hard Rock Laboratory. High-permeability features (HPF). IPR-00-02, SKB.

SKB, 2002. Simpevarp – site descriptive model version 0. SKB, R-02-35.

Sjöberg, J. (2002). Äspö Hard Rock Laboratory. 3D overcoring rock stress measurements in borehole KA3376B01 at the Äspö HRL. SKB, IPR-03-16.

Stanfors, R., Liedholm M., Munier, R., Olsson, P., and Stille, H., 1994. Geological-structural and rock mechanical evaluation of data from tunnel section 2265-2874 m. PR 25-94-19, SKB.

Stanfors, R., Olsson, P., Stille, H. (1997). Äspö Hard Rock Laboratory – Geoscientific evaluation 1997/3. Results from pre-investigations and detailed site characterization. Comparison of prediction and observations. Geology and mechanical stability. SKB, TR-97-04.

Staub, I., Fredriksson, A. and Outters, N. (2002). Strategy for a rock mechanics site descriptive model – development and testing of the theoretical approach. SKB R-02-02. Stockholm.

Stille, H. and Olsson, P. (1989). First evalution of rock mechanics. SKB PR 25-89-07. Stockholm.

Sundberg, J. och Gabrielsson, A. (1999). Laboratory and field measurements of thermal properties of rocks in the prototype repository at Äspö HRL. IPR-99-17, Stockholm.

Sundberg, J. (2002a). Determination of thermal properties at Äspö HRL. Comparison and evaluation of methods and methodologies for borehole KA2599G01. R-02-27. Stockholm.

Sundberg, J. (2002b). Determination of linear thermal expansion – samples from borehole KA2599G01, Äspö HRL. SKB, IPR-02-63.

Vanmarcke, E. H. 1977. Probabilistic modeling of soil profiles. Journal of the Geotechnical Engineering, Div. ASCE, vol.103, No GT 11, Nov.1977.

Appendix A

Visualisation of RQD and fracture frequency along the sections of boreholes included in the 200-m model.

The fracture frequency is illustrated as a 2 y-axis graph plotting respectively the frequency of natural fractures and the frequency of fractures in crush zones when such are identified.

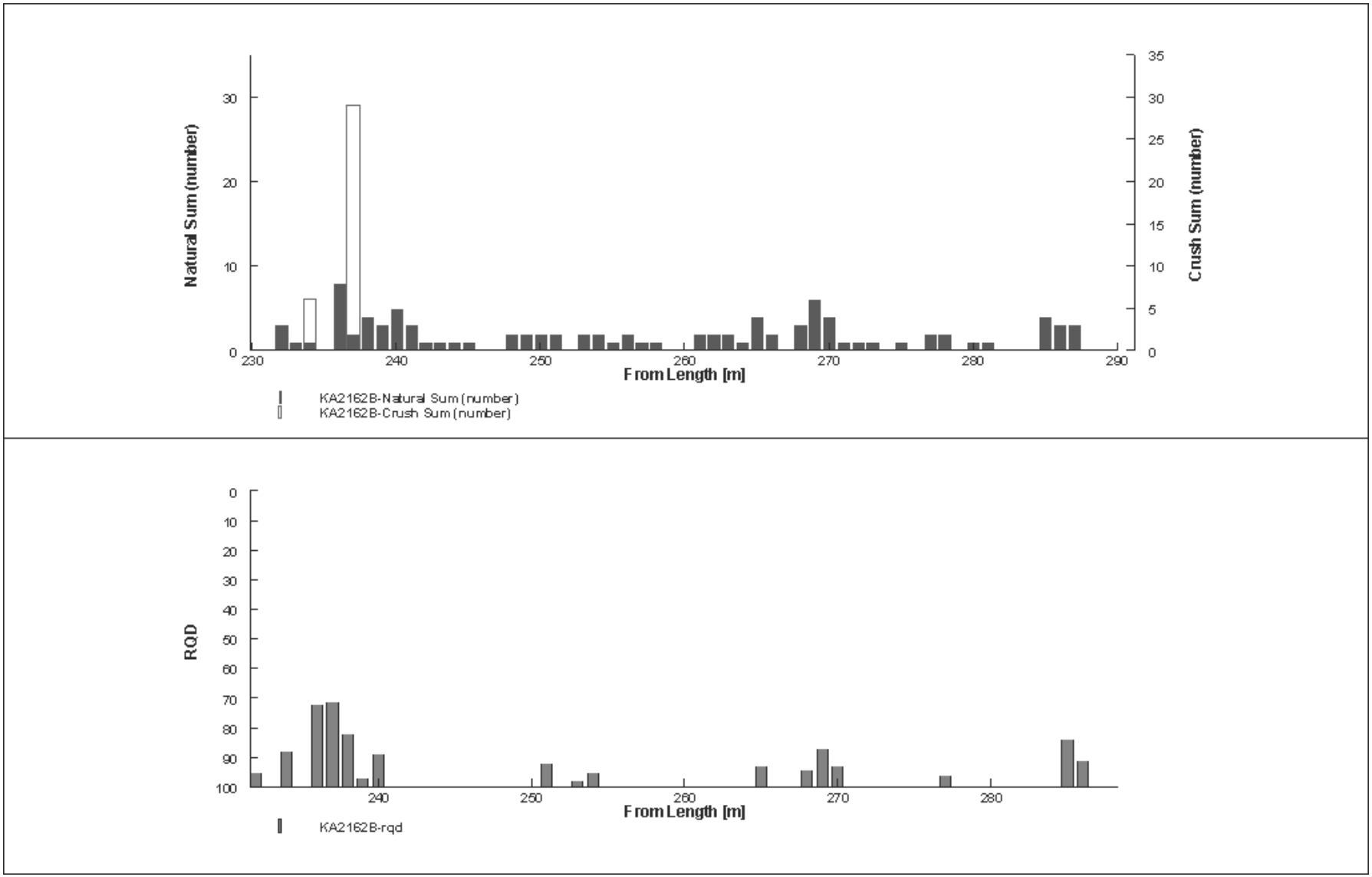
Natural Sum (number)
Crush Sum (number)
From Length [m]
KA2162B-Natural Sum (number)
KA2162B-Crush Sum (number)
RQD
From Length [m]
KA2162B-rqd

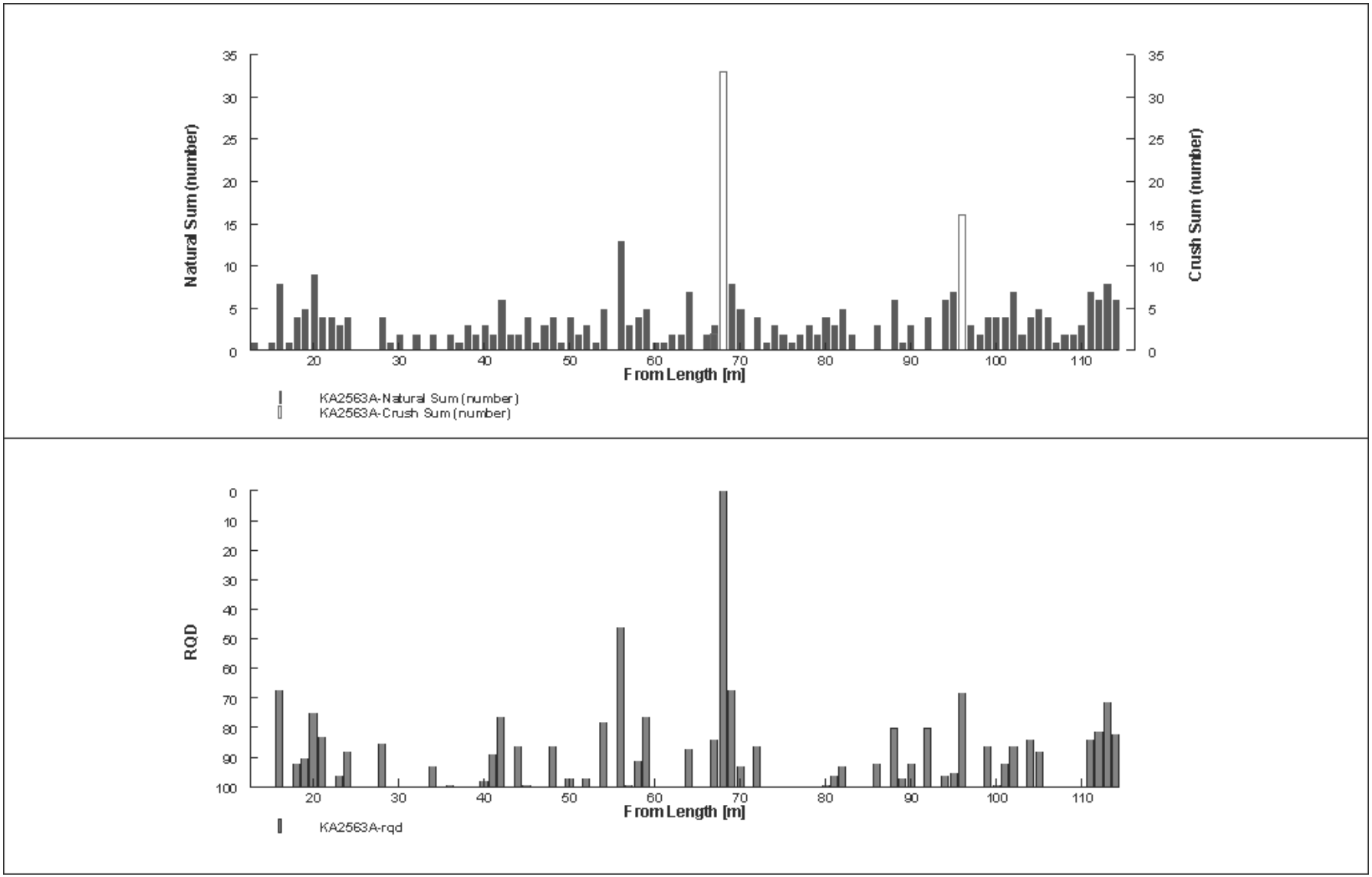
Natural Sum (number)
Crush Sum (number)
From Length [m]
KA2563A-Natural Sum (number)
KA2563A-Crush Sum (number)
RQD
From Length [m]
KA2563A-rqd

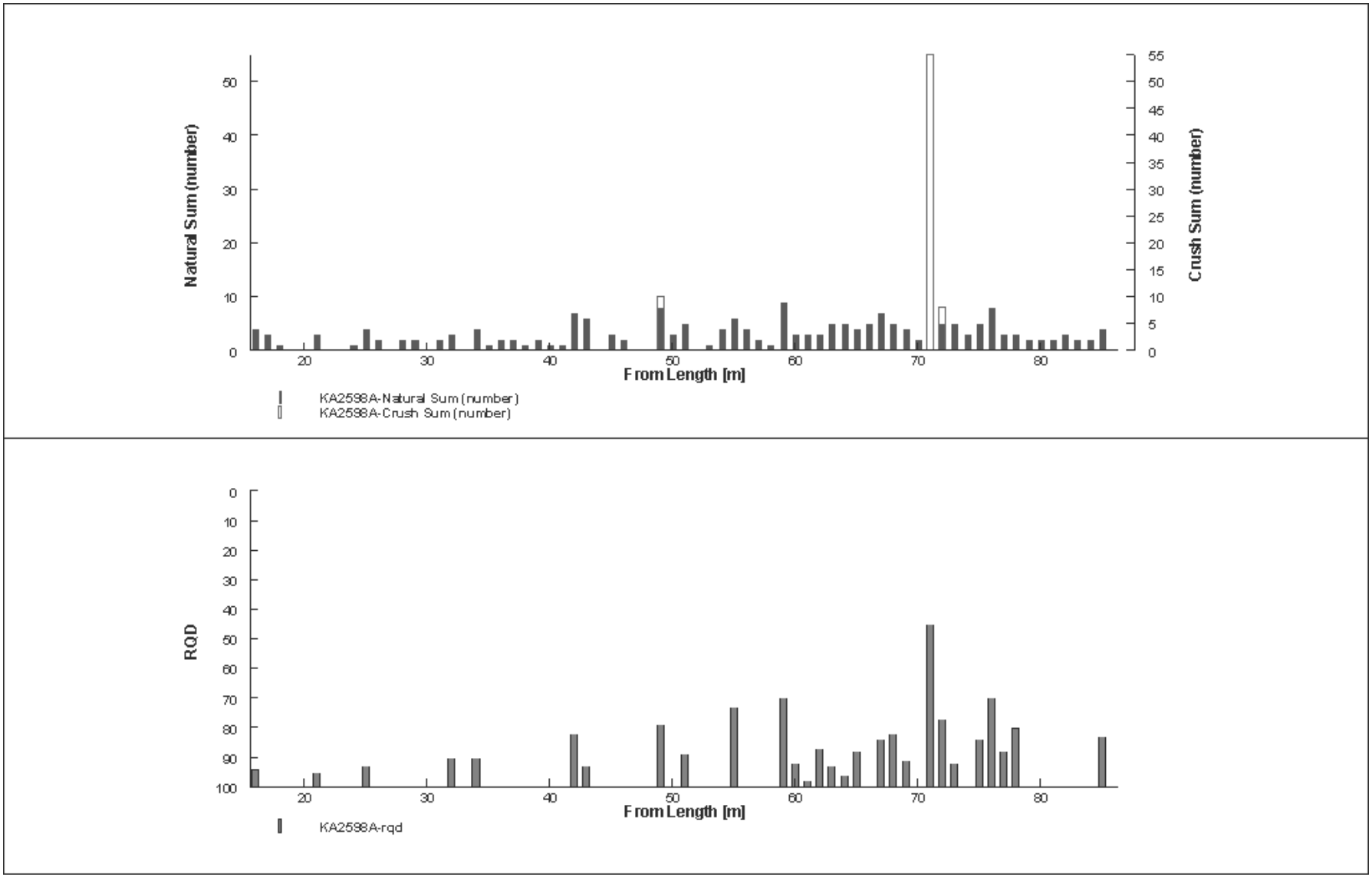
Natural Sum (number)
Crush Sum (number)
From Length [m]
KA2598A-Natural Sum (number)
KA2598A-Crush Sum (number)
RQD
From Length [m]
KA2598A-rqd

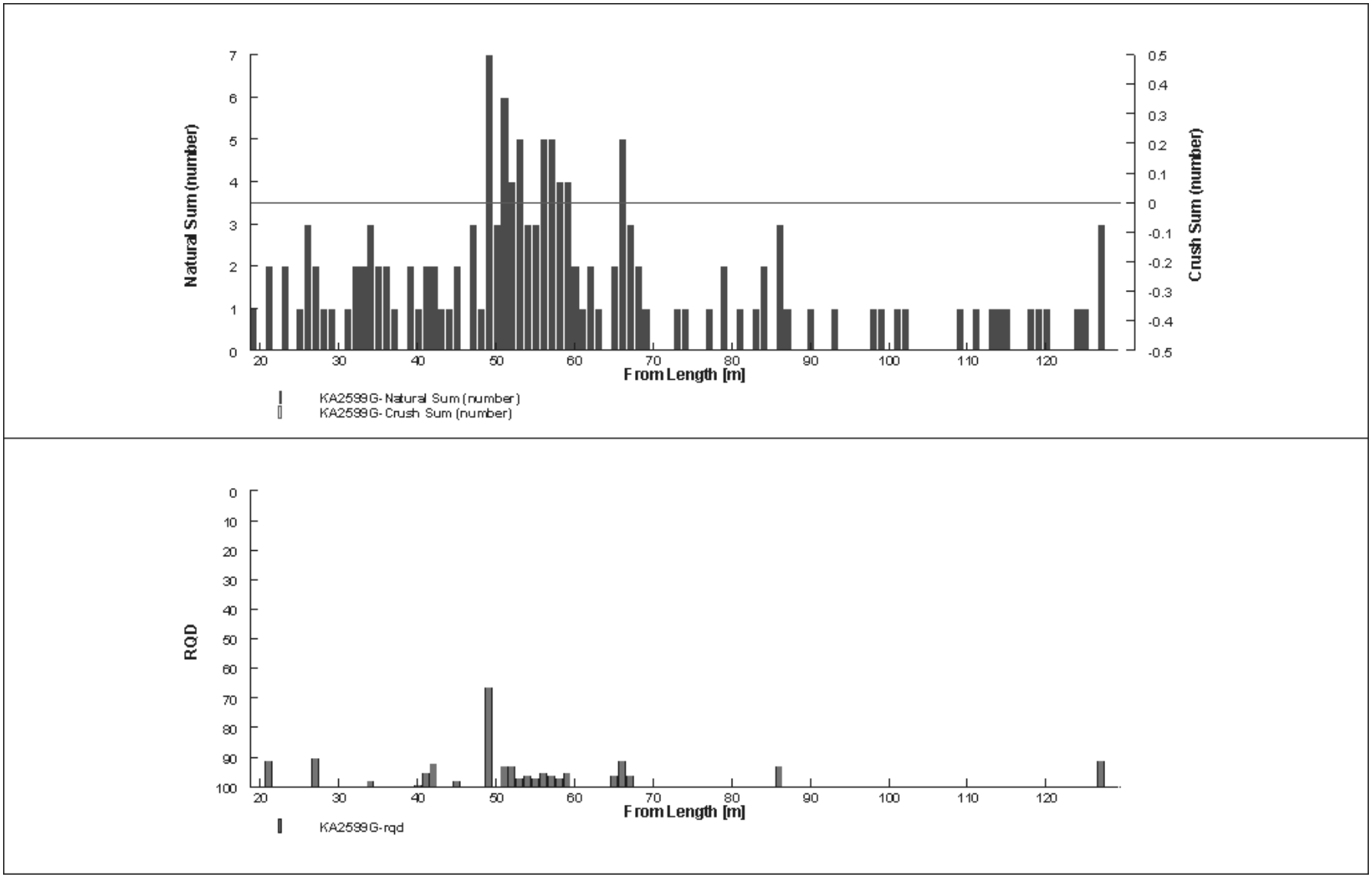
Natural Sum (number)
Crush Sum (number)
From Length [m]
KA2599G-Natural Sum (number)
KA2599G-Crush Sum (number)
RQD
From Length [m]
KA2599G-rqd

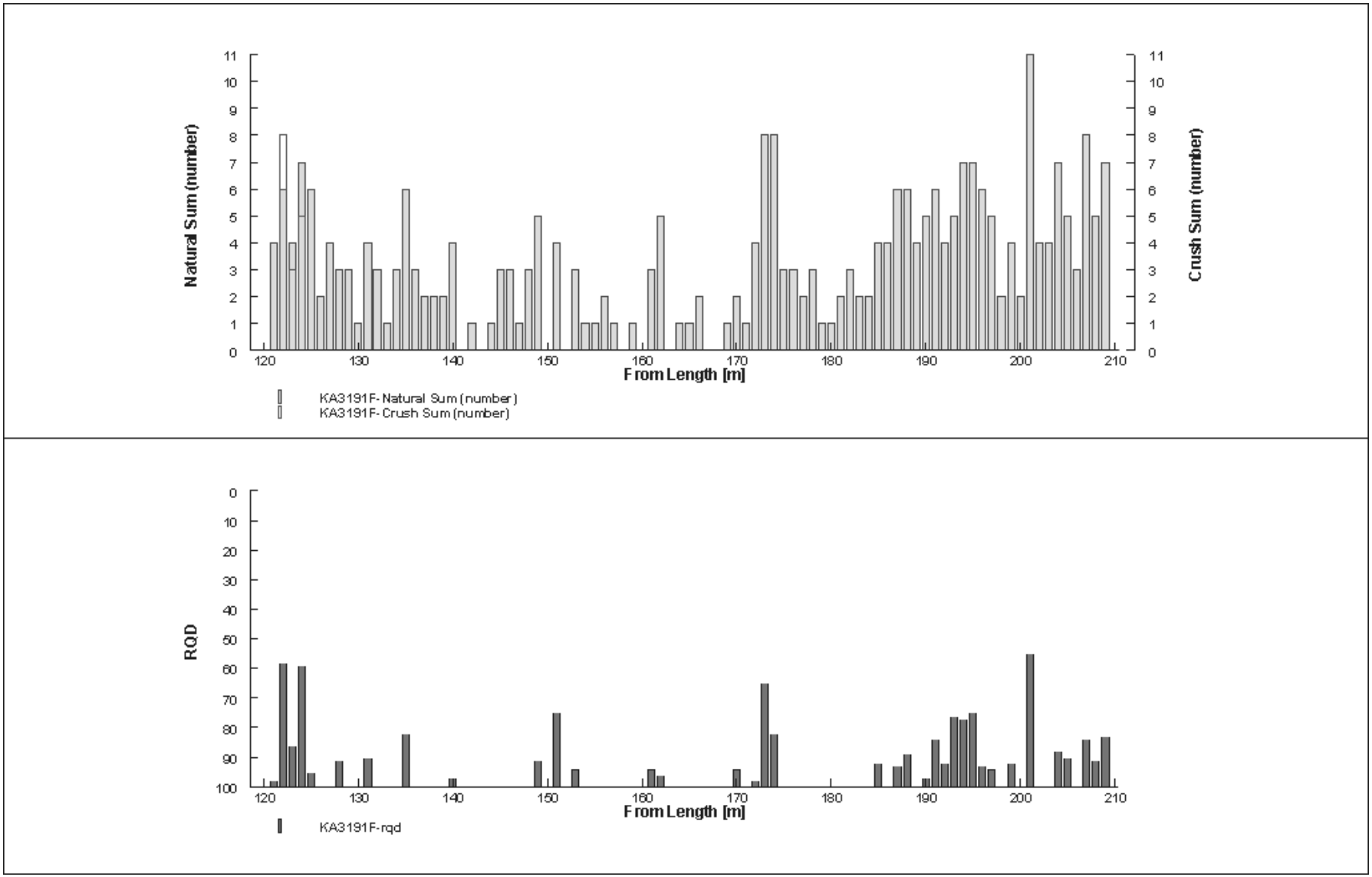
Natural Sum (number)
Crush Sum (number)
From Length [m]
KA3191F- Natural Sum (number)
KA3191F- Crush Sum (number)
RQD
From Length [m]
KA3191F-rqd

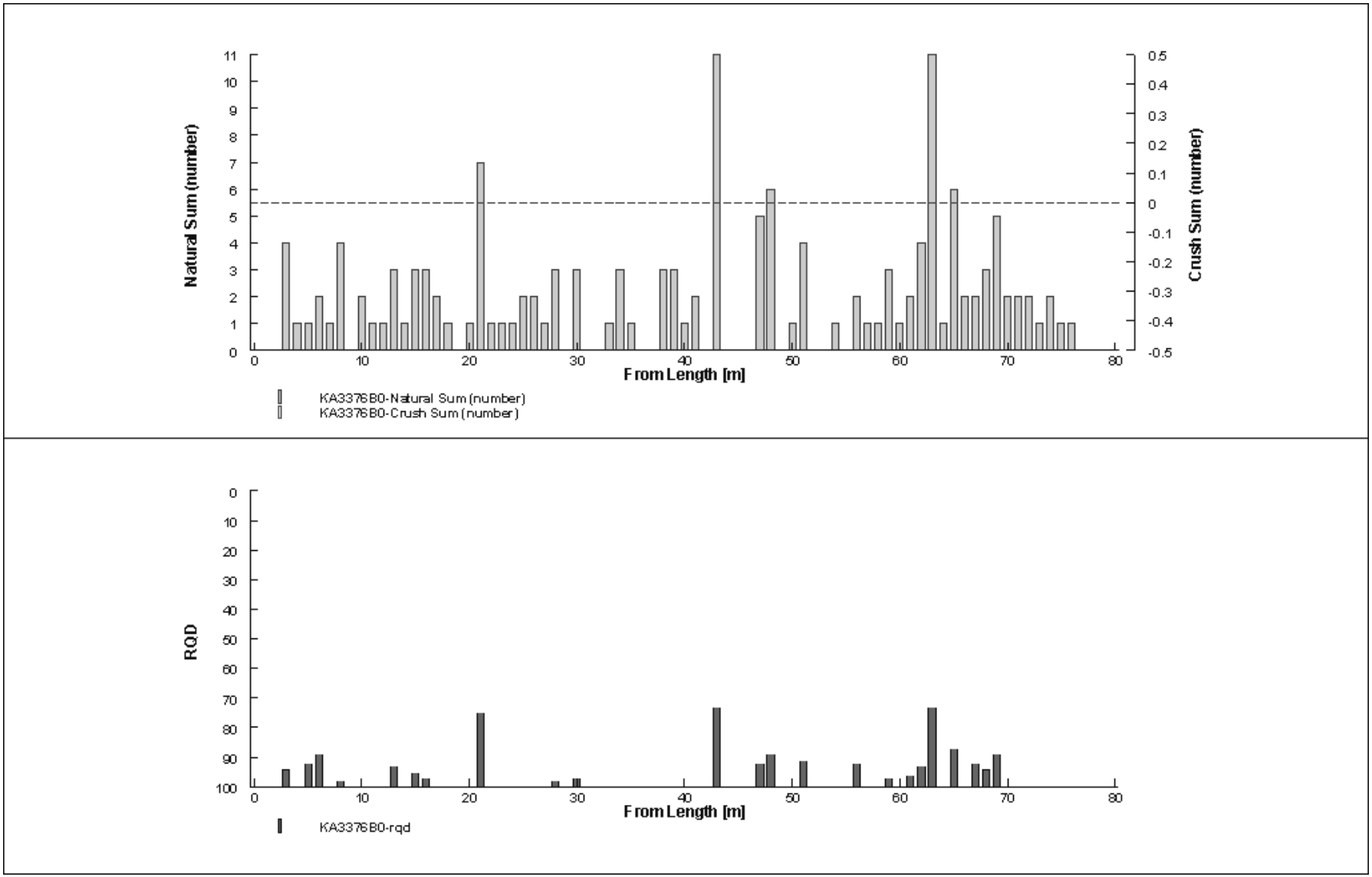
Natural Sum (number)
Crush Sum (number)
From Length [m]
KA3376B0-Natural Sum (number)
KA3376B0-Crush Sum (number)
RQD
From Length [m]
KA3376B0-rqd

No data for fracture frequency

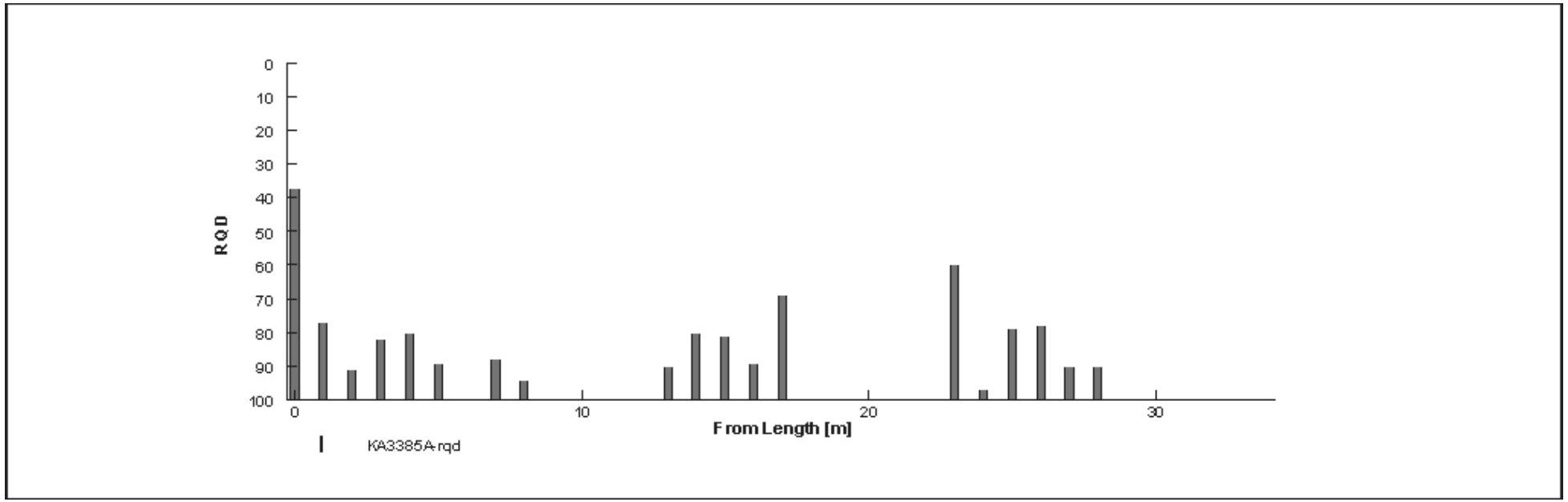

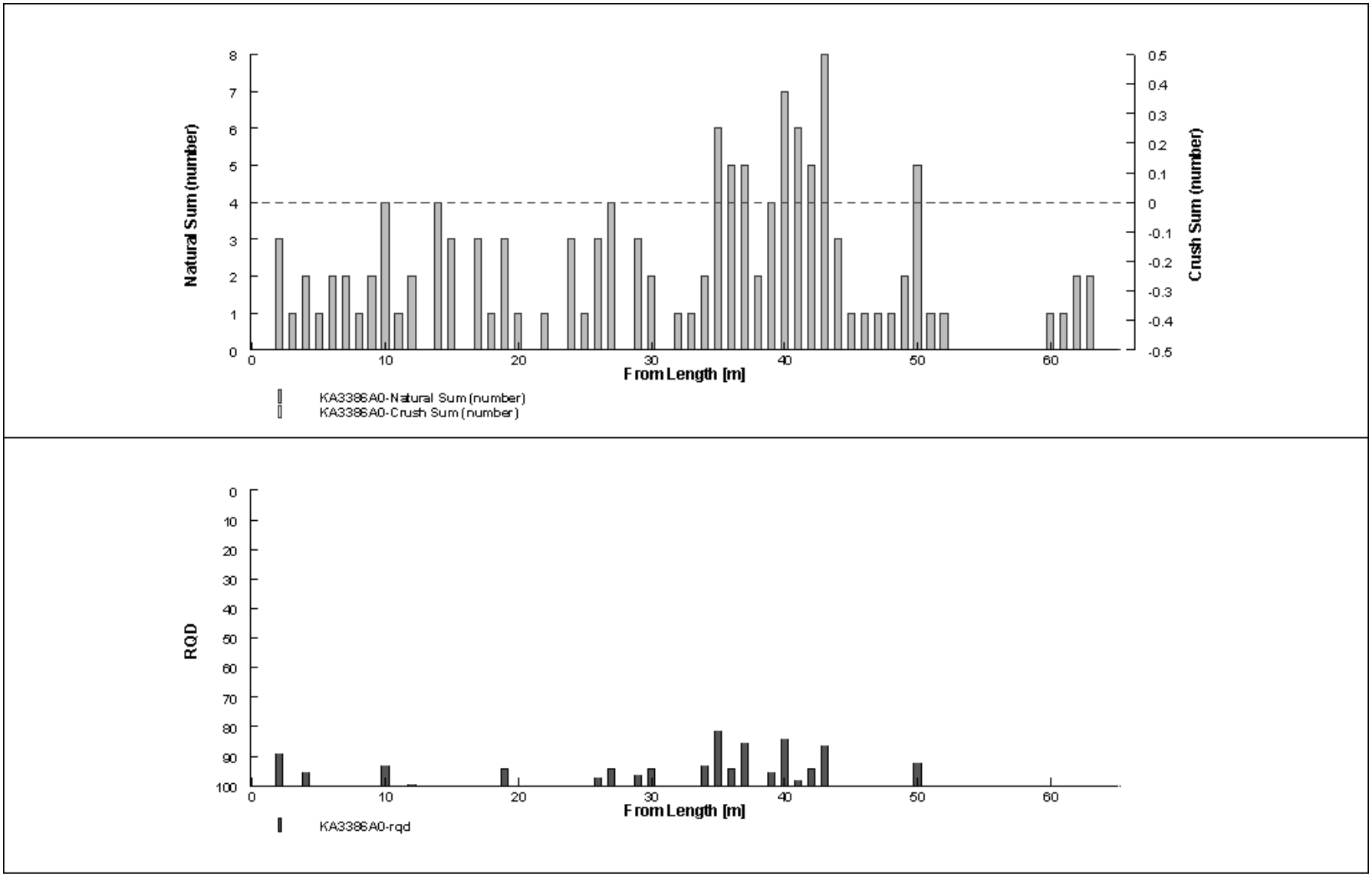
Natural Sum (number)
Crush Sum (number)
From Length [m]
KA3386A0-Natural Sum (number)
KA3386A0-Crush Sum (number)
RQD
From Length [m]
KA3386A0-rqd

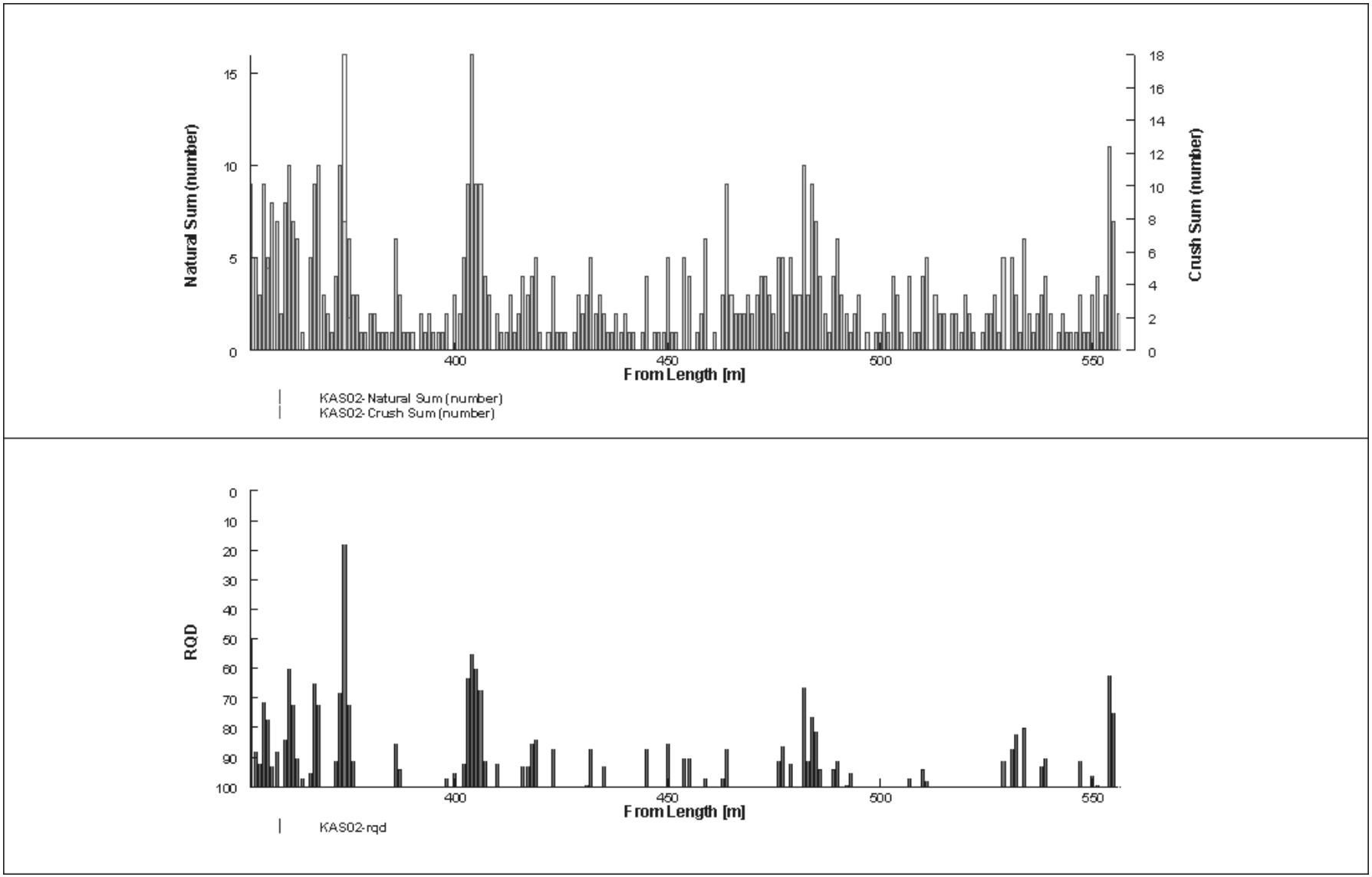
Natural Sum (number)
Crush Sum (number)
From Length [m]
KAS02-Natural Sum (number)
KAS02-Crush Sum (number)
RQD
From Length [m]
KAS02-rqd

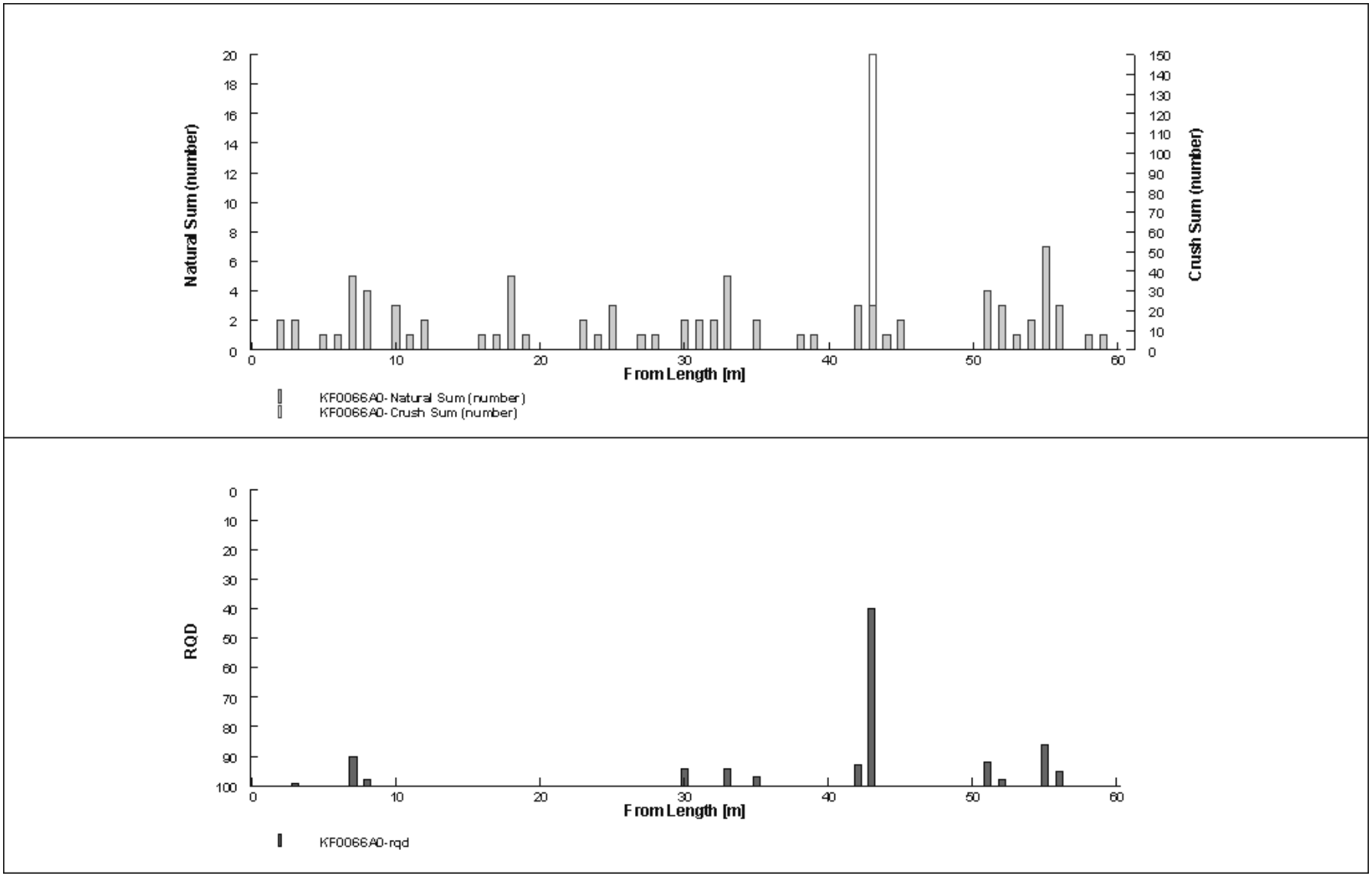
Natural Sum (number)
Crush Sum (number)
From Length [m]
KF0066A0-Natural Sum (number)
KF0066A0-Crush Sum (number)
RQD
From Length [m]
KF0066A0-rqd

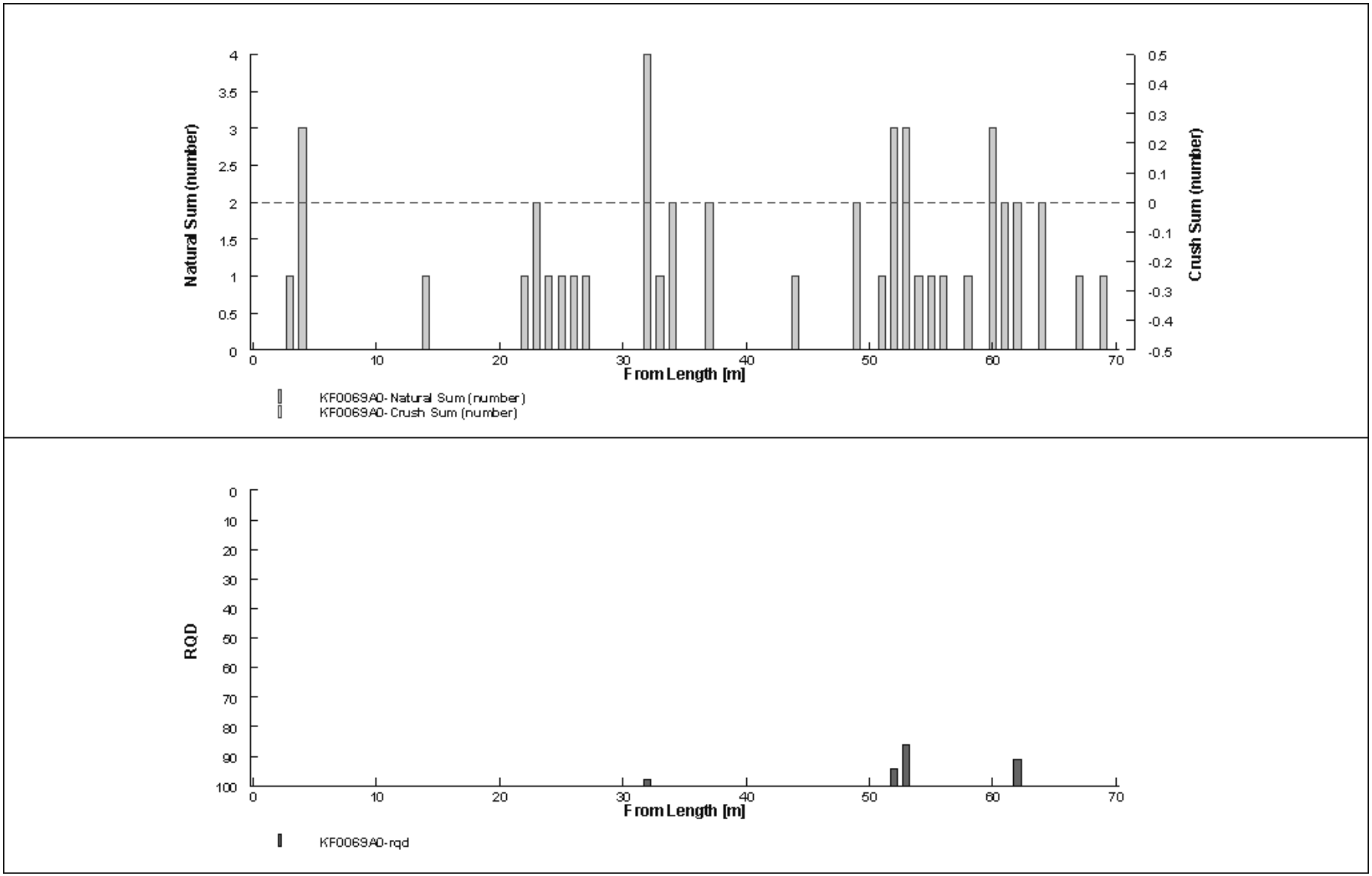
Natural Sum (number)
Crush Sum (number)
From Length [m]
KF0069A0-Natural Sum (number)
KF0069A0-Crush Sum (number)
RQD
From Length [m]
KF0069A0-rqd

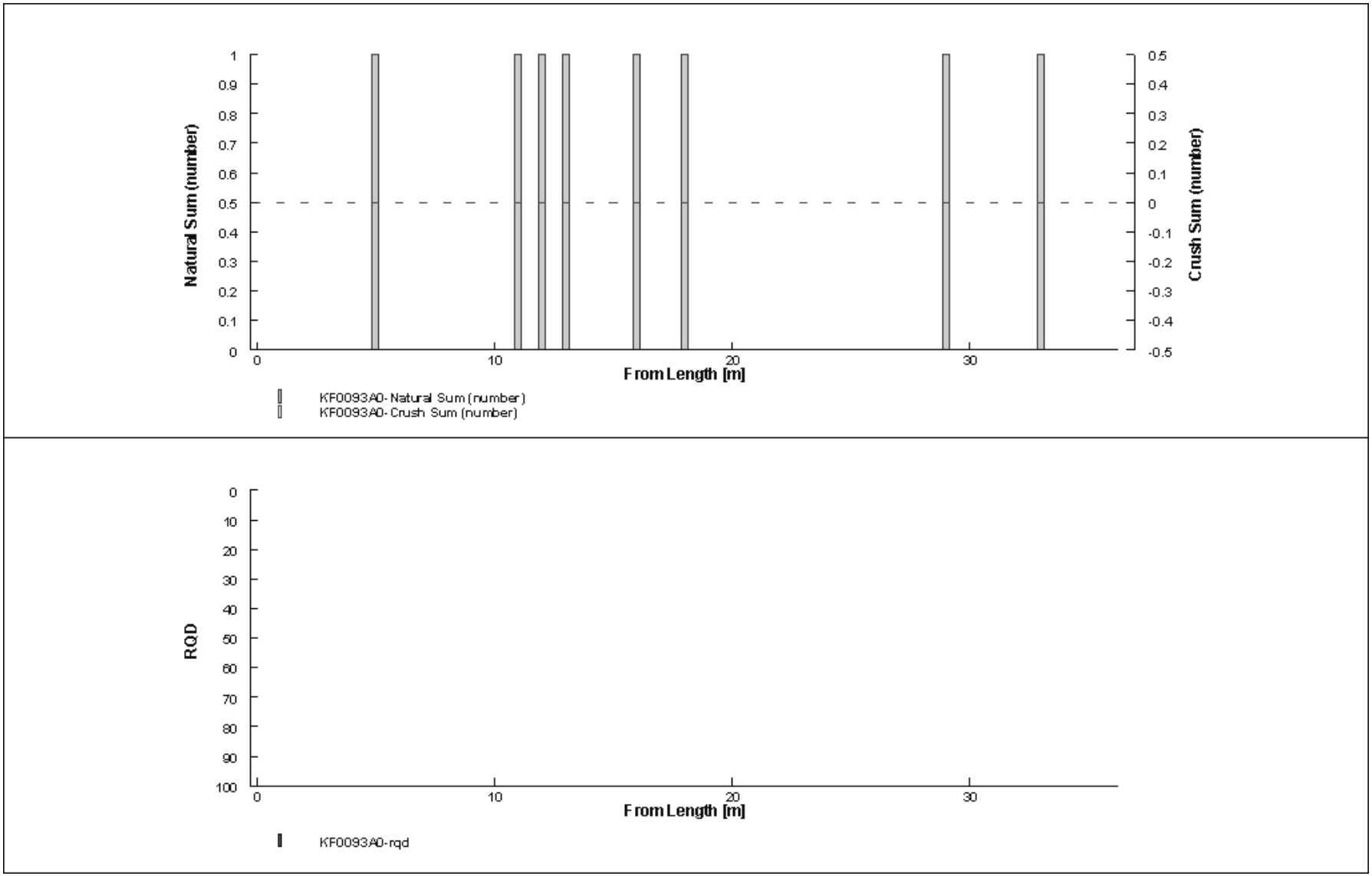
Natural Sum (number)
Crush Sum (number)
From Length [m]
KF0093A0-Natural Sum (number)
KF0093A0-Crush Sum (number)
RQD
From Length [m]
KF0093A0-rqd

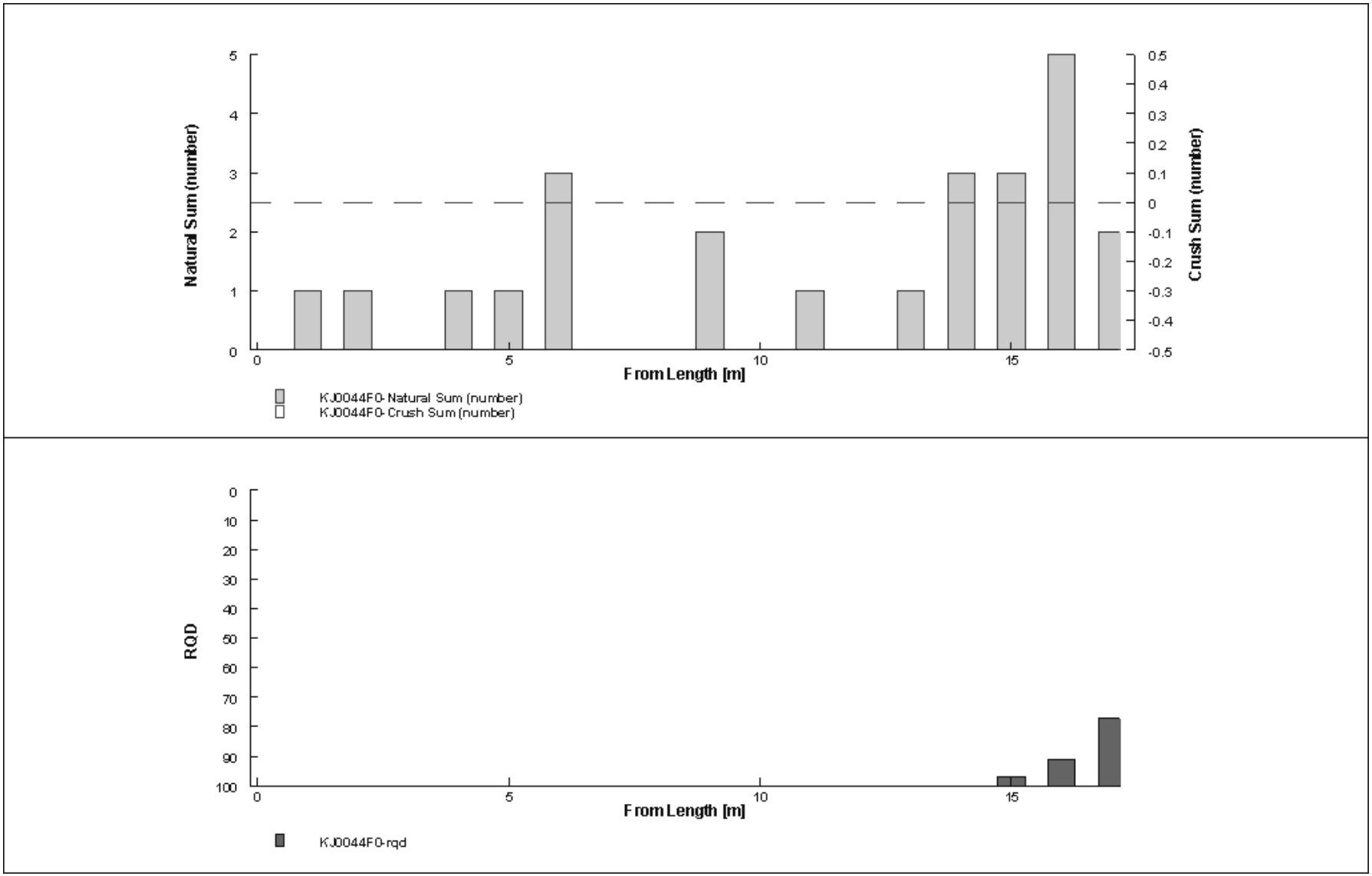
Natural Sum (number)
Crush Sum (number)
From Length [m]
KJ0044F0-Natural Sum (number)
KJ0044F0-Crush Sum (number)
RQD
From Length [m]
KJ0044F0-rqd

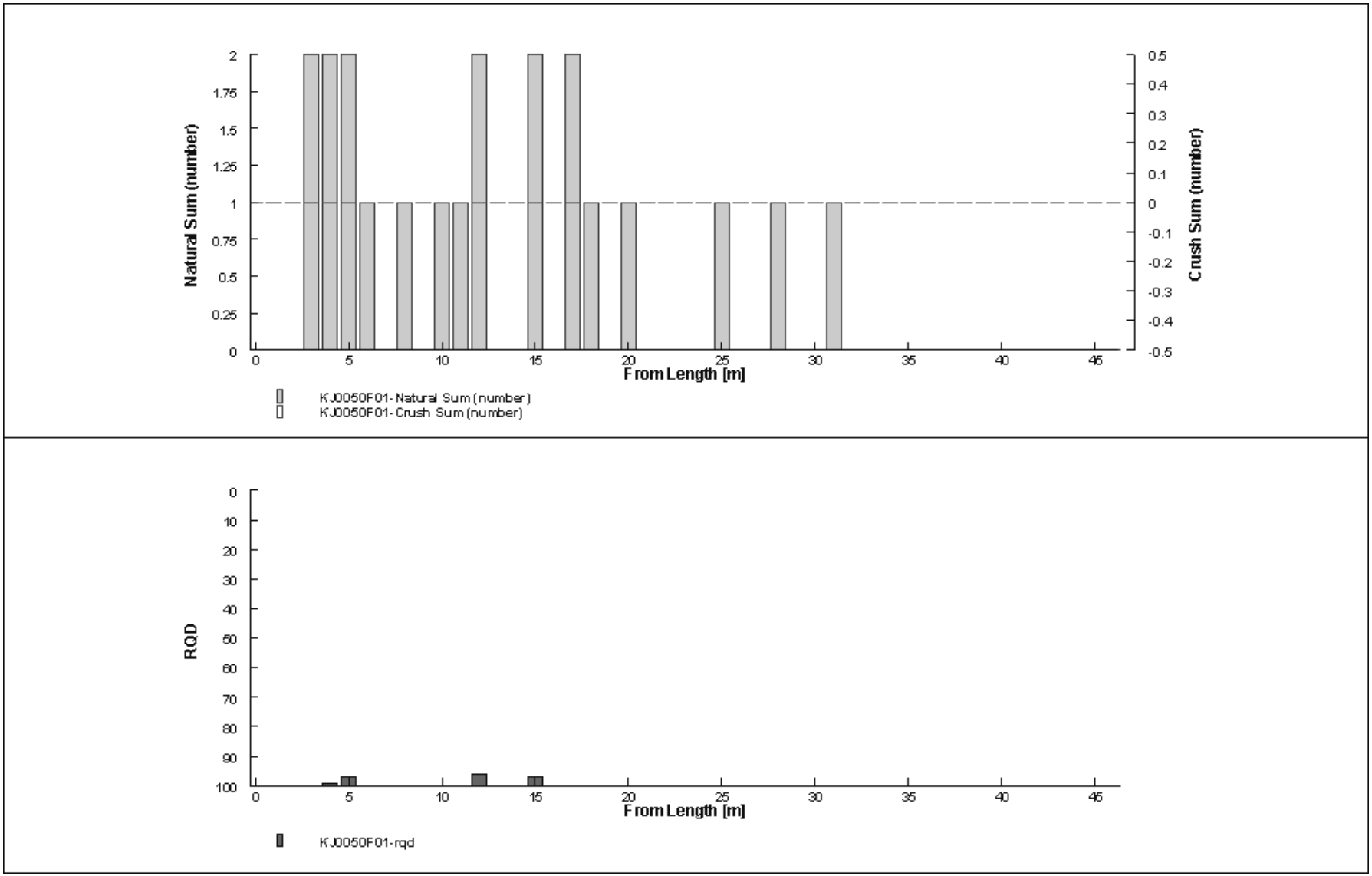
Natural Sum (number)
Crush Sum (number)
From Length [m]
KJ0050F01-Natural Sum (number)
KJ0050F01-Crush Sum (number)
RQD
From Length [m]
KJ0050F01-rqd

Appendix B. Correlation of water-bearing points/sections to core mapping characteristics

ID	Length, m	RQD	Natural fractures	Crush zone	Rocktype	Veins	Contact
KA2162B	237-238	71	2	Y	Granite	-	-
	252-254	100 / 98	0 / 2	N	Granite	-	-
	256-257	100	2	N	Granite	-	-
	270-271	93	4	N	Aplite	-	Aplite – granite, L=271.43
KA2511A	23						
KA2563A	12.5	100	2	N	Diorite	-	-
	68.5	0	-	Y	Diorite	-	-
	90.35-94.85	92 / 100 / 80 / 100 / 96	3 / 0 / 4 / 0 / 6	N	Aplite Mafic volcanite Aplite	-	Aplite-mafic volcanite, L=90.58 Mafic volc.-aplite, L=93.86
	102-105	86 / 100 / 84	7 / 2 / 4	N	Diorite		
KA2598A	18.5	100	1	N	Diorite	-	-
	37.4-39.4	100	2/1/2	N	Diorite	-	-
	49.8-52.4	79/100 /89/100	8/3/5/0	Y (L=49-50)	Aplite	-	L=49.94: transition to gneissic aplite
	73.5-75.5	92/100/ 84	5/3/5	N	Aplite	-	L=73: transition from brecciated to tectonised aplite
KA3191F	123.58	86	4	Y	Diorite	-	-
	124.1	59	7	Y	Diorite	-	-
	195	77/75	7/7	N	Diorite	-	-
	202.5	100	4	N	Diorite	-	-
KA3376B01	43.4	73	11	N	Diorite	-	-
	45.6	100	0	N	Diorite	Granite vein (45.55-45.61)	-
	47.7	92	5	N	Diorite	-	-
	48.2	89	6	N	Diorite	-	-
	49.5	100	0	N	Diorite	-	-
	49.8	100	0	N	Diorite	-	-
	50.5	100	1	N	Diorite	-	-
	51.8	91	4	N	Diorite	-	-
	52.1	100	0	N	Diorite	-	-
	57	100	1	N	Diorite	-	-
	58.2	100	1	N	Diorite	-	-
	59.8	97	3	N	Diorite	-	-

	61.2	96	2	N	Diorite	-	-
	62.6	93	4	N	Diorite	-	-
	63.4	73	11	N	Diorite	-	-
	63.7	73	11	N	Diorite	-	-
	65.2	87	6	N	Diorite	-	-
	65.6	87	6	N	Diorite	Vein pegmatite (65.7-65.84)	-
	66.8	100	2	N	Diorite	Vein pegmatite (66.58-66.7)	-
	69.2	89	5	N	Diorite	Xenolith amphibolite (68.9-69.17)	-
	70.8	100	2	N	Diorite	-	-
	71.7	100	2	N	Diorite	-	-
	72.4	100	2	N	Diorite	-	-
	73.6	100	1	N	Diorite	-	-
KA3386A01	10.1	93	4	N	Diorite	Granite vein (10.06-10.11)	-
	10.7	93	4	N	Diorite	-	-
	32.4*	100	1	N	Diorite	-	-
	40*	84	7	N	Aplite	-	-
	41	98	6	N	Aplite	-	-
	41.2*	98	6	N	Aplite	-	-
	36.4	94	5	N	Aplite	-	-
	43.1	86	8	N	Aplite	-	-
	43.6	86	8	N	Aplite	-	-
KC0045F	31.6	0	3	Y	Aplite	-	-
	57.8	0	6	Y	Aplite Diorite	-	L=57.85
	68.1	75	8	N	Aplite	-	-
	71.2	66	7	N	Aplite	-	-
KF0066A01	8.1	98	4	N	Diorite	-	-
	56.1	95	3	N	Diorite	-	-
KF0069A01	64.8	100	2	N	Diorite	-	
	66.1	100	0	N	Diorite (61.94-66.28) Hybride rock (66.28-27.3)	-	? (66.28)

The data for RQD and natural fractures are taken for a 1m section including the measured inflow depth.

Appendix C: Mechanical properties of the intact rock - results from the laboratory investigations

Presentation of raw data from Nordlund et al., 1999

5.1 The specimens

The specimens were prepared using the cores from three boreholes drilled in the floor of the tunnel in the Äspö Hard Rock Laboratory. The diameter of the cores is 45 mm. All the specimens are listed in Table 5-1.

Table 5-1 All the specimens for the tests.

No.	Depth (m)	Borehole	Dimension (mm) Diameter × Length
		For compression tests	
C1	1.95 – 2.10	KA3557G	ϕ45 × 115
C2	2.45 – 2.60	KA3557G	ϕ45 × 115
C3	2.60 – 2.75	KA3557G	ϕ45 × 115
C4	2.75 – 2.90	KA3557G	ϕ45 × 115
C5	3.86 – 4.01	KA3557G	ϕ45 × 115
C6	5.11 – 5.26	KA3557G	ϕ45 × 115
C7	5.26 – 5.41	KA3557G	ϕ45 × 115
C8	7.08 – 7.24	KA3557G	ϕ45 × 115
C9	7.40 – 7.55	KA3557G	ϕ45 × 115
C10	1.46 – 1.62	KA3545G	ϕ45 × 115
C11	1.84 – 2.01	KA3545G	ϕ45 × 115
C12	2.12 –2.28	KA3545G	ϕ45 × 115
C13	3.52 – 3.67	KA3545G	ϕ45 × 115
C14	3.68 – 3.84	KA3545G	ϕ45 × 115
C15	3.84 – 3.99	KA3545G	ϕ45 × 115
C16	4.34 – 4.49	KA3545G	ϕ45 × 115
C17	6.01 – 6.18	KA3545G	ϕ45 × 115
C18	4.69 –4.85	KA3551G	ϕ45 × 115

Table 5-1 (continued)

		For Brazil tests	
BR1-2(1)	1.30 – 1.45	KA3557G	ϕ45 × 22.5
BR1-2(2)	1.30 – 1.45	KA3557G	ϕ45 × 22.5
BR3-5(1)	0.94 – 1.09	KA3545G	ϕ45 × 22.5
BR3-5(2)	0.94 – 1.09	KA3545G	ϕ45 × 22.5
BR3-5(3)	0.94 – 1.09	KA3545G	ϕ45 × 22.5
		For three point bending tests	
B1	0.54 – 0.74	KA3557G	ϕ45 × 180
B2	0.74- 0.94	KA3557G	ϕ45 × 180
B3	2.10- 2.30	KA3557G	ϕ45 × 180
B4	2.90 – 3.11	KA3557G	ϕ45 × 180
B5	7.44 – 7.64	KA3545G	ϕ45 × 180

Table 5-2 The test results.

Compression tests

No.	σ_3 (MPa)	P_{max} (kN)	σ_{1c} (MPa)		E (GPa)		ν		σ_{ci} (MPa)	σ_{cd} (MPa)
				mean	E_{ini}	E_{50}	ν_{ini}	ν_{50}		
C1*	0	327	206	219	75	75	0.23	0.27	147	192
C6*	0	365	229		86	75	0.22	0.29	98	195
C9*	0	322	202		79	70	0.19	0.27	108	184
C10	0	379	238							
C7	5	432	272	256						
C11	5	411	258							
C18	5	380	239							
C5	20	575	362	346						
C15	20	556	350							
C17	20	520	327							
C4	40	690	434	690						
C3	50	723	455	502						
C12	50	840	528							
C16	50	832	523							

* strain-gauged specimen; Dimension: $\phi 45 \times 11.5$ mm

Brazil tests

Specimen No.	Ultimate load P_{max} (kN)	Tensile strength, σ_t (MPa)	
			mean
BR1-2(1)	25.3	15.8	14.7
BR1-2(2)	26.4	16.5	
BR3-5(1)	20	12.5	
BR3-5(2)	23	14.4	
BR3-5(3)	23	14.4	

Diameter of the specimens: D = 45 mm, Thickness of the specimens: t = 22.5 mm

Three-point bending tests

Specimen No.	Tip distance a_0 (mm)	Ultimate load F_{max} (kN)	Fracture toughness K_{IC} (MPa$\sqrt{m}$)	
				mean
B1	7.7	2.81	3.28	3.21
B2	7.2	2.92	3.29	
B3	7.5	2.60	3.00	
B4	7.4	2.94	3.36	
B5	7.7	2.69	3.14	

D = 45 mm, S = 3.33D = 150 mm.

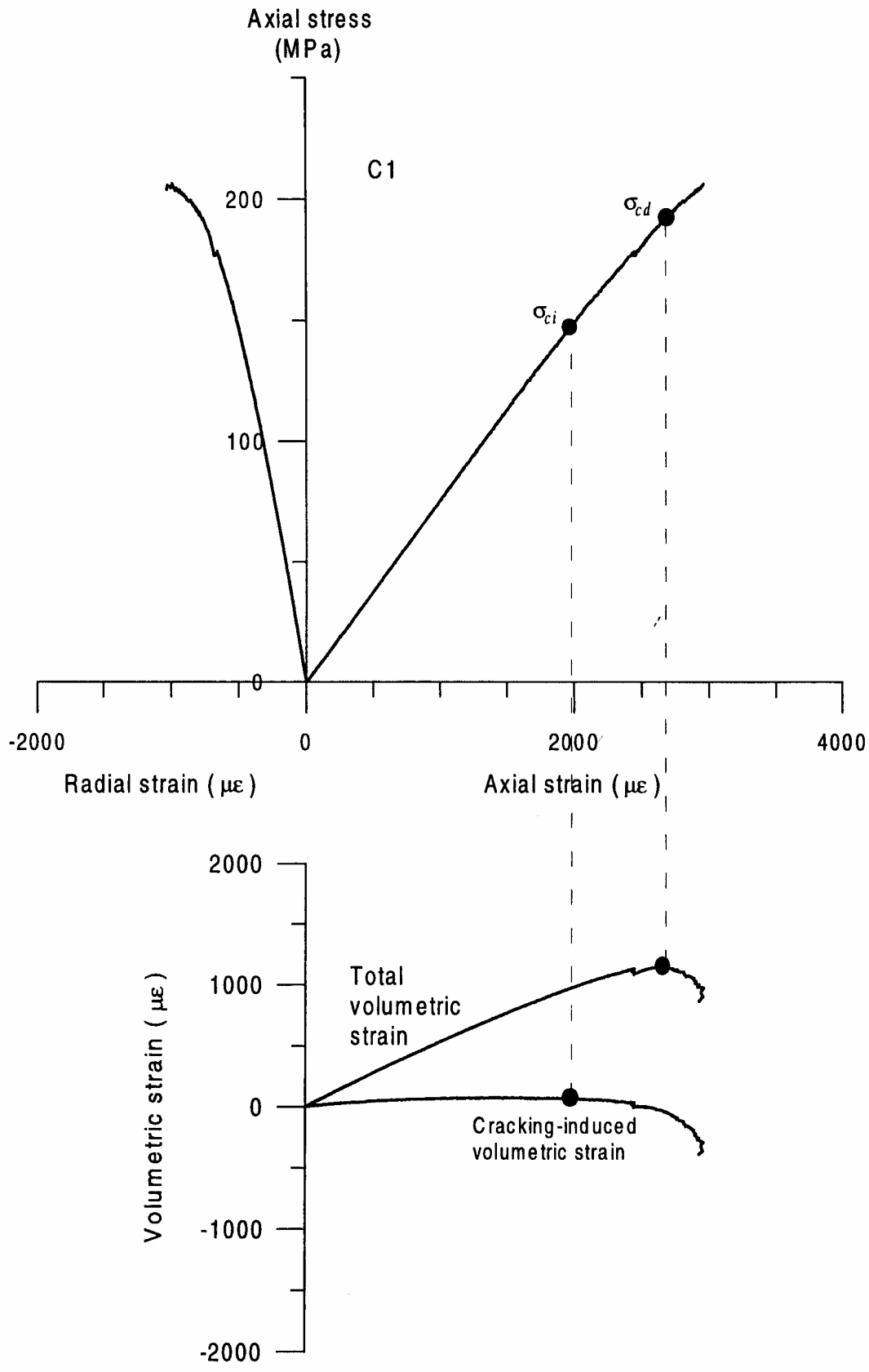

Figure A-1 The stress-strain curves of specimen C1.

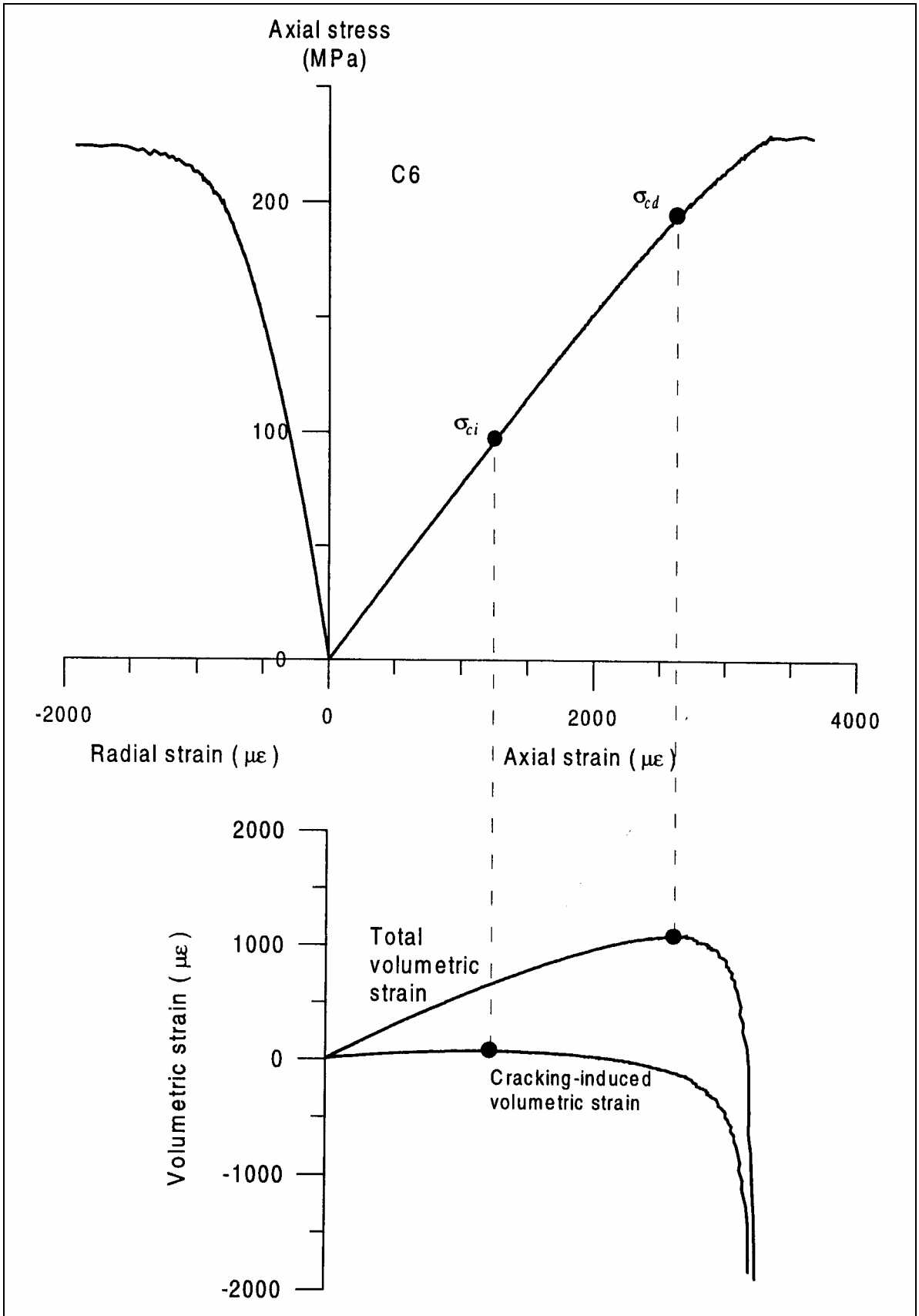

Figure A-2 The stress-strain curves of specimen C6.

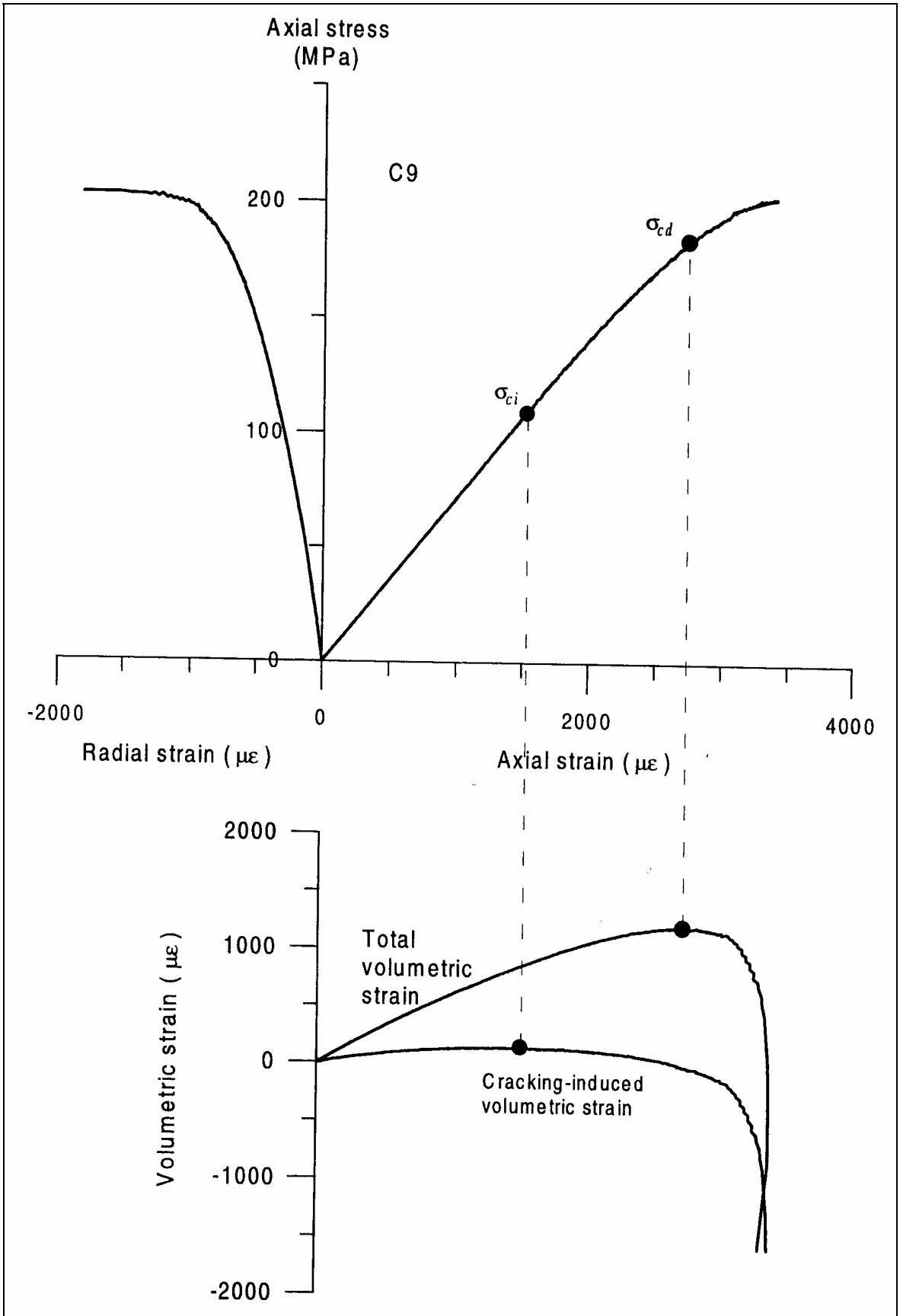

Figure A-3 The stress-strain curves of specimen C9.

Appendix D: Mechanical properties of fractures

Mechanical properties of fracture samples selected from borehole KAS02 (from Stille and Olsson, 1989)

Sample[(1)]	Level (m)	K_s (MPa/mm)	K_n (MPa/mm)	Low normal stress c_{pl} (MPa)	Low normal stress ϕ_{pl} (°)	Higher normal stress c_{ph} (MPa)	Higher normal stress ϕ_{ph} (°)
ST1	-397,81	8.4	4.7-22.7	0.1	47	0.4	43
ST2	-350,17	19.2	27.7	0.1	49	0.5	42
ST3	-327,44	7.2	10.4	0.8	63	2.4	29
ST5	-462,80	11.6	12.2	0.4	57	1.6	34
ST6	-500,18	7.4	9-26	0.3	47	1	36
ST8	-360,64	8.0	13.2	0.0	37	1.3	17
ST9	-394,52	7.6	12.5	0.2	38	1.0	29
ST10	-484,73	4.8	15.0	1.0	65	4.0	21
ST11	-281,40	8.9	11.6	0.5	54	1.7	38
ST12	-292,56	11.4	15.1	0.8	55	2.0	34

(1) ST1-ST6 belong to the steeply dipping fracture set, and ST8-ST12 belong to the gently dipping fracture set.

Secant normal stiffness, K_n, during the virgin loading and reloading cycles, for different stress intervals (from Lanaro, 2001).

Borehole	Fracture set	Depth (m)*	Secant normal stiffness, K_n (MPa/mm)										
			σ_n, during virgin normal loading cycle (MPa)								σ_n, during reloading (MPa)		
			Initial	0.5-5	0.5-10	0.5-15	0.5-30	5-10	5-15	10-15	0.5-5	0.5-10	0.5-15
KA3548A01	Sub-vertical fracture set	-446.87	40	78	151	155		312	278	218	144	200	207
		-447.51	22	61	84	86		91	106	101	72	67	74
KA3573A		-446.30	33	55	75	85		55	121	115	101	95	192
		-446.47											
		-446.81	300	71	124	139		92	200	184	101	101	179
KA3600F		-446.90											
		-446.90	138	106	134	117		177	93	93	142	141	189
		-446.91	24	59	81	92		110	126	126	77	77	98
KG0021A01		-432.84	57	83	136	138		199	141	141	137	167	139
KG0048A01		-442.68	66	161	326	453					440	699	565
		-437.87	41	89	143	174		105	277	299	206	146	165
		-433.37	85	69	92	116		150	183	182	101	112	125
		-433.26	68	55	54	61		54	78	78	120	123	124
KA3579G	Sub-horizontal fracture set	-457.80	118	185	279	363	535	514	853	949	280	385	681
		-459.10	37	73	130	191	357	457	1572	2023	174	279	735
		-459.62	31	72	132	193	352	525	1480	1669	222	424	1124
		-463.23	124	783	322	454	798	1027	2012	2700	818	1157	2432
		-467.81	124	274	500	738	1367	1972	7187	7702	578	1399	3170

* The depth of samples is absolute depth and has been re-calculated according to the co-ordinates of the boreholes.

Shear stiffness, K_s, of the selected rock fracture samples for different normal stresses (from Lanaro, 2001)

Borehole	Fracture set	Depth (m)*	Shear Stiffness, K_s (MPa/mm)											
			σ_n= 0.5 MPa			σ_n=1 MPa			σ_n=5 MPa			σ_n=10 MPa		
			Initial	Peak	Reload	Initial	Peak	Reload	Initial	Peak	Reload	Initial	Peak	Reload
KA3548A01	Sub-vertical fracture set	-446.87	5.6	3.3	7.9				17.5	11.4	27.6	35.5	14	37.7
		-447.51	1.9	2.1	4.4				7.9	6.2	35.1	25.1	12.8	46.6
KA3573A		-446.30	1.1	-	5.5				7.1	5.3	39.8	21.7	7.6	48.2
		-446.47												
		-446.81	1.5	1.2	7.9				20.1	16	27.7	35.1	13.6	45.1
KA3600F		-446.90												
		-446.90	3.9	3.7	5.3				22.9	8	36.8	43.4	11.5	30
		-446.91	4.2	0.2	3.8				1.5	1	45.3	28.1	15	52.3
KG0021A01		-432.84	0.8	0.6	-				4.7	4	40.4	25.7	5.4	40.2
KG0048A01		-442.68	4.6	2.2	27.1				11.8	7.5	-	27.2	8.1	-
		-437.87	0.9	-	5.8				19.3	13.6	28.3	27.1	9.3	67.9
		-433.37	2.3	2.1	6.1				13.1	9.2	27.9	32.2	14.9	37.9
		-433.26	15.4	4.5	6				-	13.5	17.6	32.7	6.3	45.7
KA3579G	Sub-horizontal fracutre set	-457.80	-	-	-	2.5	2.5	7.6	19.7	8.9	36.6	44.5	10.5	34.4
		-459.10	-	-	-	15.9	8.4	12.7	18.4	13.9	25.6	28.5	16.6	30.3
		-459.62	1.9	2.1	4.4	-	-	-	10.1	6.2	35.1	20.8	13	48.1
		-463.23	8.3	3.4	13.8	-	-	-	9.6	7.8	44.9	28.3	6.3	58.6
		-467.81	4.5	4.1	12.6	-	-	-	16.7	7.2	30.9	32.7	9.5	45.6

* The depth of samples is absolute depth and has been re-calculated according to the co-ordinates of the boreholes.

Appendix E: Results from laboratory investigations of thermal properties of the intact rock (from Sundberg, 2002a and 2002b)

Thermal conductivity, W/m K, and density at room temperature presented for each rock type (Sundberg, 2002a)

Sample no	Äspö Diorite	Altered Äspö Diorite	Ävrö granite	Fine-grained granite	Density (kg/m^3)
1	2.49				2765
2	2.34				2769
3	2.47				2755
4			2.99		2673
5				3.58	2635
6				3.68	2648
7	2.84				2707
8	2.69				2720
9		3.11			2726
10			3.22		2655
11			3.55		2662
Geom. mean:	2.56	3.11	3.24	3.63	

Coefficient of thermal expansion for different temperature intervals (from Sundberg, 2002b).

Sample number	Coefficient of Thermal Expansion (m/mK)					
	5-50˚C	5-95˚C	50-105˚C	25-95˚C	50-95˚C	5-105˚C
1	8,06E-06	8,34E-06	7,80E-06			
2	8,96E-06	8,55E-06	6,51E-06	7,82E-06	7,37E-06	
3	7,73E-06	7,48E-06	7,50E-06			
4	6,66E-06	7,24E-06	7,72E-06			
5a	6,73E-06	6,55E-06	6,53E-06			
5b	6,94E-06	6,68E-06	6,23E-06			
6	8,54E-06	7,70E-06	7,41E-06	6,68E-06		
7	7,32E-06	7,80E-06	8,33E-06			
8	6,89E-06	7,28E-06	7,21E-06			
9	9,24E-06	7,25E-06	6,78E-06	6,76E-06		
10	9,68E-06	8,98E-06	6,77E-06			
11	7,64E-06	7,79E-06				7,85E-06